

**EFFECTS PRODUCED IN GaAs BY  
MeV ION BOMBARDMENT**

Thesis by  
Chu Ryang Wie

In Partial Fulfillment of the Requirements  
for the Degree of  
Doctor of Philosophy

California Institute of Technology

Pasadena, California

1985

(Submitted May 10, 1985)

## ACKNOWLEDGEMENTS

I would like to express my deepest appreciation to many people at Caltech for providing a stimulating environment which made this work possible. Foremost among them are Professor Tom Tombrello, my advisor, and Professor Thad Vreeland, Jr., my friendly guide in materials research. Dr. Tombrello gave me freedom and enthusiastic support throughout this research. Dr. Vreeland has been a very friendly teacher in the lab, providing many enthusiastic discussions during the entire research.

Many thanks go to M. H. Mendenhall, R. P. Livi, and J. Y. Tang for their help in the tandem lab, and to V. Speriosu for his help in the x-ray lab during the earlier period of this research. I am also grateful to Peter Haff, C. R. Shi, and graduate students and technicians in our group for providing friendly environment and helpful discussions.

I would like to thank Dr. R. Grant, and Dr. Bob Housley at Rockwell International Science Center for their important collaboration in the ESCA analysis of the GaAs samples.

Finally, I would like to dedicate this thesis to my parents, and my brothers and sisters in Korea. Without their support and love, I couldn't be here in America to study science.

## ABSTRACT

Presented in the first part of this thesis is work performed on the ionizing energy beam induced adhesion enhancement of thin ( $\sim 500$  Angstrom) Au films on GaAs substrates. The ionizing beam, employed in the present thesis, is the MeV ions (i.e.,  $^{16}\text{O}$ ,  $^{19}\text{F}$ , and  $^{35}\text{Cl}$ ), with energies between 1 and 20 MeV. Using the "Scratch" test for adhesion measurement, and ESCA for chemical analysis of the film-substrate interface, the native oxide layer at the interface is shown to play an important role in the adhesion enhancement by the ionizing radiation. A model is discussed which explains the experimental data on the the dependence of adhesion enhancement on the energy which was deposited into electronic processes at the interface. The ESCA data indicate that the chemical bonds (or compounds), which are responsible for the increase in the thin film adherence, are hydroxides rather than oxides.

In the second part of the thesis we present a research performed on the radiation damage in GaAs crystals produced by MeV ions. Lattice parameter dilatation in the surface layers of the GaAs crystals becomes saturated after a high dose bombardment at room temperature. The strain produced by nuclear collisions is shown to relax partially due to electronic excitation (with a functional dependence on the nuclear and electronic stopping power of bombarding ions). Data on the GaAs and GaP crystals suggest that low temperature recovery stage defects produce major crystal distortion. The x-ray rocking curve technique with a dynamical diffraction theory analysis provides the depth distribution of the strain and damage in the MeV ion bombarded crystals.

## TABLE OF CONTENTS

Acknowledgements	ii
Abstract	iii
Table of Contents	iv
I. General Introduction	1
II. MeV Ion-Induced Enhanced Adhesion of Au Films on GaAs	5
1. Previous work	5
2. Experiment and results	15
3. Discussion and model	31
III. Strain/Damage in MeV Ion Bombarded GaAs	35
1. Introduction	35
2. Dynamical x-ray diffraction in nonuniform crystalline films	39
2.1 Strain/damage measurement by x-ray rocking curve technique	39
2.2 Dynamical diffraction theory and rocking curve analysis	45
3. Behavior of CaF <sub>2</sub> , LiNbO <sub>3</sub> , Si, and Cu crystals	51
4. GaAs and III-V semiconductors	60
4.1 Lattice disorder and recovery stages in III-V's	60
4.2 Experimental results and discussion	65

4.2.1 GaAs	65
4.2.2 GaP	86
4.2.3 Summary	91
Appendix A - Derivation of the Takagi-Taupin Equation	93
Appendix B - Formula for Evaluating $s = \sqrt{C^2 - B^2}$	97
References	98

## I. General Introduction

An incident energetic ion in solid materials loses energy by electronic and nuclear collisions with target atoms, as it slows down and eventually comes to rest. The electronic collision excites the target electrons from the innershells or valence bands to the higher lying states or conduction bands. Thereby, it leaves the target atoms around the ion track in a highly excited state immediately after the collision. The nuclear collision causes a direct momentum transfer from the incident ion to the target nuclei through a screened Coulomb interaction. When the energy transfer by nuclear collision exceeds the threshold displacement energy, the collision results in direct displacements of target atoms.

Figure 1 shows a rough schematic of the energy loss per unit length of an ion  $dE/dX$ , which is commonly called the stopping power, as a function of ion energy. At a high energy, higher than 100-500 keV for the ions incorporated in the present thesis, the electronic stopping is the dominant energy loss process. At energies below that, the nuclear stopping becomes a major energy loss process. The energy range of ions incident on the target, employed in the present thesis, is somewhat below the energy of maximum electronic stopping power which occurs at the ion velocity of approximately  $Z_1^{2/3}e^2/\hbar$ . When the ion velocity is less than the Bohr velocity,  $v_0=e^2/\hbar$ , the electronic stopping power is approximately given by the Lindhard-Scharff formula (Li61).

$$S_e(E) = 72.69 \frac{Z_1^{7/6} Z_2}{M_2 (Z_1^{2/3} + Z_2^{2/3})^{3/2}} \sqrt{\frac{E}{M_1}} \quad \text{for } E < \frac{1}{2} M_1 v_0^2, \quad (1)$$

where  $S_e$  is the electronic  $dE/dX$  in  $MeV/mg/cm^2$ ,  $E$  is in  $MeV$ , and  $M$  in

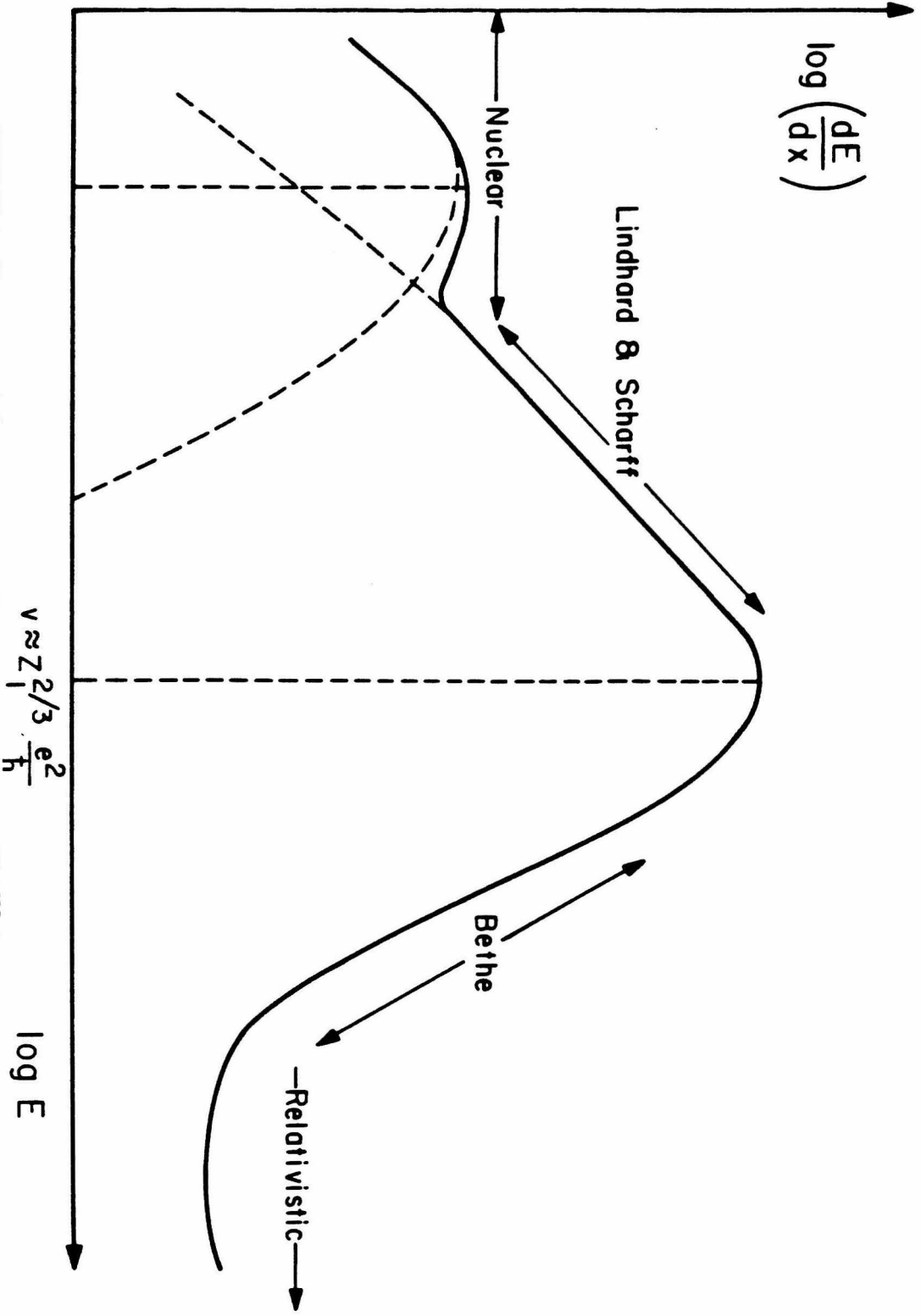


**FIGURE 1.** The general dependence of the stopping power,  $dE/dX$ , is shown as a function of energy for an ion travelling through matter. The schematic was taken from Sigmund (Sigmund 1977).

*amu*. Since the initial incident velocity of ions incorporated in this thesis lies somewhere between the Bohr velocity and the velocity of maximum electronic stopping power, the electronic stopping power values used in this thesis are taken from the Northcliffe-Schilling data book (No70).

A detailed numerical calculation of the nuclear stopping power values was done by Wilson et al. for the screened scattering of various ion-target combinations (Wi77). They suggested one nuclear stopping power formula as a best estimate, which was identified in their paper as Kr-C. In the present thesis, the nuclear stopping power values are obtained from the Kr-C formula which is

$$S_n(E) = 2.547 \frac{Z_1 Z_2 M_1}{M_2 (M_1 + M_2) (Z_1^{2/3} + Z_2^{2/3})^{1/2}} \frac{\ln(1+\varepsilon)}{(\varepsilon + 0.10718\varepsilon^{.37544})}, \quad (2)$$

where

$$\varepsilon = \frac{32530 M_2}{Z_1 Z_2 (M_1 + M_2) (Z_1^{2/3} + Z_2^{2/3})^{1/2}} E$$

and the units are the same as those in Formula (1).

Ions with energy between several *MeV* and several tens of *MeV* are referred to as *MeV* ions. When one comes to discuss a physical phenomenon induced by *MeV* ions, one is usually concerned with the coupling mechanism of the energy deposited into the target electronic system to a physical process which would result in the observed phenomenon. Ion damage tracks in insulating materials produced by *MeV* ions are an example. Since the damage tracks are produced by the electronic erosion process of the ion, the observability of tracks are closely related to the target electronic properties (Fl75). Ion damage tracks are produced in most insulators and in some selected compound



semiconductors whose conductivities are lower than a certain value (Mo68), but not in metals. The exact physical mechanism is still controversial (Da81, To84a). Another example of energy conversion from the excited electronic system to atomic motion is the sputtering effects, i.e., the ejection of atoms from the target surface when bombarded with MeV ions. The sputtering yield, i.e., the number of ejected atoms per bombarding ion, is correlated with the electronic stopping power of the bombarding MeV ion (Gr79a). The sputtering by MeV ions is believed to be related to the formation of ion damage tracks (To84b)

The electronic processes of MeV ions may induce chemical changes in the target materials other than the atomic displacements. An MeV ion, crossing the interface of two materials in contact, may trigger a local chemical reaction of the participating atoms. The enhanced adhesion of thin films on a substrate by MeV ion bombardment appears to be closely related to this chemical process. Work on the enhanced adhesion of thin gold films on GaAs substrates by MeV ion bombardment is presented in the first part of this thesis.

The nuclear stopping power is typically several  $eV$  per Angstrom for the MeV ions, whereas the electronic stopping power is typically two orders of magnitude larger. This relatively small nuclear stopping is responsible for the structural damage process in good electrical conductors such as metals and semiconductors. The degree of structural damage in solids by MeV ions lies in between those by keV ions and MeV electrons for a comparable beam dose. Thus MeV ions provide a good tool for the study of radiation damage in materials. A study of structural damage and induced change in lattice parameter in crystalline materials forms the second part of this thesis.

## II. MeV Ion-Induced Enhanced Adhesion of Au Films on GaAs

### 1. Previous Work

Since the discovery of MeV ion beam-induced enhanced adhesion of thin metallic films on insulating substrates by Griffith, Qui, and Tombrello at Caltech (Gr82), there have been extensive experimental efforts to clarify the physical mechanism involved in this phenomenon. Various sample combinations, e.g., metal-metal, metal-semiconductor, and metal-insulator, have been studied by irradiating with MeV ion beams, keV electron beams, and UV photons.

The data obtained at Caltech and other institutions suggest that new chemical/physical bond formation at the interface triggered by the ionizing radiation is responsible for the enhanced adhesion. However, there have been numerous speculations on the mechanisms. We describe some of these proposed mechanisms.

(1) Atomic mixing: When Griffith et al. first observed the remarkable adhesion enhancement by MeV ion bombardment for thin metal films on insulating substrates, the first model was of interface atomic mixing driven by the nuclear damage track formation and ejection of atoms at the surface of insulating substrates. However, subsequent observation of similar adhesion enhancement on metal-metal and on metal-semiconductor samples, and the measurement of the interface mixed-layer thickness, the upper limit of which is less than 20 Angstroms, made this proposed mechanism less plausible. This is because nuclear damage tracks are usually not formed in metals and in semiconductors (except for some selected compound semiconductors, e.g., MoSe<sub>2</sub> (Fl75)), and because the sputtering yield from these materials is very small under the

bombardment conditions employed (To83). However, a small atomic mixing (i.e., mixing of a few atomic monolayers) may increase the adhesion significantly.

(2) An electrostatic force from electric dipole layer formation: When metals or semiconductors with different workfunctions are brought into contact, mobile charges move across the interface until the Fermi level in both materials become equal (i.e., thermal equilibrium for the electronic system). This process causes an electric dipole layer to form at the interface. Let us take an ideal Au and n-type GaAs contact as an example. The electrons move from the n-type GaAs to Au, creating a positive space charge layer in GaAs and excess electrons on the Au surface. For a doping level of  $1 \times 10^{18}/\text{cm}^3$  in GaAs, and a contact potential (or Schottky barrier) of .87 V, an estimated electrostatic force is about 3 psi ( pounds per square inch ) under an abrupt junction approximation (see, for example, Sz81). The effect of MeV ion bombardment on this electrostatic force is to decrease it. The reason is the following. The irradiation produces point defects in the space charge region near the GaAs surface. Some of these defects create new electronic energy levels within the bandgap of GaAs. These new levels trap mobile electrons or holes, reducing the mobile carrier density and thereby decreasing the space charge density in the depletion region. The electrostatic force due to the dipole layer is proportional to the space charge density times barrier energy.

(3) New bond formation and the role of an impurity oxide layer at the interface: This is the most probable mechanism for the ionizing beam (MeV ions, keV electrons, and UV photons) induced enhanced adhesion, and most data up-to-date point toward it. An ionizing radiation can enhance chemical reaction at an interface of gas-solid or liquid-solid. For

example, the irradiation of UV photons on the solid surfaces enhances the etching rate of gas phase or liquid phase etchants on GaAs or Si (As84, Br84, Po84). The etching reaction is believed to be initiated by photochemical gas-phase photodissociation and combined surface- and gas-phase chemistry in the dry etching case. Also, irradiation of 4 keV electrons on GaAs in an oxygen pressure of  $5 \times 10^{-5}$  Torr, triggers gallium oxide formation at the  $O_2$  gas and GaAs interface (Al84). In this case, the ionizing electron stimulates the chemical reaction of  $O_2$  gas with GaAs surface possibly by photodissociation of  $O_2$  molecules and electronic excitation of the GaAs surface. There is no reason why the enhanced interface chemistry should not happen at a solid-solid interface. The degree of ionization of atoms at the solid surfaces is much higher in the case of MeV ions than keV electrons or UV photons. The ionization density around an ion track is higher by orders of magnitude than in the case of electron or photon irradiation. Thus it is not surprising that the observable adhesion enhancement is easily achieved by MeV ion irradiation for those samples which are hard or practically impossible with keV electrons or UV photons. If there exist any impurity oxide layers at the interface, which may form during the thin film deposition process or may form by diffusion through the thin film to the interface under the ambient oxygen partial pressure, the beam induced chemical reaction is likely to happen between the oxide layer and the substrate surface or the thin film surface. Using XPS (x-ray photoelectron spectroscopy), or equivalently ESCA (electron spectroscopy for chemical analysis), we studied the interface chemistry for MeV ion bombarded Au films on GaAs. The results will be discussed in the next section.

In the rest of this section, the work performed previously at Caltech and at other institutions on the use of various ionizing radiations for the adhesion enhancement is described. A summary of the previous adhesion work is given in Table I.

The first use of an ionizing energy beam to induce adhesion enhancement of thin metallic films on various substrates was done by Griffith, Qui, and Tombrello at Caltech in 1981. They bombarded thin metallic films on insulating substrates with various MeV ions (Gr82). MeV ions of the same type were used, subsequently, to produce enhanced adhesion for metal-metal and metal-semiconductor combinations at Caltech and at Uppsala (We83, Me83, Ja83). In the experiment performed by Mendenhall, the threshold beam dose corresponding to passing the "Scotch" tape test was measured as a function of beam energy. Subsequently, Tombrello proposed a model which well explains this result (To83).

Similar observations of adhesion enhancement from 5-30 keV electron irradiation for Au films on Si substrates were subsequently reported by Mitchell et al (Mi84a). Since the MeV ion-induced adhesion enhancement is correlated with the electronic stopping power of the ion, their experiment was designed to test whether the enhancement is caused exclusively by the electronic processes. The same effect was found to occur at an electron beam dose which is typically three orders of magnitude higher than an MeV ion beam dose. Since the energy transfer by an electron is lower by about the same orders of magnitude than that by an MeV ion, this result suggests that the induced bonding mechanism is an individual process for each ion or electron.

Mitchell et al. have shown that a vacuum ultraviolet irradiation causes the same effects (Mi84b). They irradiated metal films on Si

**Table I.** Use of ionizing radiation for the enhancement of thin film adhesion.

<i>Radiations</i>	<i>Films - Substrates</i>	<i>References</i>
<i>MeV Ions</i>	<i>Au, Cu - Insulators SiN<sub>4</sub> - Si</i>	Griffith et al., Nucl. Instr. Meth., 198, (1982), 607.
<i>MeV Ions</i>	<i>Au, Insulators, Ag, - Semiconductors, Pd, Metals</i>	Werner et al., Thin Solid Films, 104, (1983), 163.
<i>keV electrons</i>	<i>Au - Si</i>	Mitchell et al., Appl. Phys. Lett., 44, (1984), 193.
<i>UV Photons</i>	<i>Au - Si</i>	Mitchell et al., Appl. Phys. Lett., 45, (1984), 137.
<i>MeV Ions</i>	<i>Insulators, Metals - Semiconductors, Metals</i>	M. H. Mendenhall, Ph. D. Thesis, Caltech, (1983).
<i>keV Electrons</i>	<i>Al - SiO<sub>2</sub></i>	Sai-Halasz et al., RMIT* Preprint, (1984).
<i>MeV Ions</i>	<i>Au - SiO<sub>2</sub></i>	Wie et al. Nucl. Instr. Meth., (1985) in press.
<i>MeV Ions</i>	<i>Metals - Insulators, Metals</i>	Jacobson et al., Univ. of Uppsala, Preprint, (1984).
<i>MeV Ions keV Electrons</i>	<i>Metals - Glasses</i>	Sood et al., RMIT Preprint, (1984).
<i>MeV Ions</i>	<i>Au - GaAs</i>	Livi et al., Proc. Matr. Res. Soc. (1984), in press.

\*Royal Melbourne Institute of Technology, Australia.

substrates with 21.2 eV (He I) and 10.2 eV (H Lyman $\alpha$ ) photons. Sai-Halasz et al. at RMIT (Royal Melbourne Institute of Technology, Australia) had put a static electric field across the oxide layer of Al films on SiO<sub>2</sub> grown on Si wafers during 10-20 keV electron irradiation, and found a much more pronounced adhesion enhancement over the case with no bias (Sa84). There was also extensive work at IBM and at RMIT (Ba84, So84). All these experimental data indicate that the adhesion enhancement is caused by additional bonds or stronger bond formation initiated by the electronic excitation/ionization of the interface atoms. Also, the keV electron and UV photon work indicates that the energy transfer to the interface atoms need not be much in excess of typical chemical bond energies, i.e., a few eV.

The fact that specific mechanism can be different for different systems was illustrated by a work on Au-SiO<sub>2</sub> (Wi85a). In this experiment, thin Au films (about 350 Angstrom thick) on vitreous SiO<sub>2</sub> substrates were bombarded with Cl ions of energy from 6.5 to 21 MeV, to a wide range of beam doses. The threshold in the enhanced adhesion corresponding to passing the "Scotch" tape test occurs in two different dose ranges at a given ion energy (see Figure 2(a)). The "Scratch" test result, shown in Figure 2(b), also illustrates the adhesion enhancement variation as a function of beam dose. At low doses ( $2 \times 10^{12}$  to  $5 \times 10^{13}$ /cm<sup>2</sup>), surface crazing of the vitreous SiO<sub>2</sub> substrate caused by a nonuniform stress relaxation in the bombarded region (Pr75) was shown to produce the enhanced adhesion force at the interface (Wi85a). The surface cracks close up at doses higher than  $5 \times 10^{13}$ /cm<sup>2</sup> for all the beam energies used (see Figure 3). The enhanced adhesion produced at higher doses correlates with the electronic stopping power, and the mechanism seems to fall within the

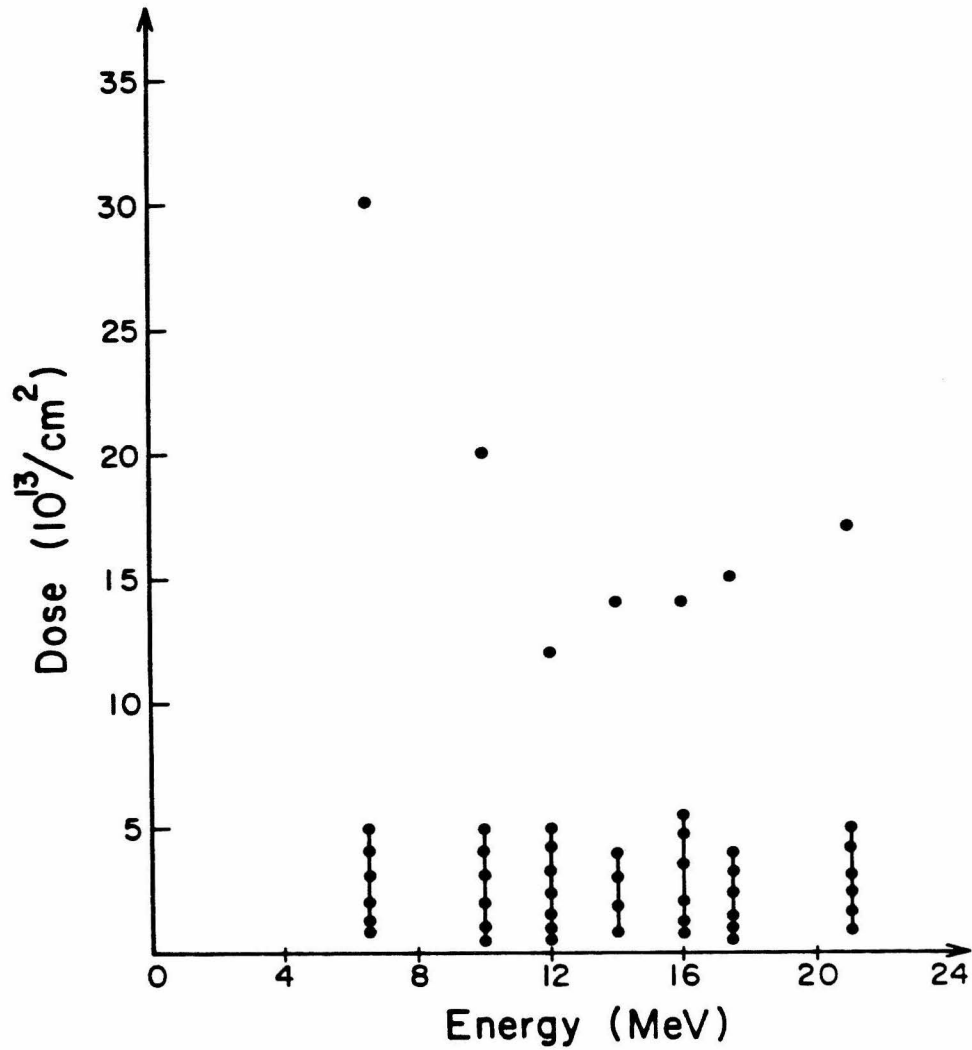


**Figure 2(a).** Threshold dose versus Cl ion bombarding energy for Au films on SiO<sub>2</sub>. The bars represent the low dose adhesion range; the single dots are the threshold doses for the higher dose adhesion. All the data points correspond to passing the tape test.



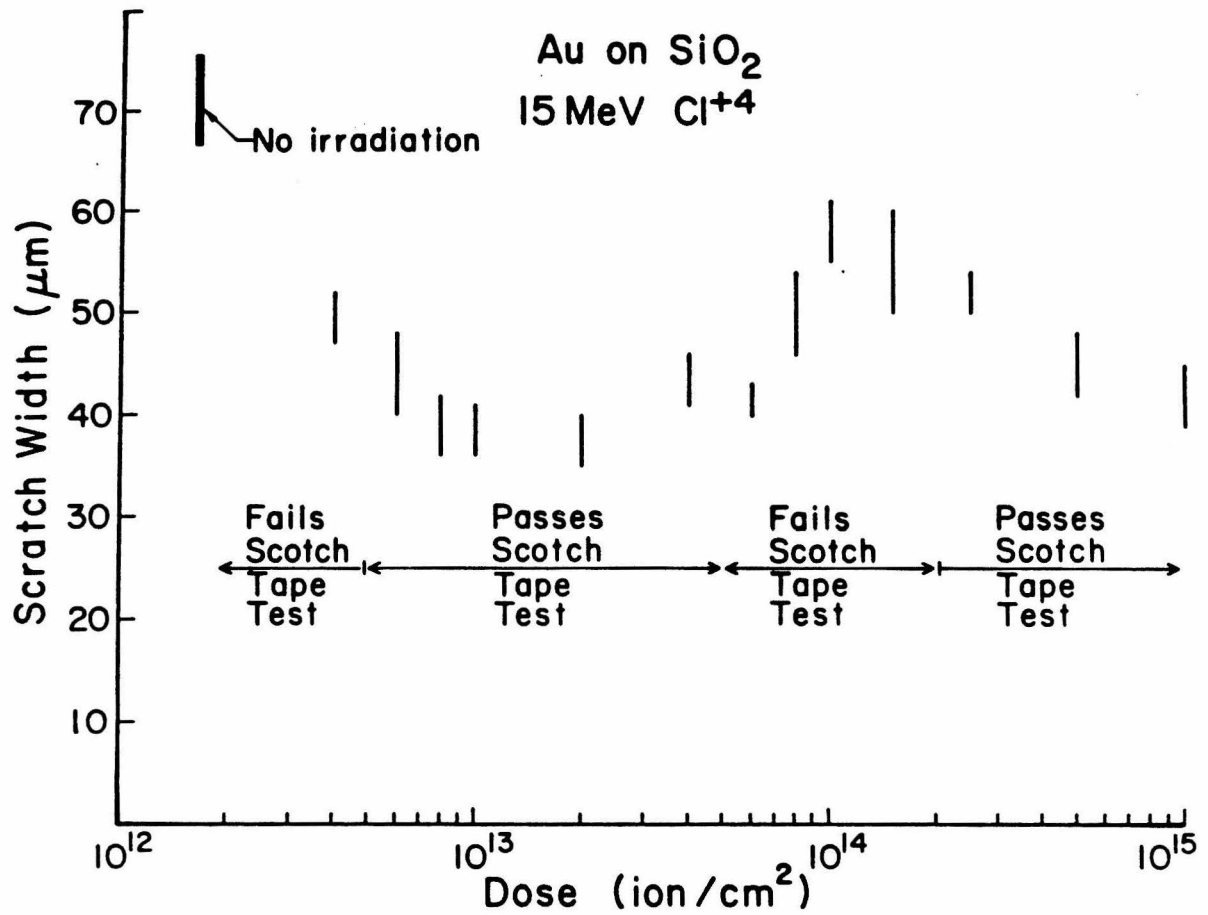
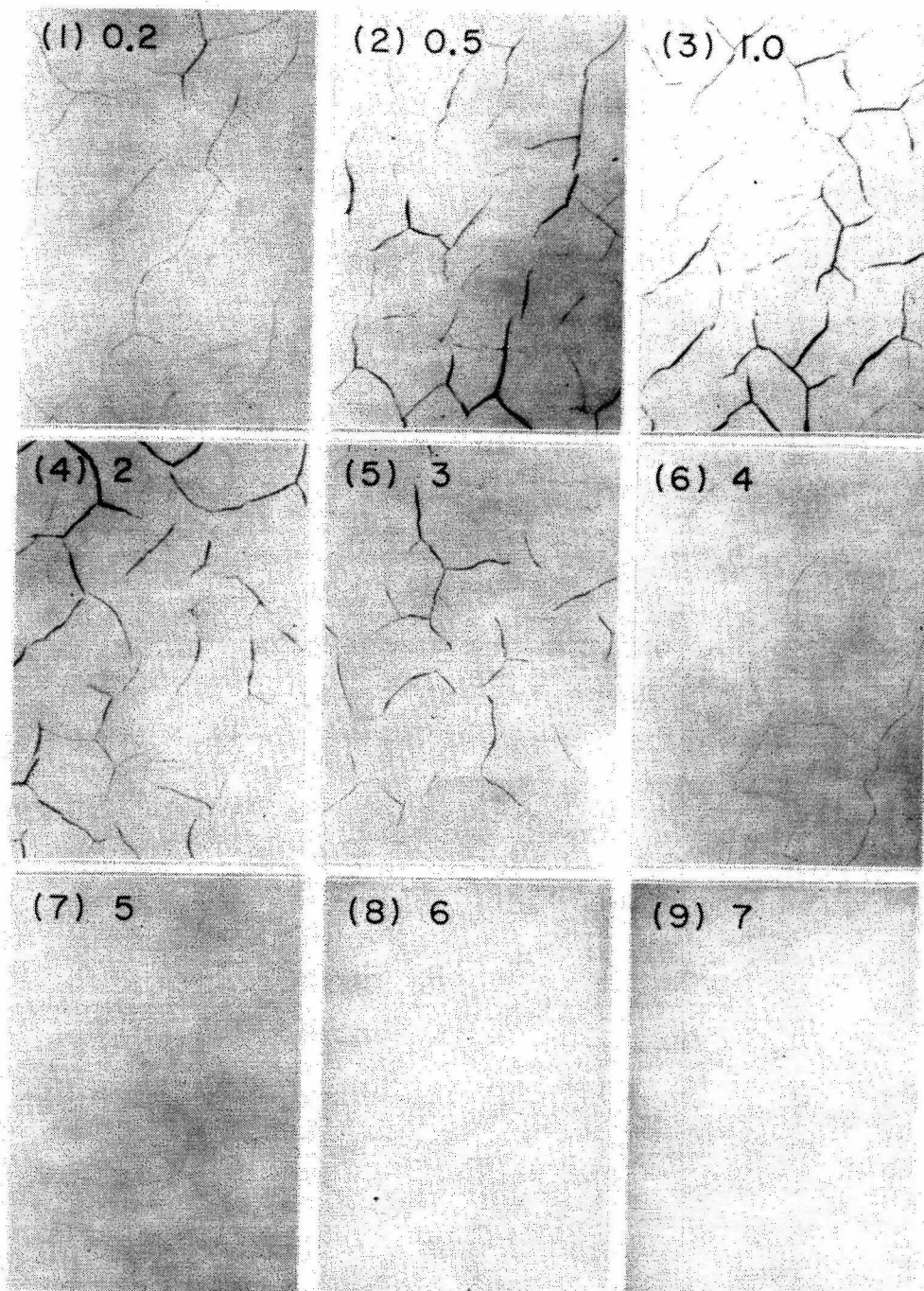


Figure 2(b). The scratch widths as a function of beam dose. Corresponding tape test results are shown in the figure.



**Figure 3.** Surface crazing of vitreous  $\text{SiO}_2$  due to the nonuniform stress relaxation from ion bombardment. The cracks produce an electrostatic edge field, which gives rise to higher adhesion of Au films (Wi85a). The cracks close up at a high dose ( $>5 \times 10^{13} \text{ cm}^{-2}$ ), because the bombarded region becomes more uniform due to the overlapping of cylindrical ion tracks. The numbers in the picture are bombarding ion doses in units of  $10^{13} \text{ cm}^{-2}$  of  $15 \text{ MeV Cl}^{+4}$ .

conventional category of the ionizing beam-induced enhanced adhesion.

## 2. Experiment and Results<sup>1</sup>

GaAs wafers with four different dopants, as shown in Table II, were cleaned in Alconox detergent and warm water in an ultrasonic bath, rinsed in warm water, in deionized water, and in methanol, etched in a solution of 3-5 drops of bromine in 100 ml methanol, rinsed in methanol, and dried in a dry N<sub>2</sub> flow. The cleaned wafers were loaded into a diffusion-pumped vacuum chamber in which about 500 Angstrom thick Au films were deposited by a resistive evaporation. The Caltech EN-tandem Van de Graaff accelerator was used to bombard samples with F<sup>19</sup> or Cl<sup>35</sup> ions for energies between 2 and 18 MeV. The bombardment dose varied from 8×10<sup>11</sup> to 2×10<sup>15</sup> ions/cm<sup>2</sup>. After the bombardment the film surfaces were cleaned by a plasma etching technique to avoid the influence of hydrocarbon contaminants on the "Scratch" test.

The adhesion test was done using a Leitz micro-hardness tester equipped with either a 0.5 mm radius chrome plated steel ball tip or a 0.4 mm radius tungsten carbide ball tip. The ball tip was loaded with a weight ranging from 5 g to 500 g, and samples were mounted on a motor driven translation stage. Figure 4 shows scratches made by the ball tip across the ion beam spots. The beam spot size is 1.2 mm radius. The letters a, b, c, and d indicate the beam spots of doses 25, 10, 5, and 2.5×10<sup>13</sup> ions/cm<sup>2</sup> of 18 MeV Cl ions, respectively. The scratches shown in the picture were made with a .4 mm tungsten carbide ball tip with various loads. The loads are not in order in the picture.

The results of the "Scratch" test are given in Figure 5 for the four different GaAs substrates bombarded with 18 MeV Cl ions. The bottom of

---

<sup>1</sup>Part of the results on Au-GaAs has been published (Li84).

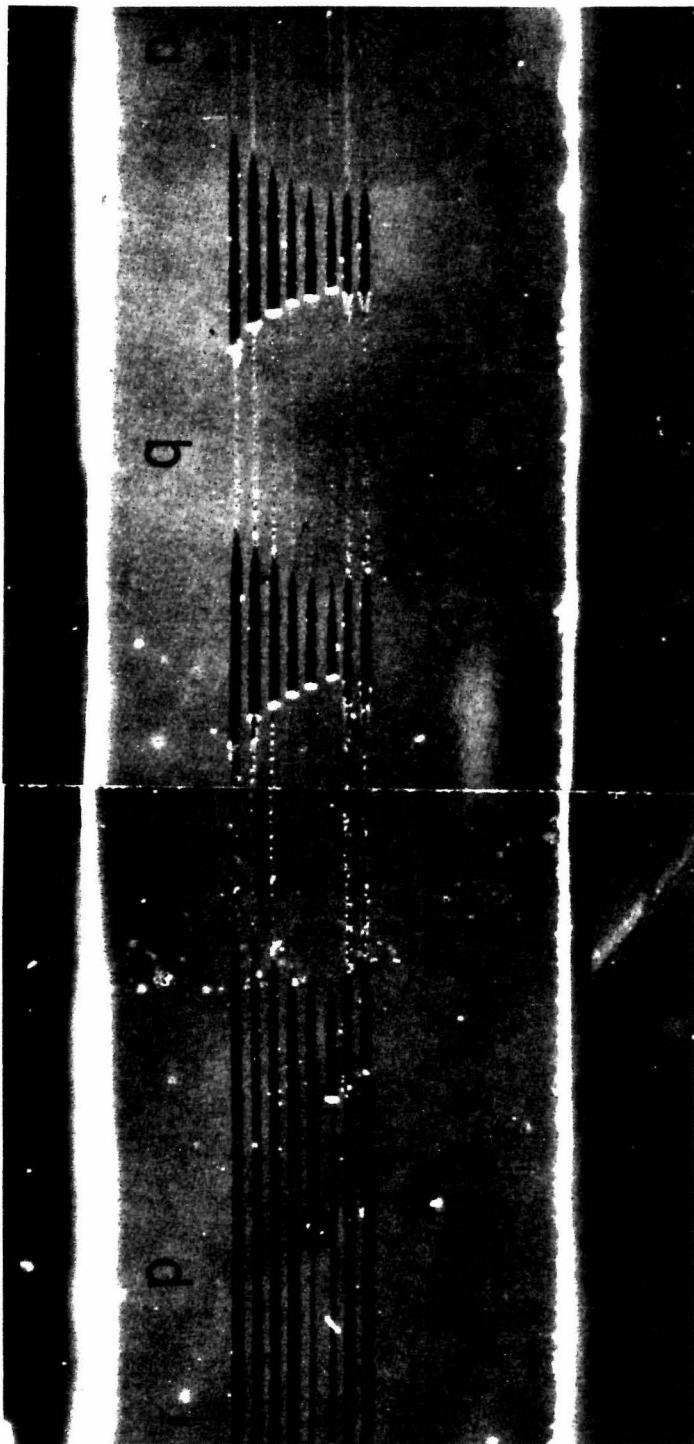


**Figure 4.** Scratches made in the Au films on GaAs, with .4 mm radius WC ball tip. The letters a, b, c, and d indicate 25, 10, 5, and  $2.5 \times 10^{13}$   $\text{cm}^{-2}$  doses of 18 MeV Cl ion. Film was stripped from the dark areas.

**Table II.** Properties of the GaAs substrates used for studying adhesion enhancement of Au films by MeV ion bombardment. All wafers are <100> cut.

Dopant	Concentration( $\text{cm}^{-3}$ )	Mobility ( $\text{cm}^2/V\cdot\text{s}$ )	Resistivity ( $\text{Ohm}\cdot\text{cm}$ )
Si(n)	$3.5 \times 10^{18}$	1350	$1.0 \times 10^{-3}$
	* $7.0 \times 10^{17}$	1100	$8.0 \times 10^{-3}$
Te(n)	$5.0 \times 10^{17}$	2100	$3.0 \times 10^{-3}$
	* $8.0 \times 10^{17}$	2540	$1.4 \times 10^{-3}$
Cr(p)	compensation doped		
Zn(p)	$7.0 \times 10^{17}$	1000	$9.6 \times 10^{-3}$

\*Used for the energy dependence measurements.

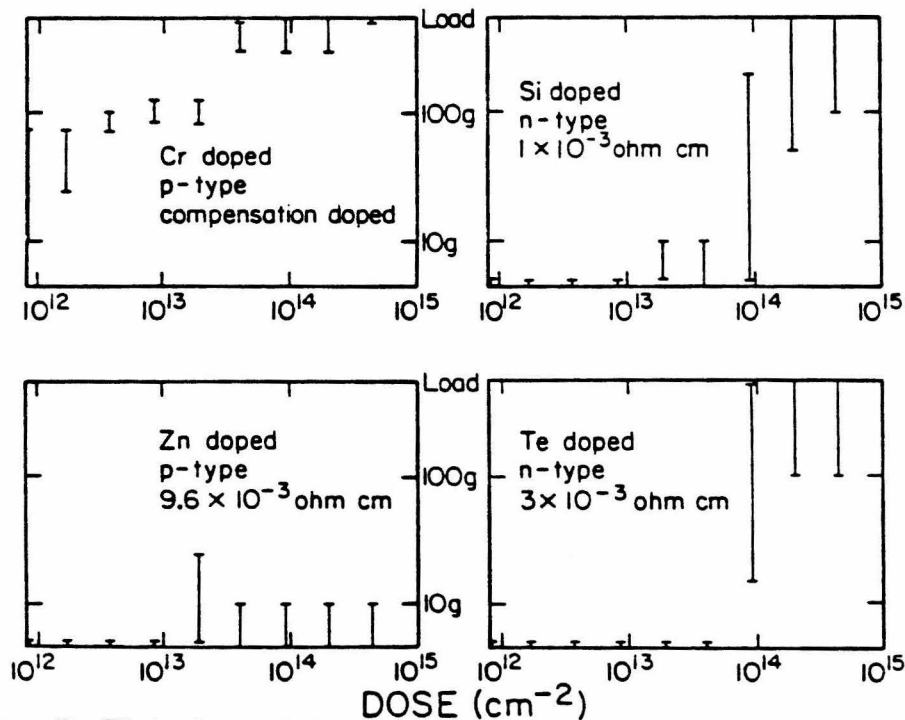


**Figure 5.** Plot of scratch test load that causes film stripping from GaAs substrate. The bars indicate the load range, from initiating of partial stripping (bottom of bar) to total stripping (top of bar)

the bars indicate the load at which the film starts to be partially removed and the top of the bars indicates the load at which the film is totally removed (the critical load). At the critical load, the scratch width is the same in both the bombarded area and the unbombarded area. In all the samples, the unbombarded films could be removed at 5 g, the lowest weight used. It can be seen in Figure 5 that only the Cr-doped semi-insulating GaAs sample shows a substantial increase in the adhesion for low bombardment doses ( $< 5 \times 10^{13}$  ions/cm<sup>2</sup>). On the other hand, the Zn-doped p-type sample does not exhibit any significant enhancement even for a high dose irradiation, at which all the other samples exhibit a large enhancement.

This result illustrates very well the dependence of the adhesion enhancement on the substrate electronic properties. The two n-type semiconducting substrates show very similar behavior, whereas the Zn-doped p-type semiconducting substrate sample shows very little enhancement and the Cr-doped p-type semi-insulating substrate sample shows a significant increase from a very low dose. This behavior correlates well with the XPS measurements of oxide layers at the interface. The XPS results are discussed later in this section. We must note that all the GaAs wafers were cleaned and deposited at the same time under identical conditions.

Using n-type GaAs substrates we measured the threshold beam dose as a function of ion energy. The threshold dose corresponds to a beam dose at which the load required to remove films increases rather abruptly (see Figure 5). Figure 6 shows the "Scratch" test results for the energy dependence measurements. Table III summarizes the data. It can be seen in Figure 6 that the adhesion changes more gradually for F ions than for

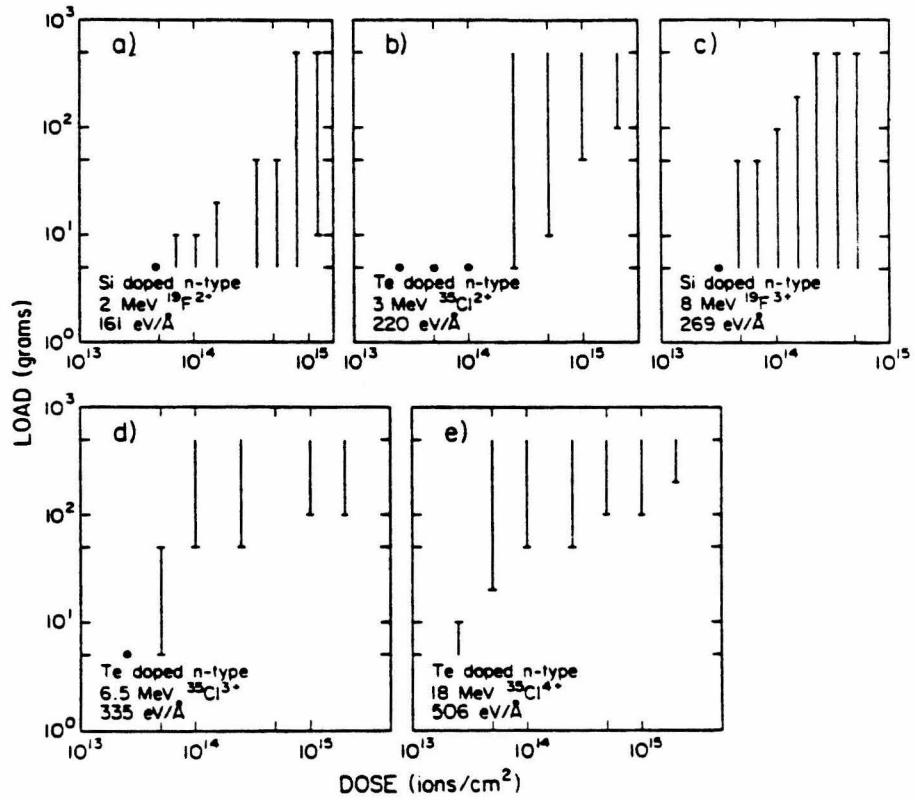


**Figure 6.** Plot of scratch test load range for the energy-dependence measurements.

**Table III.** GaAs and bombarding ion characteristics, electronic stopping power of bombarding ion at film-substrate interfaces, and the threshold for the onset of beam induced adhesion enhancement.

GaAs Substrate	Bombarding ion Characteristics	Electronic Stopping Power(eV/Å)	Adhesion Enhancement Threshold(ions/cm <sup>2</sup> )
Si doped	2.0 MeV, <sup>19</sup> F <sup>2+</sup>	161	(3.5 - 12) × 10 <sup>14</sup>
Te doped	3.0 MeV, <sup>35</sup> Cl <sup>2+</sup>	220	2.5 × 10 <sup>14</sup>
Si doped	8.0 MeV, <sup>19</sup> F <sup>3+</sup>	269	(4.7 - 25) × 10 <sup>13</sup>
Te doped	6.5 MeV, <sup>35</sup> Cl <sup>3+</sup>	335	1.0 × 10 <sup>14</sup>
Te doped	18.0 MeV, <sup>35</sup> Cl <sup>4+</sup>	506	5.0 × 10 <sup>13</sup>



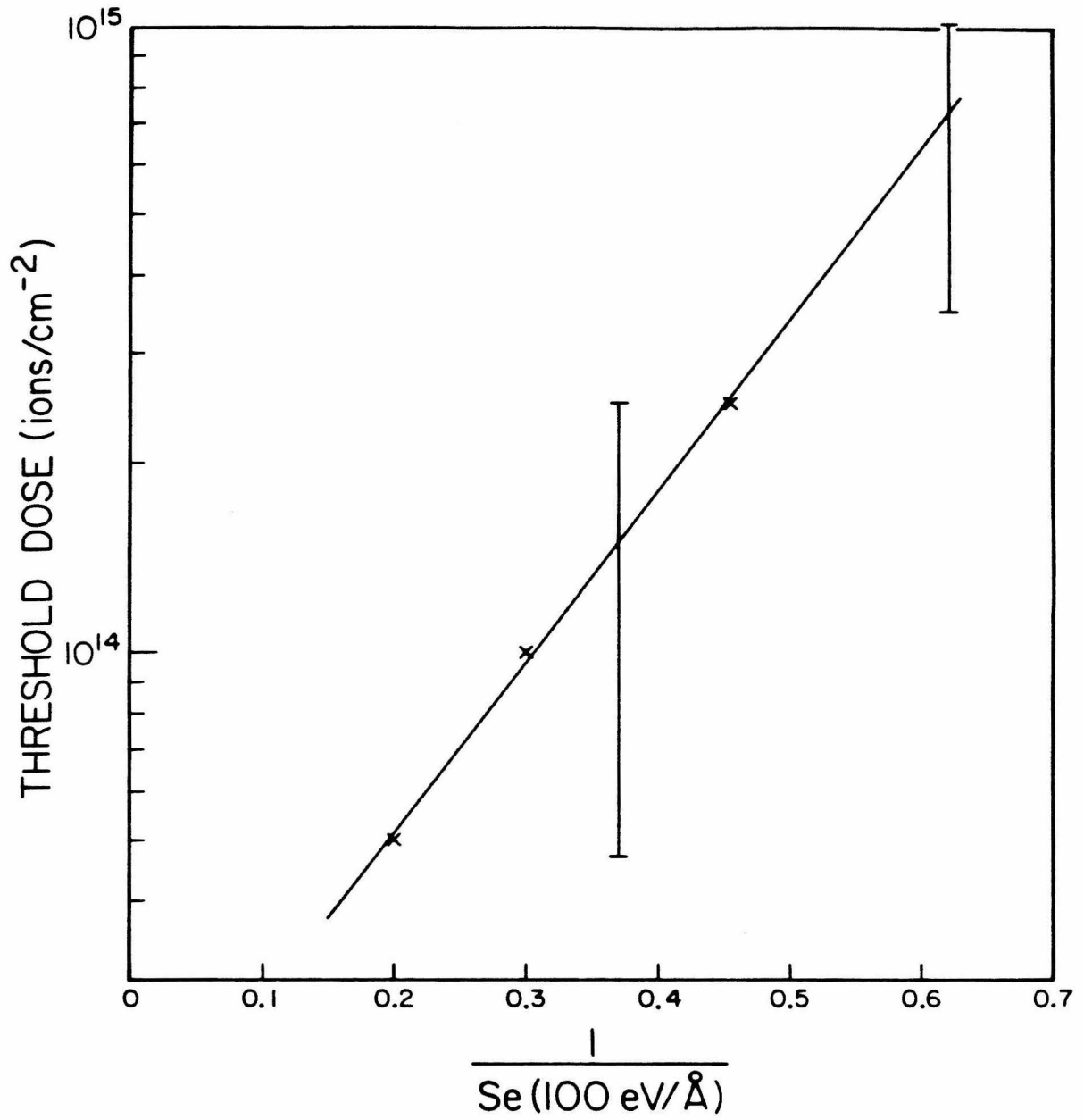


**Figure 7.** Plot of the threshold dose against electronic stopping power, from Table III. The solid line through the data represent the exponential dependence of  $D_{Th}$  on  $1/Se$ .

Cl ions. In Figure 7 the threshold beam dose is plotted against the electronic stopping power (see also Table III). The straight line corresponds to an exponential dependence of the threshold dose on  $1/Se$ . Here, the electronic stopping power values,  $Se$ , were taken from the data table by Northcliffe and Schilling (No70). This dependence is explained by a model, which will be discussed in the next section.

The dependence of adhesion enhancement on substrate electronic properties was a most interesting result. We investigated a possible difference in chemical compositions at the interface region using XPS<sup>2</sup>. The XPS technique measures the photoelectrons emitted from the first few atomic monolayers of solid surfaces by x-ray photons, and the escape depth for photoelectrons in the 1-2 keV energy range is typically 10-20 Angstroms (Gr79a). Thereby, the XPS technique provides chemical information about the surfaces of solid.

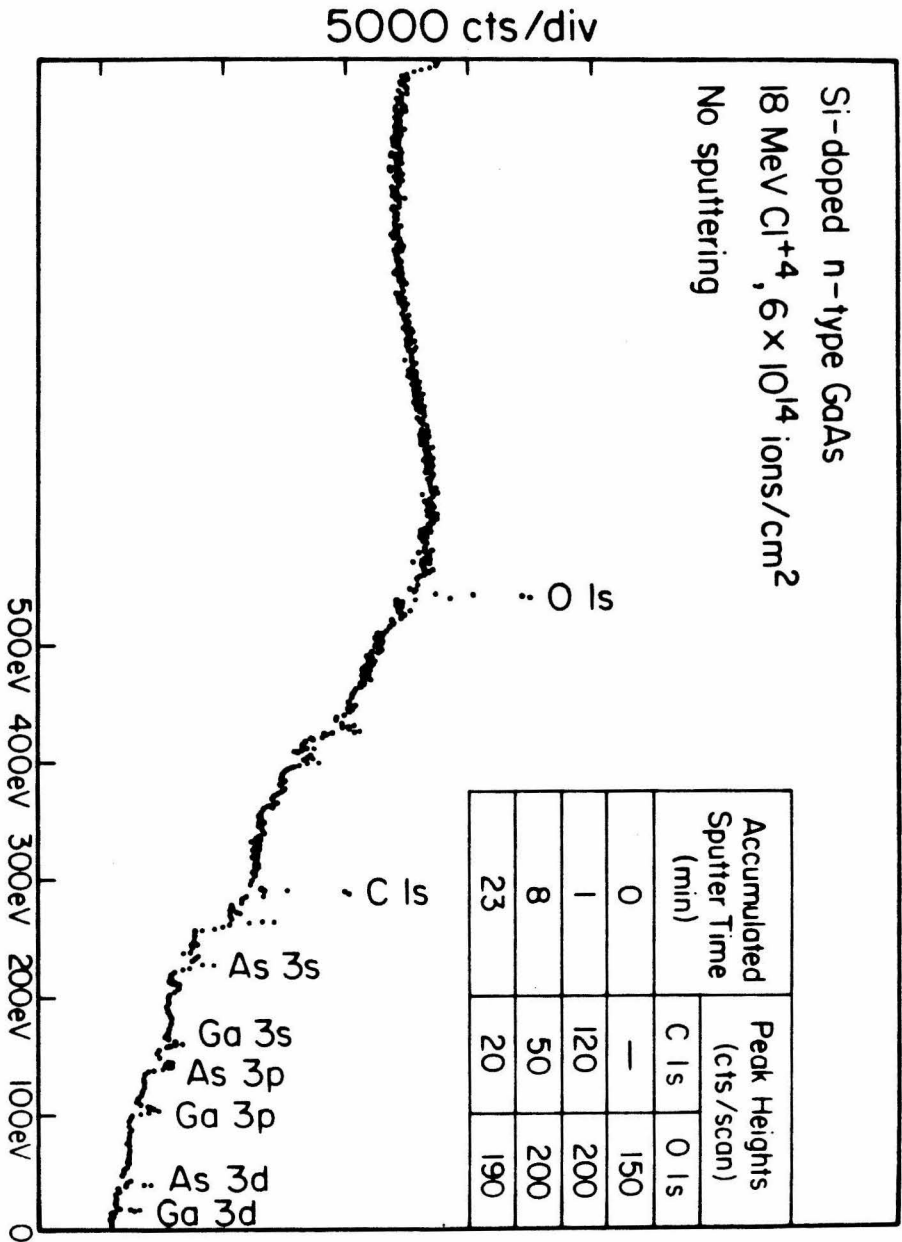
For the XPS measurement, Si-, Zn-, and Cr-doped GaAs substrates were cleaned and deposited with Au films at the same time under identical conditions. The bombarded and as-deposited samples were etched in a dilute solution of KCN in water to remove Au films (KCN is known to etch Au selectively). After removal of Au films, the samples were loaded into the XPS apparatus. The ESCA spectra were obtained from the as-loaded samples. Subsequently, these samples were sputter etched *in situ* with Ar ions.

Figure 8 shows an ESCA spectrum taken (before sputter etching) from a Si-doped GaAs substrate bombarded to  $6 \times 10^{14}$  ions/cm<sup>2</sup> with an 18 MeV Cl ion beam. The strong O 1s signal was typical for all the bombarded

---

<sup>2</sup>The XPS measurements were performed in a collaboration with R. Grant and R. Housley at Rockwell International Science Center in Thousand Oaks, CA.

# SAMPLE ESCA SPECTRUM



**Figure 8.** An ESCA spectrum taken before sputter etching from an n-type GaAs(Si) sample bombarded with MeV ions. The Au film had been removed by dilute KCN solution in water. The sputtering results for C 1s and O 1s lines are given in the inset.

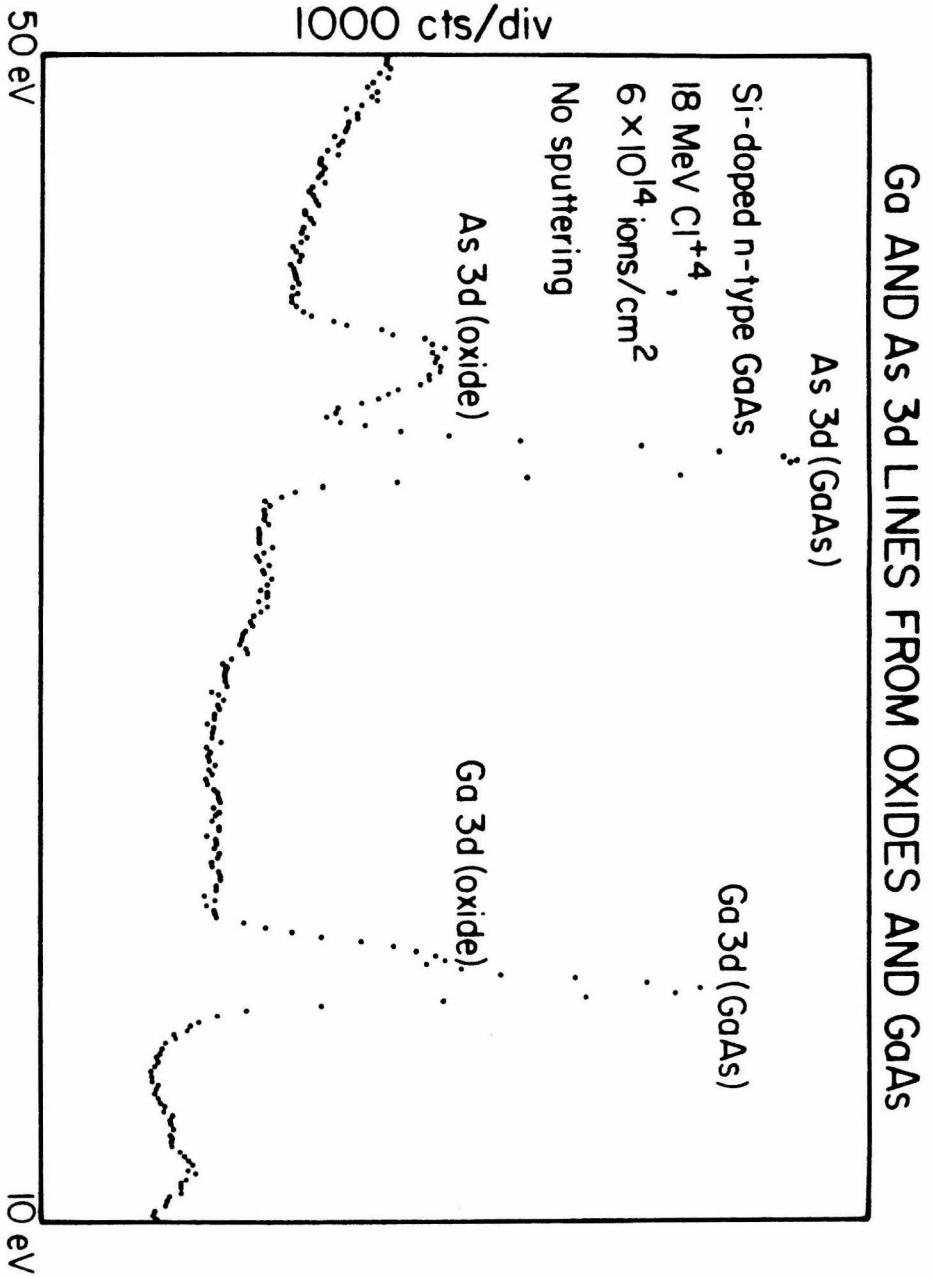


**Figure 9.** Enlarged ESCA spectrum for Ga 3d and As 3d lines. Oxide satellite signal is resolved for As, but not for Ga.

samples. Shown in the inset are the sputtering results for the O 1s and C 1s lines. Carbon existing on the sample surfaces is largely due to the contamination, and is removed by 23 minutes of sputtering. However, the oxygen signal virtually did not change after the same sputtering. For the unbombarded sample it was found that the oxygen signal decreased rather rapidly with sputtering.

To look at the oxygen signal variation with substrate electronic properties, we started with Si-doped n-type and Zn-doped p-type substrates which had been bombarded with 18 MeV Cl ions to  $3 \times 10^{14}$  ions/cm<sup>2</sup>. One unbombarded Si-doped n-type sample was also examined. The ESCA spectra from these samples are discussed below.

Figure 10 shows peak heights of the O 1s line as a function of sputtering time. It can be seen that the oxygen signal heights are well correlated with the "Scratch" test results shown in Figure 5. It is also noted that the oxygen concentration extends into deeper regions in the bombarded samples than in the unbombarded sample, and it extends deeper in the Si-doped substrate than in the Zn-doped substrate. The *in situ* sputtering was performed simultaneously for all three samples in the same Ar ion beam.

Table IV gives the peak heights of As 3d, O 1s, and C 1s lines for increasing sputter time. As can be seen from Figure 9 the As 3d lines are resolved for oxide and GaAs, whereas the Ga 3d lines are not. One thing we should note is that arsenic oxides dissolve in water and gallium oxides do not. The arsenic signal from arsenic oxide in Table IV is probably from the native oxide layer which was formed after the Au film was etched off with the KCN solution, and this signal goes away much earlier than the oxygen signal.

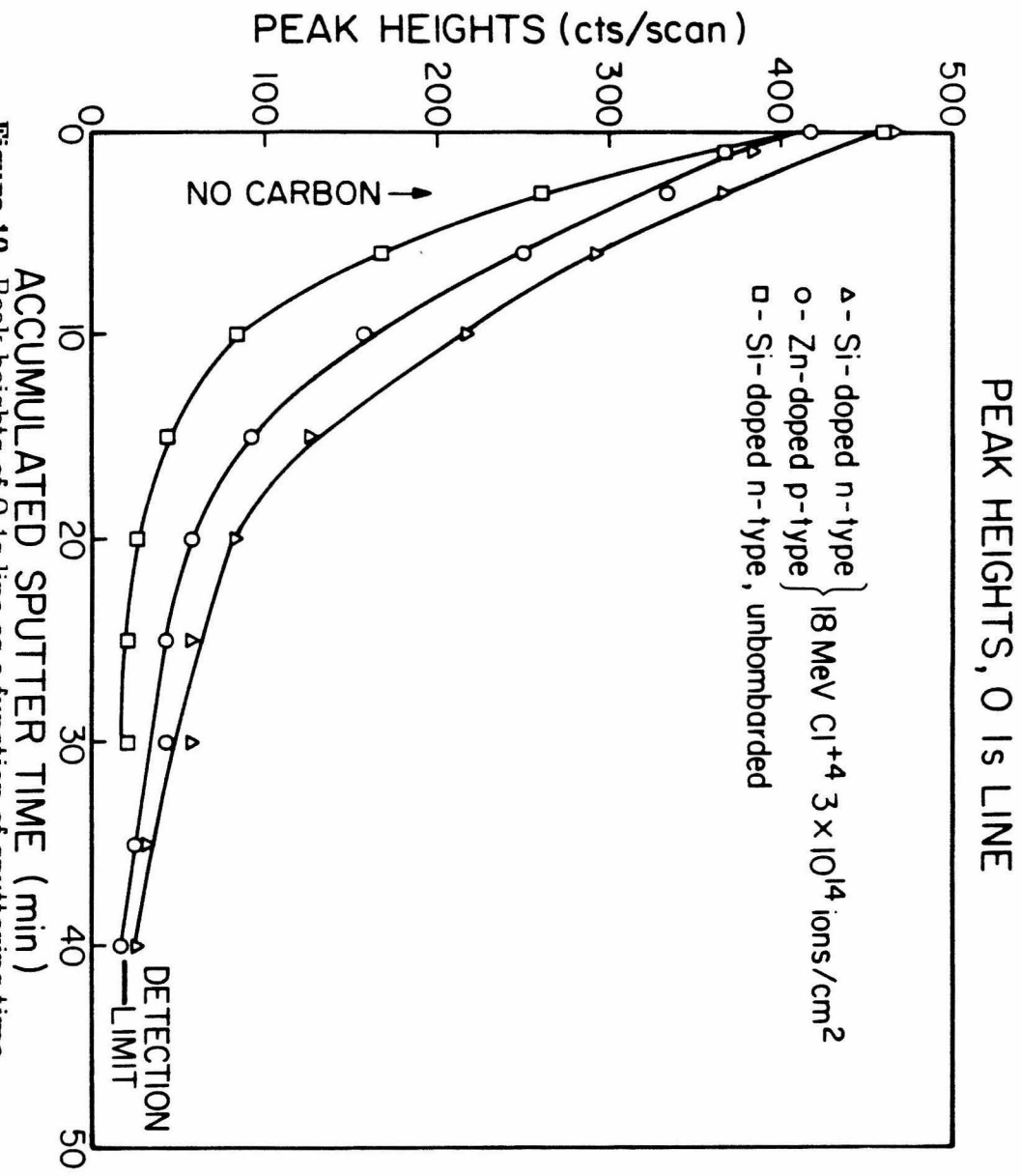


**Figure 10.** Peak heights of O 1s line as a function of sputtering time. The data are to compare the oxygen concentration for different substrates, and for before and after the ion bombardment.

**Table IV.** Peak height data for bombarded and unbombarded GaAs substrates with different dopants.

Sputter Time (min.)	Si-doped n-type GaAs Accumulated 18 MeV Cl <sup>+</sup> , 3x10 <sup>14</sup> cm <sup>-2</sup>				Zn-doped p-type GaAs 18 MeV Cl <sup>+</sup> , 3x10 <sup>14</sup> cm <sup>-2</sup>				Si-doped n-type GaAs Unirradiated			
	As3d (GaAs)	As3d (Oxide)	O1s	C1s	As3d (GaAs)	As3d (Oxide)	O1s	C1s	As3d (GaAs)	As3d (Oxide)	O1s	C1s
0	193	93	467	110	200	70	417	90	230	72	460	104
1	277	75	383	36	260	50	367	24	323	25	367	15
3	313	27	367	0	327	20	333	0	375	0	260	0
6	342	0	293	--	340	0	250	--	400	0	167	--
10	342	0	217	--	356	0	158	--	383	0	83	--
15	353	0	127	--	403	0	92	--	408	0	43	--
20	--	--	83	--	--	--	58	--	--	--	≈25	--
25	--	--	57	--	--	--	42	--	--	--	≈20	--
30	--	--	56	--	--	--	42	--	--	--	<20	--
35	--	--	≈30	--	--	--	≈25	--	--	--	--	--
40	--	--	<25	--	--	--	<17	--	--	--	--	--

Since the gallium oxides do not dissolve in water during the removal of Au films, they provide a better measurement for the oxide compound formed by the MeV ion irradiation. We therefore measured the linewidths of the Ga 3d line. The linewidths at half peak are shown in Figure 11 for the same samples from which the O 1s peak heights were obtained (see Figure 10). The variation of the Ga 3d linewidths as a function of sputter time, and for different samples is consistent with the O 1s signal height data and the "Scratch" test results. This is evidence that the oxygen in irradiated samples exists as a compound with the substrate atoms. Note that the As 3d linewidths do not change with sputtering, because this line is resolved for oxide and GaAs.

Figure 12 shows the lineshape of Ga 3d line for the bombarded Si- and Zn-doped substrates. The lineshape is more asymmetric even after longer sputtering for the Si-doped substrate than for the Zn-doped substrate. This also indicates that the oxide concentration is higher in the Si-doped GaAs than in the Zn-doped GaAs.

In an effort for more quantitative analysis, rough chemical compositions were obtained from the signal height measurement for the Si-doped substrates. After 6 min. sputtering, when the native oxides and carbon contaminants have been removed, the atomic percents are 32% As, 41% Ga, and 27% O for the bombarded substrate, and 39% As, 45% Ga, and 16% O for the unbombarded substrate. Data indicate  $\text{Ga}(\text{OH})_3$  formation rather than  $\text{Ga}_2\text{O}_3$ . Thus a hydrogen profiling measurement would be interesting. Continuing work is under way in this respect, but data are not available for this thesis.

We close this section by mentioning an observation that was made during the selective etching of Au films in a dilute KCN solution. Complete



### LINEWIDTHS OF Ga AND As 3d LINES

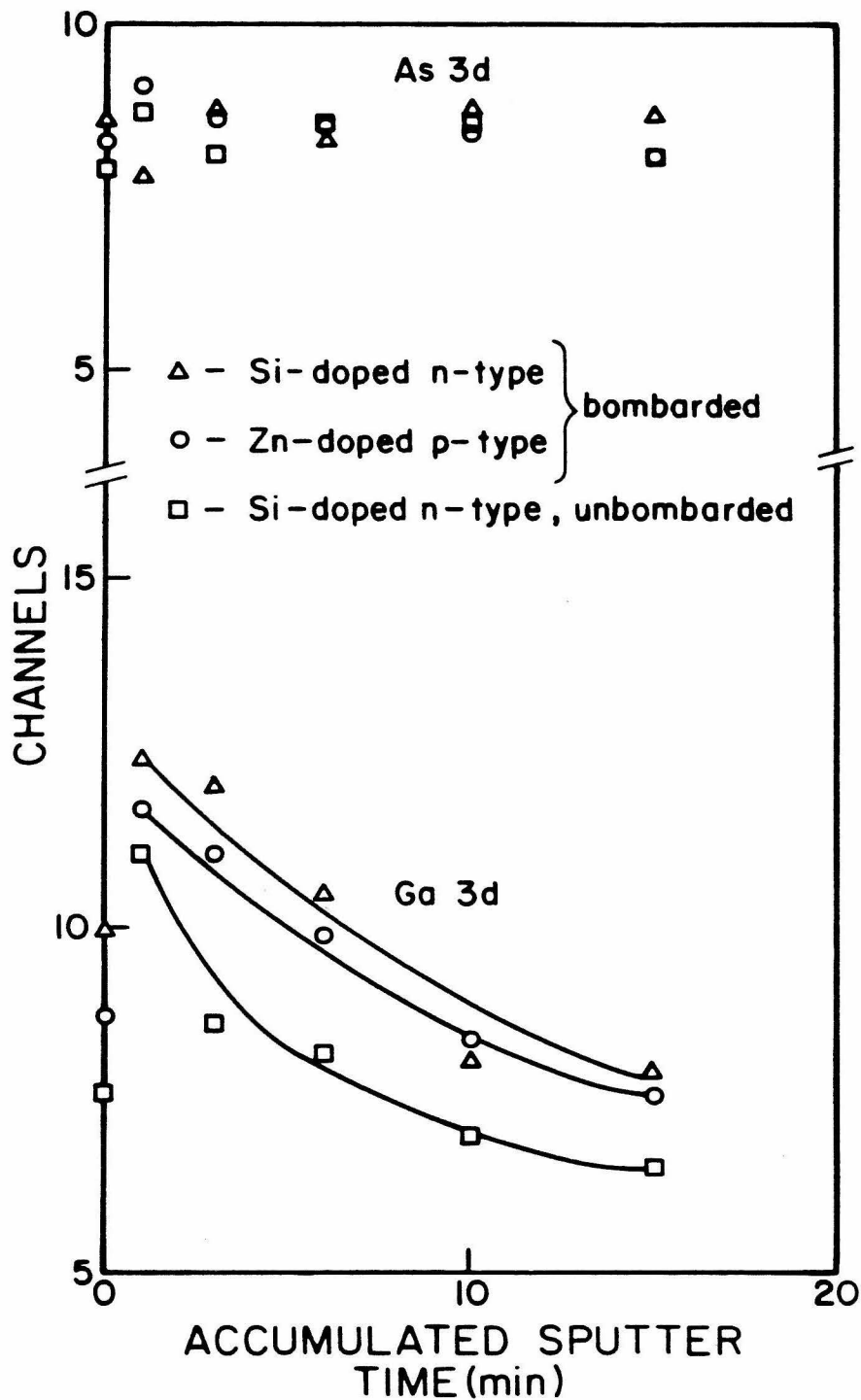
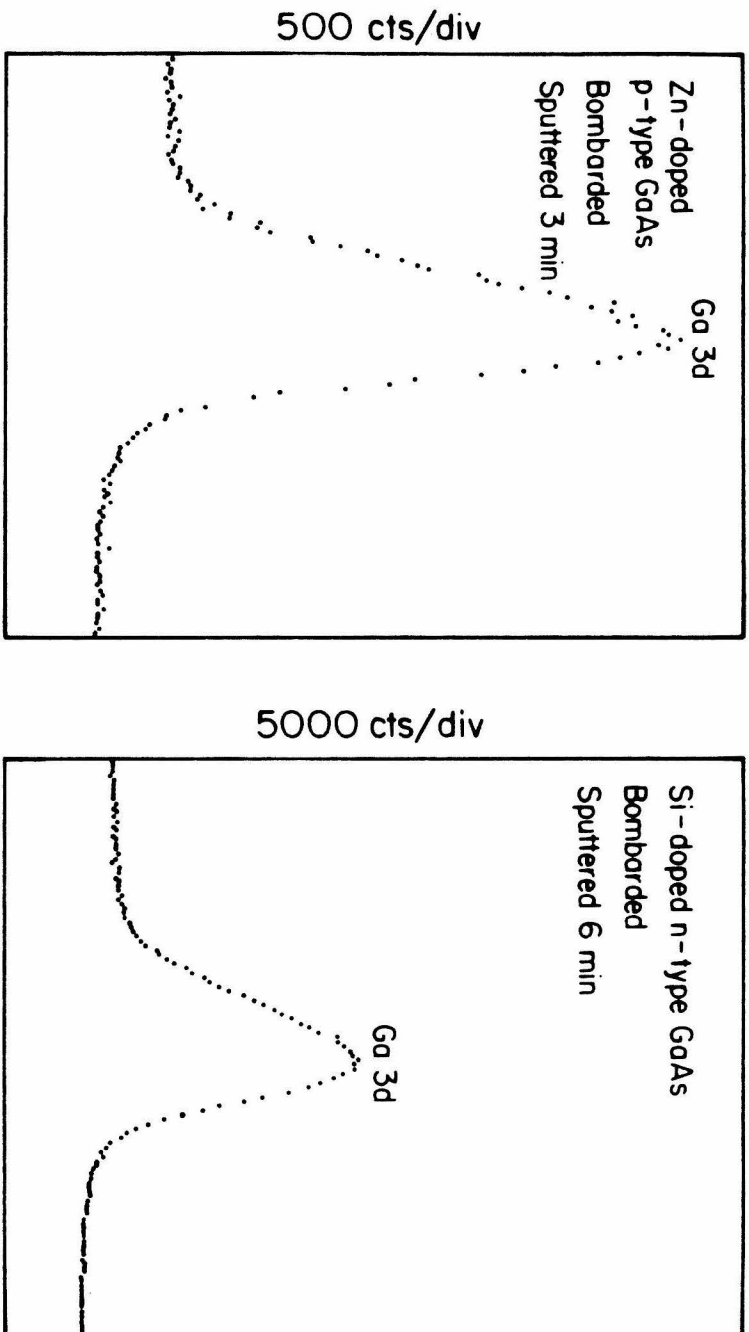


Figure 11. Linewidths at half-peak versus sputtering time for Ga 3d and As 3d lines.

ASYMMETRY OF Ga 3d Lines  
FROM Si-doped AND Zn-doped SUBSTRATES



**Figure 12.** Lineshape of Ga 3d line for Si-doped and Zn-doped GaAs. Total sputter time before the data were taken is indicated in the figure.

removal of Au films from the substrates was in order of adhesion strength, i.e., unbombarded Si-doped sample, bombarded Zn-doped sample, and bombarded Si-doped sample. The bombardment beam dose was  $3 \times 10^{14}$  ions/cm<sup>2</sup> for both bombarded samples. At the last instant of removal, the unbombarded films were cracked and taken off as small pieces, and so were the bombarded films on the Zn-doped substrate. However, the bombarded films on the Si-doped substrate were removed fairly continuously without cracking. Even though the deposition of hydrocarbon contaminants during beam bombardment may decrease the etching rate, this cracking behavior may be related to the bonding strength of the films to the substrate.

### 3. Discussion and Model

The dependence of adhesion enhancement on the substrate electronic properties (see Figure 6) was shown to be related to the oxide concentration (see Figure 10) which is chemically bound to the substrate atoms in the interface region. The XPS data provide a rough measurement of the total oxide layer thickness after the beam bombardment which is about a factor of two higher than the native oxide layer thickness (i.e., before beam bombardment).

Thin native oxide layer does not exhibit any enhanced sputtering yield under MeV ion bombardment when they exist on a semiconducting substrate (Qi83). The critical thickness of the insulating film on a semiconducting substrate, to give rise to enhanced sputtering, is estimated to be 3 atomic monolayers in their paper by Qiu et al. Thus, the sputtering mechanism of MeV ions in insulators may not be responsible for the small mixing of oxides and substrate surfaces by the beam bombardment. Also, when the insulator layer in a metal-insulator-semiconductor structure is very thin (less than 10 Angstroms), little impediment is provided to carrier transport between the metal and the semiconductor(Sz81).

The XPS data suggest that the adhesion enhancement between the Au film and the GaAs substrate is provided by chemical bond formation of the impurity oxides with the substrate atoms (and most likely with the thin film atoms also), with a beam-induced mixing on the order of the native oxide layer thickness. Now, a model for the Au-GaAs system is discussed which is based upon the adhesion enhancement model originally proposed by Tombrello (To83).

At the beam current densities employed each ion interacts independently, so any new bonds created (i.e., any increased adhesion) must be proportional to the bombardment beam dose. Thus, if we define the threshold dose as the dose at which the load on the "Scratch" test increases rather abruptly, then

$$\begin{aligned} (\text{New bonds per event}) \times (\text{Threshold dose}) &= \text{a constant which} \\ &\text{depends on the} \\ &\text{adhesion test alone} \end{aligned}$$

The number of new bonds of the impurity oxides produced with the substrate atoms or the thin film atoms is assumed to be proportional to the electron current flowing across the interface layer caused by the bombarding ion. This is because, to form new bonds, one must first free the electrons and exchange them among the participating atomic species, and because the electron exchange of the impurity oxides with the film/substrate atoms will be governed by the electrons, freed by the electronic collisions of the ion and flowing between the substrate and the metal film. Since the impurity oxide layer provides little impediment to the carrier transport, we can use the Richardson-Dushman equation for thermionic emission:

$$\text{electron current} \propto T^2 \exp\left(-\frac{\varphi}{T}\right).$$

The temperature for the electrons is taken to be provided by various energy loss process of the ion in the electronic collisions, i.e.,  $T \propto Se$ . The  $\varphi$  is taken to be approximately the difference in work functions of the thin film and the substrate. Since the dominant dependence is from the exponential term, the threshold dose,  $D_{Th}$ , is:

$$\text{Log}(D_{\text{Th}}) \propto \frac{1}{\text{Se}}.$$

In Figure 7 the experimental data are provided. The solid curve through the data points is for an exponential dependence of the threshold dose on  $1/\text{Se}$ . This rather simple model provides the correct dependence of the threshold dose on the electronic stopping power for the Au on n-type GaAs system. For the doping concentration of GaAs substrates given in Table II, the work function difference is roughly .7 eV for Au (with the work function of 4.8 eV) and n-type GaAs(Te), and .6 eV for Au and p-type GaAs(Zn). The marked difference of adhesion enhancement between these two substrates, as shown in Figure 6, may not be explained by this work function difference. The adhesion enhancement for p-type GaAs(Zn) as a function of beam dose suggests rather that the remarkable difference is due to the difference in the native oxide thickness among the different substrates. With more oxides available for new bond formation, the adhesion enhancement will be higher, thus explaining the substrate electronic property dependence. The variation of the oxide concentration with the substrate electronic properties was clear from the data in Figure 10 and in Table IV.

This model needs to be refined to account for the small oxide diffusion into the substrate by the ion bombardment, and this may require one to consider, for example, the heat of mixing.

In conclusion, we demonstrated that in the ionizing beam-induced adhesion enhancement the role of an impurity oxide layer is important, and the "Scratch" test results for the Au and n-type GaAs system support the proposed adhesion mechanism by Tombrello. Also, the data suggest that more extensive investigation of the oxide compounds formed by the MeV ion irradiation is necessary for the metal-metal, and other metal-

semiconductor systems to understand more rigorously the adhesion mechanism. If one uses an ultrahigh vacuum for the thin film deposition, the ionizing beam-induced solid state reaction between the atomic species of the thin film and the substrate will provide an exciting field to study.

### III. Strain/Damage in MeV Ion Bombarded GaAs

#### 1. Introduction

In this chapter we present research performed on the radiation damage in GaAs and in other crystalline materials bombarded by MeV ions. The results on GaAs will be compared with those on other materials.

Principal measurements of the radiation damage were performed by measuring the x-ray lattice parameter change, and the average atomic displacements from regular lattice sites. Both quantities were measured experimentally by an x-ray rocking curve technique which gives a Bragg reflecting power of the samples as a function of angle.

In the Bragg reflection, the deviations of lattice parameter from an original value give rise to angular shifts in the reflection intensity. Random displacements of atoms from the lattice sites cause a decrease in the Bragg intensity and x-ray broadening. The x-ray rocking curve technique and data analysis will be described in the next section.

The radiation damage by MeV ions is intimately related to a partition of energy into electronic processes and lattice processes. Thus, we briefly present an overview of the energy partition and related effects in this section.

Figure 13 shows an example of the depth distribution of the stopping powers. As seen in the figure, the electronic stopping is dominant over the nuclear stopping over most of the range (marked as Region I), except the last less-than-one micron region (marked as Region II) where the nuclear stopping becomes comparable to the electronic stopping. This situation is typical for the MeV ions employed in this thesis. We thus describe a general aspect of radiation damage in Region I ( $S_n \ll S_e$ ), and



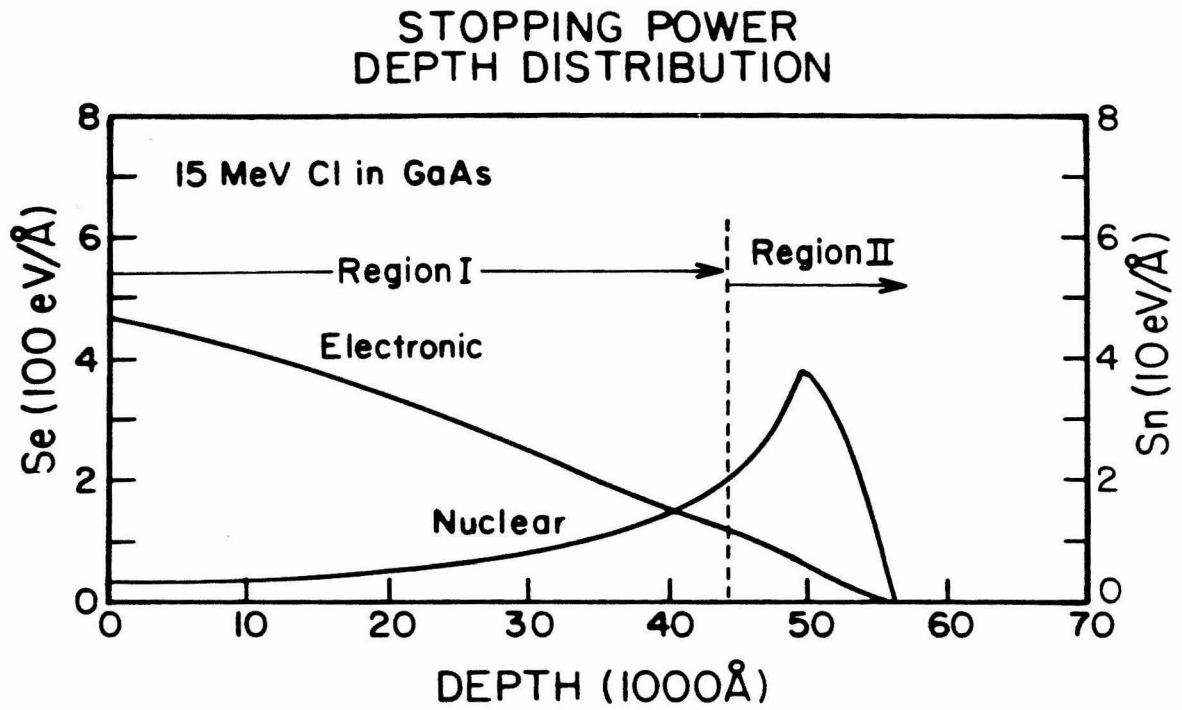


**Figure 13.** Depth distribution of stopping power for a 15 MeV Cl ion incident on GaAs.

in Region II (Sn ~ Se), for the materials which exhibit electronic erosion and for those which do not.

(1) Radiation damage in Region I: When the target materials are electrical insulators or some selected compound semiconductors (Mo68), some part of the energy in the electronic system couples to a lattice displacement process (Fl75). Thereby, it creates an elongated ion damage track in these materials, and it also produces an enhanced sputtering yield from the surfaces of these materials (To84b). In these track-forming materials, the theoretical approach to the ion erosion process is largely focused on the coupling mechanism of the energy deposited in the electronic system into lattice displacements (Fl75, To84a). The nature of the damage may be different for different materials. However, the general nature of the damage in the track-forming materials seems to be that it is composed of extended defect regions and point defects which continuously spread out in between the extended defects (Da81).

The electronic excitation/ionization-induced lattice displacements do not usually occur in metals and in most semiconductors. In these materials only the nuclear collision process is responsible for the displacement damage. Since the nuclear stopping power in Region I is on the order of the threshold displacement energy of atoms in the target materials, the damage is mainly composed of point defects.

The point defects in crystalline materials act as centers of lattice dilatation. A random uniform distribution of such point defects produces a dilatational strain which is uniform and isotropic in the entire specimen (Es56). If  $\Omega$  is the atomic volume,  $f_v\Omega$  is the volume change due to the dilatational field of one vacancy, and  $f_i\Omega$  is the volume change due to one interstitial, the strain is then

$$\varepsilon = \frac{\Delta a}{a} = \frac{1}{3}(c_v f_v + c_i f_i)$$

where  $c_v$  and  $c_i$  are the atom fractions of vacancies and interstitials (Si59).

Also the extended defects produce a strain field around them. For example, a nuclear damage track produces strain field which is expected to decrease as  $r^{-2}$  with the radial distance (F175).

The measurement of strain, induced by MeV ion irradiation, is suitable for the radiation damage study in this Region I.

(2) Radiation damage in Region II: This region corresponds to the ion energy of several hundred eV and below. In this region the nuclear collision energy loss is comparable to the electronic energy loss. Since nuclear collision is a much more efficient process in producing displacement damage than electronic collision, the radiation damage in this region is dominated by the nuclear process regardless of the target material properties.

The nuclear stopping power in this region is typically several tens of eV/Angstrom, and the radiation damage is composed of many isolated disordered regions produced by collision cascades. The radiation damage in this region is most important in ion implantation for semiconductor device processing. The use of the x-ray rocking curve technique for the ion implanted materials has been described by Speriosu et al. (Sp84).

## 2. Dynamical X-Ray Diffraction in Nonuniform Crystalline Films

### 2.1 Strain/Damage Measurement by X-Ray Rocking Curve Technique

An x-ray diffractometer system measures the Bragg reflection intensity as a function of angle (the x-ray rocking curve). A goniometer installed under a sample holder moves (i.e., rocks) the sample with respect to the incoming x-ray beam by a step angle typically of  $10^{-3}$  degrees. At each step the reflection intensity is measured and recorded by a computerized data acquisition system.

A schematic and picture of the equipment are shown in Figures 14(a) and 14(b). The beam emerging from the x-ray tube is diffracted by the first crystal. The x-ray beam becomes monochromatic, more planar, and partially polarized by the diffraction from the first crystal. This diffracted beam is incident onto the sample. The reflecting power is defined as the intensity ratio at the sample surface of the diffracted beam to the incident beam.

To analyze the strain induced in the surface layers of a crystal, the x-ray source should be chosen such that the x-ray absorption length is not much less than the total thickness of the strained layer. This is because the x-ray strain is obtained by measuring the angular shift of the diffraction pattern by the surface strained layers from the Bragg peak of the undamaged substrate.

The unpolarized x-ray beam emerging from the x-ray tube is partially polarized by a diffraction from the first crystal. This diffracted beam contains the normal polarization component which is a factor of  $(\cos 2\theta_{B_1})^{-2}$  higher than the parallel component, where  $\theta_{B_1}$  is the first crystal Bragg angle. The normal polarization is for the electric field vector which is

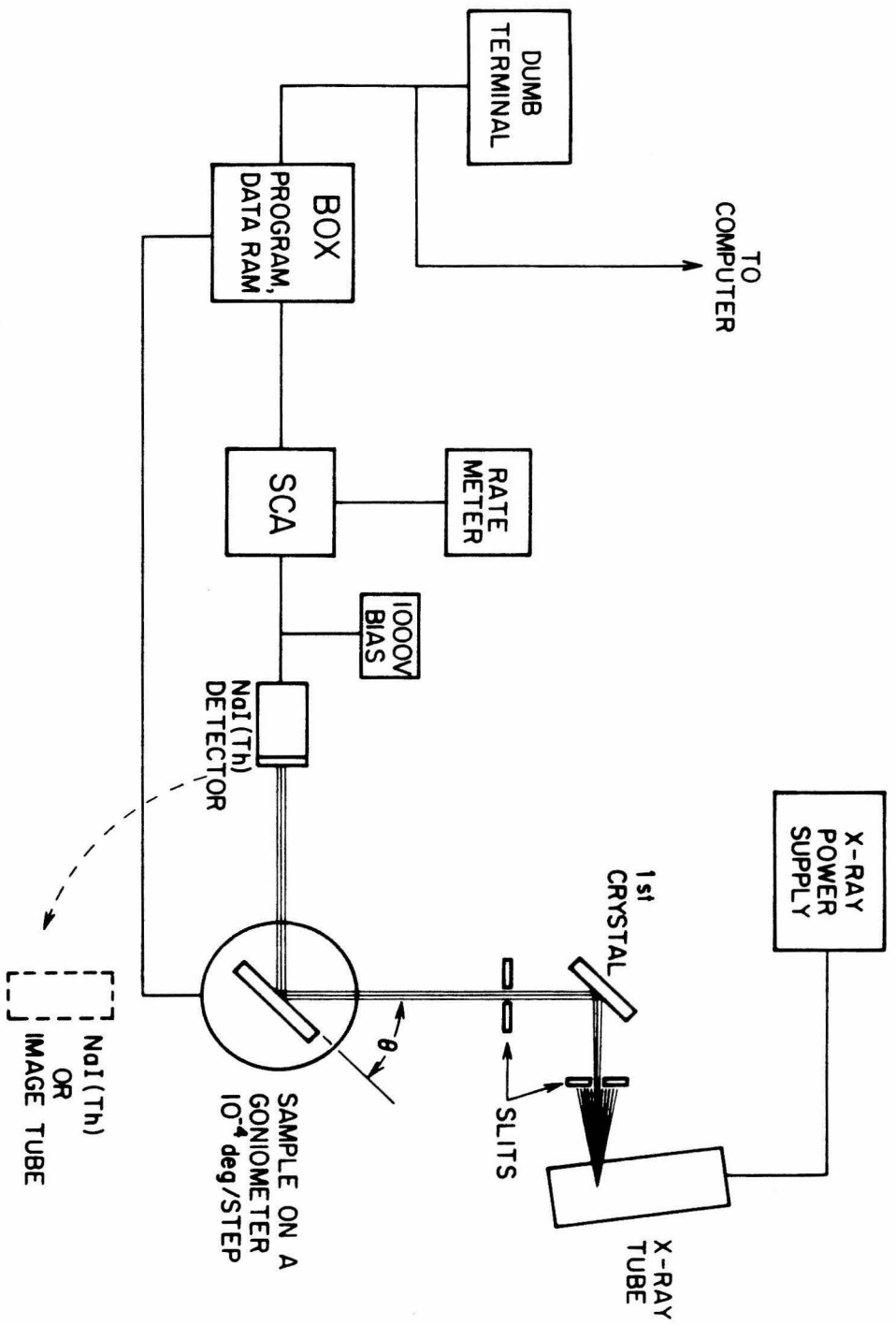
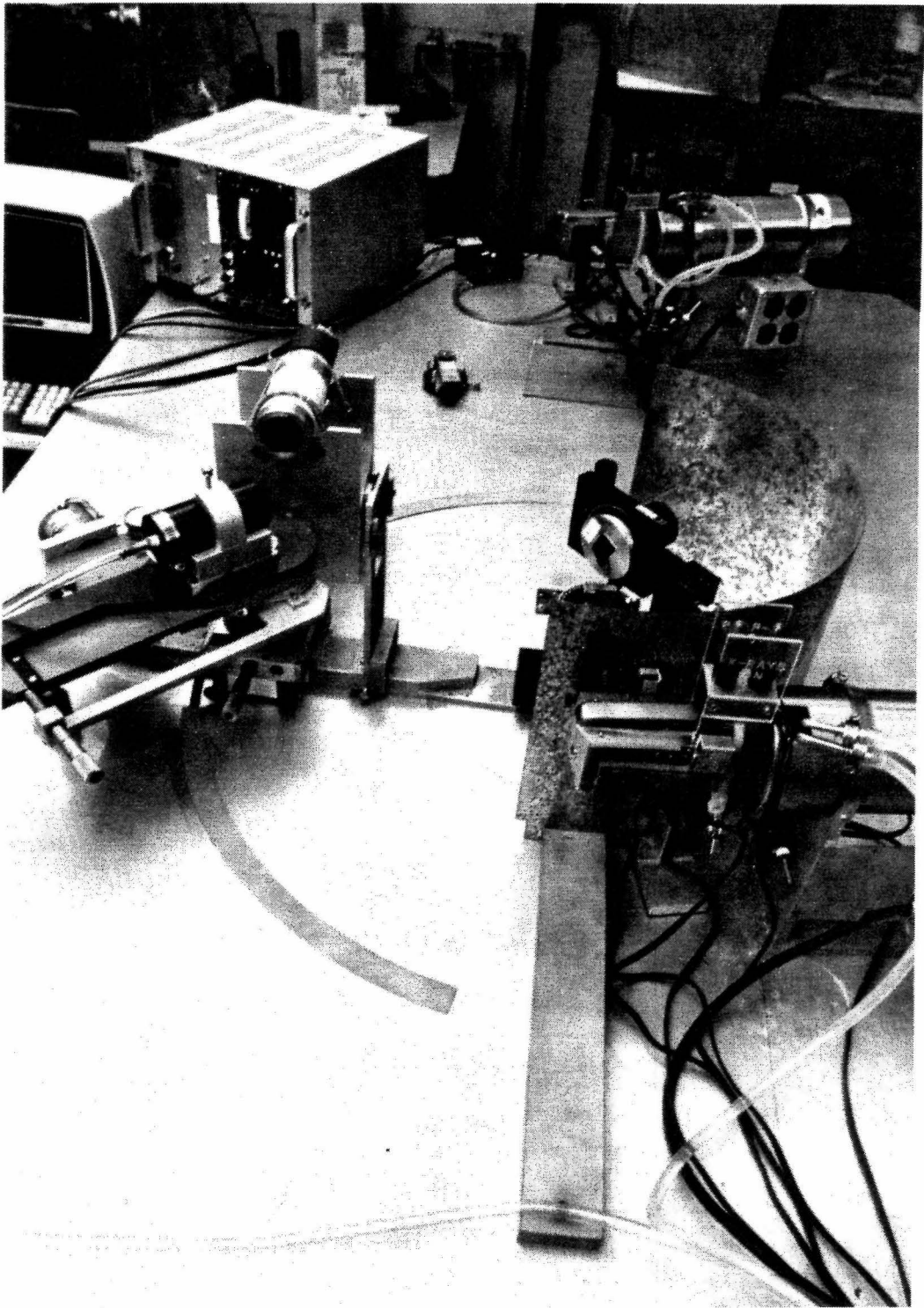


Figure 14(a). A schematic of rocking curve equipment.



**Figure 14(b).** Picture of rocking curve equipment. At center of the picture, the first crystal is seen. Sample crystal is mounted on the face of the black cylindrical tube shown on the left.

perpendicular to the plane defined by the incident and the diffracted wave vectors.

Also, the first crystal resolves slightly different wavelengths by reflecting to different angles. The x-ray beam coming off the first crystal usually contains two prominent wavelengths (e.g.,  $K\alpha_1$  and  $K\alpha_2$ ) propagating into slightly different directions. The slit between the first crystal and the sample is used to select a single wavelength (i.e.,  $K\alpha_1$ ). This slit is also used to limit the lateral extent of the beam size, for an analysis of a small area on the sample surface.

A nonuniform depth distribution of strain in the sample will give rise to a distributed diffraction pattern. An example of the rocking curve data taken from a virgin crystal and an ion bombarded crystal is given in Figure 15. In a symmetric Bragg reflection, the strain  $\epsilon$  causes the Bragg angle shift by  $-\epsilon \tan \theta_B$  radians from the original Bragg angle,  $\theta_B$ , which is at the zero angle in the figure.

The lattice damage by the ion irradiation causes a decrease in the structure factor and the diffuse x-ray scattering. A simple way to take this into account is to assume a random Gaussian distribution for the atomic displacements. That is,

$$g(\vec{r}_i') = \frac{1}{\sqrt{2\pi a^2}} e^{-\frac{(\vec{r}_i' - \vec{r}_i)^2}{2a^2}}$$

where  $\vec{r}_i'$  is the actual atomic position,  $\vec{r}_i$  is the ideal lattice position, and  $a$  is the root mean square atomic displacement. The structure factor is to be averaged over this distribution. The structure factor,  $F_H$ , is thus expressed as

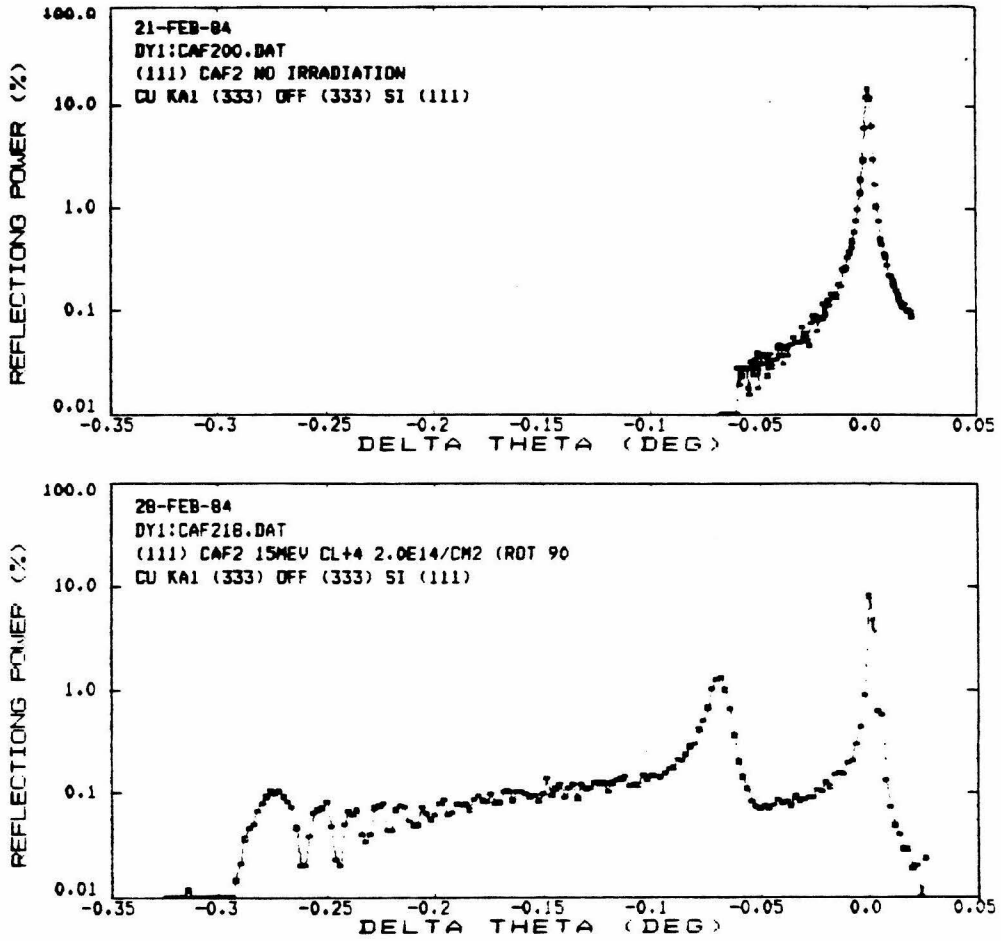


Figure 15. Example of experimental rocking curve from a virgin crystal and an MeV ion-bombarded crystal. Here, the sample crystal is  $\text{CaF}_2(111)$  with  $\text{CuK}\alpha_1$  radiation.



$$F_H = F_H^0 e^{-\frac{8\pi^2 \sin^2 \theta_B}{\lambda^2} u^2}$$

where the subscript H represents the Miller indices of the reflecting lattice plane, and  $F_H^0$  is the structure factor of an undamaged crystal.

If one knows the total thickness of strained layers, one can obtain the depth distribution for strain and for average atomic displacements. This is obtained by fitting the experimental rocking curve with the calculated rocking curve using a suitable x-ray diffraction theory. When the maximum reflecting power from the surface strained layer is less than 6 %, a kinematical x-ray diffraction theory can be used. This has been used for the samples implanted with ions of energy  $\leq 200$  keV (Sp81).

When the reflecting power of the surface strained layer is above 6 %, a more general dynamical x-ray diffraction theory should be used. We applied this theory for the analysis of the rocking curves taken from the MeV ion-bombarded crystals, and this is discussed in the next section.

## 2.2 Dynamical Diffraction Theory and Rocking Curve Analysis

The general theory of x-ray diffraction, which properly accounts for normal absorption (photoelectric process and Compton scattering) and extinction (coherent scattering or diffraction) of wave fields in a crystal medium, is called the dynamical x-ray diffraction theory. It is a first-order theory in that it takes the deviation of the x-ray refractive index from unity up to first order, and the variation of the complex amplitudes over one x-ray wavelength to the first order. When the homogeneity of the crystal specimen varies in only one direction, i.e., in depth with no lateral variation, the change in the x-ray complex amplitudes in depth is well described by the Takagi-Taupin equation which was originally developed by S. Takagi in 1962 (Ta62) and independently by D. Taupin in 1964 (Ta64). The derivation of the Takagi-Taupin equation is given in Appendix A.

The Takagi-Taupin equation is

$$i \frac{\lambda}{\pi} \vec{\beta}_0 \cdot \vec{\nabla} \vec{D}_0(\vec{r}) = \Psi_0 \vec{D}_0(\vec{r}) + \Psi_H \vec{D}_H(\vec{r}) , \quad (2.1)$$

$$i \frac{\lambda}{\pi} \vec{\beta}_H \cdot \vec{\nabla} \vec{D}_H(\vec{r}) = \Psi_0 \vec{D}_H(\vec{r}) + \Psi_H \vec{D}_0(\vec{r}) - \alpha_H \vec{D}_H(\vec{r}) ,$$

where

$\vec{D}_{0,H}(\vec{r})$  = complex amplitudes of the incident and diffracted waves,

$\vec{\beta}_{0,H}$  = wave vectors of the incident and diffracted waves,

$$\Psi_{0,H} = - \frac{e^2}{mc^2} \frac{\lambda^2}{\pi} \frac{F_{0,H}}{V} ,$$

$F_{0,H}$  = structure factors for the incident and diffracted waves,

$V =$  unit cell volume,

$$\alpha_H \approx -2(\theta - \theta_B)\sin 2\theta_B.$$

The above equation expresses the spatial variation of the complex amplitudes of the incident and diffracted waves along the incident and the diffracted directions, respectively. The Takagi-Taupin equation has been used in the study of diffraction from curved crystals by Klar and Rustichelli (Kl73). They have presented the theory in a form useful for the present study, writing the depth-dependent scattering amplitude in the following form.

$$i \frac{dX}{dA} = (1+ik)X^2 - 2(y+ig)X + (1+ik) , \quad (2.2)$$

where

$$X = \frac{D_H(\vec{r})}{\sqrt{b}D_0(\vec{r})} = \text{scattering amplitude, } b = \left| \frac{\gamma_0}{\gamma_H} \right|,$$

$\gamma_{0,H}$  = direction cosines of the incident and diffracted waves with respect to the inward surface-normal.

$$A = \frac{\pi |\Psi'_H|}{\lambda \sqrt{|\gamma_0 \gamma_H|}} z, \quad \Psi_{0,H} = \Psi'_{0,H} + i\Psi''_{0,H}, \quad z = \text{depth,}$$

$$g = \frac{(1+b)\Psi''_0}{2|\Psi'_H|\sqrt{b}} = \text{absorption, } k = \frac{\Psi''_H}{\Psi'_H},$$

$$y = \frac{(1+b)\Psi'_0 - b\alpha_H}{2|\Psi'_H|\sqrt{b}} = \text{deviation from the Bragg angle.}$$

The damage reduces the structure factor to  $F_H$ .

$$F_H = F_H^0 \exp\left(-\frac{8\pi^2 \sin^2 \theta_B}{\lambda^2} u^2\right) , \quad (2.3)$$

where

$F_H^0$  = structure factor for the undamaged crystal,

$u$  = average atomic displacement.

The strain is taken into account through  $\alpha_H$ .

$$\alpha_H = -2(\theta - \theta_B)\sin 2\theta_B - (c_1\varepsilon_1 + c_2\varepsilon_2) , \quad (2.4)$$

where

$$c_1 = \cos^2\varphi \tan\theta_B \pm \sin\varphi \cos\varphi ,$$

$$c_2 = \sin^2\varphi \tan\theta_B \mp \sin\varphi \cos\varphi ,$$

upper sign = for the incident angle of  $\theta_B - \varphi$  w.r.t. the sample surface,

lower sign = for the incident angle of  $\theta_B + \varphi$  w.r.t. the sample surface,

$\varphi$  = angle between the surface and the reflecting lattice plane,

$\varepsilon_1$  = strain perpendicular to the surface,

$\varepsilon_2$  = strain parallel to the surface.

Larson and Barhorst have used equation (2.2) to obtain the strain depth distribution in an implanted and laser annealed silicon crystal (La80a). They decomposed the complex differential equation (2.2) into two coupled real equations by putting  $X = X_1 + iX_2$ , and integrated each equation numerically to obtain the rocking curve. We take, however, a different approach which takes less computational time.

Equation (2.2) can be integrated analytically (Ha84),

$$X(A) = \frac{sX_0 + i(B+CX_0)\tan[s(A-A_0)]}{s - i(C+BX_0)\tan[s(A-A_0)]} , \quad (2.5)$$

where

$$X(A_0) = X_0, B = -(1 + ik),$$

$$C = y + ig, s = \sqrt{C^2 - B^2},$$

$$|X(0)|^2 = \text{reflecting power of the sample.}$$

Thus, if one knows the scattering amplitude  $X$  at the bottom of a layer, then one can calculate  $X$  at the top of the layer using the formula (2.5). In this layer approximation, one uses (2.5) repetitively for the strained layers, starting with an initial condition which should be given at the interface of the undamaged substrate and the bottom strained layer. This initial condition is simply the solution for an infinitely thick crystal. The initial condition is obtained most easily by the following consideration.

Imagine a layer of thickness  $A_0$  on an infinitely thick crystal. The layer and substrate crystals are assumed to be identical with no damage or strain. Then the " $X_0$ " in (2.5) is the scattering amplitude of the substrate which is the infinite crystal solution, and " $X(0)$ " at the layer surface will again be the infinite crystal solution because there is no strain or damage in the layer. Thus, by putting  $X(A) = X_0$  in (2.5) and solving for  $X_0$ , we get the infinite crystal solution, which is

$$X_0 = \frac{-C \pm \sqrt{C^2 - B^2}}{B}. \quad (2.6a)$$

The lower sign in (2.6a) gives the correct infinite crystal solution. Thus, the initial condition is

$$X_0 = -\frac{B}{C - \sqrt{C^2 - B^2}}. \quad (2.6b)$$

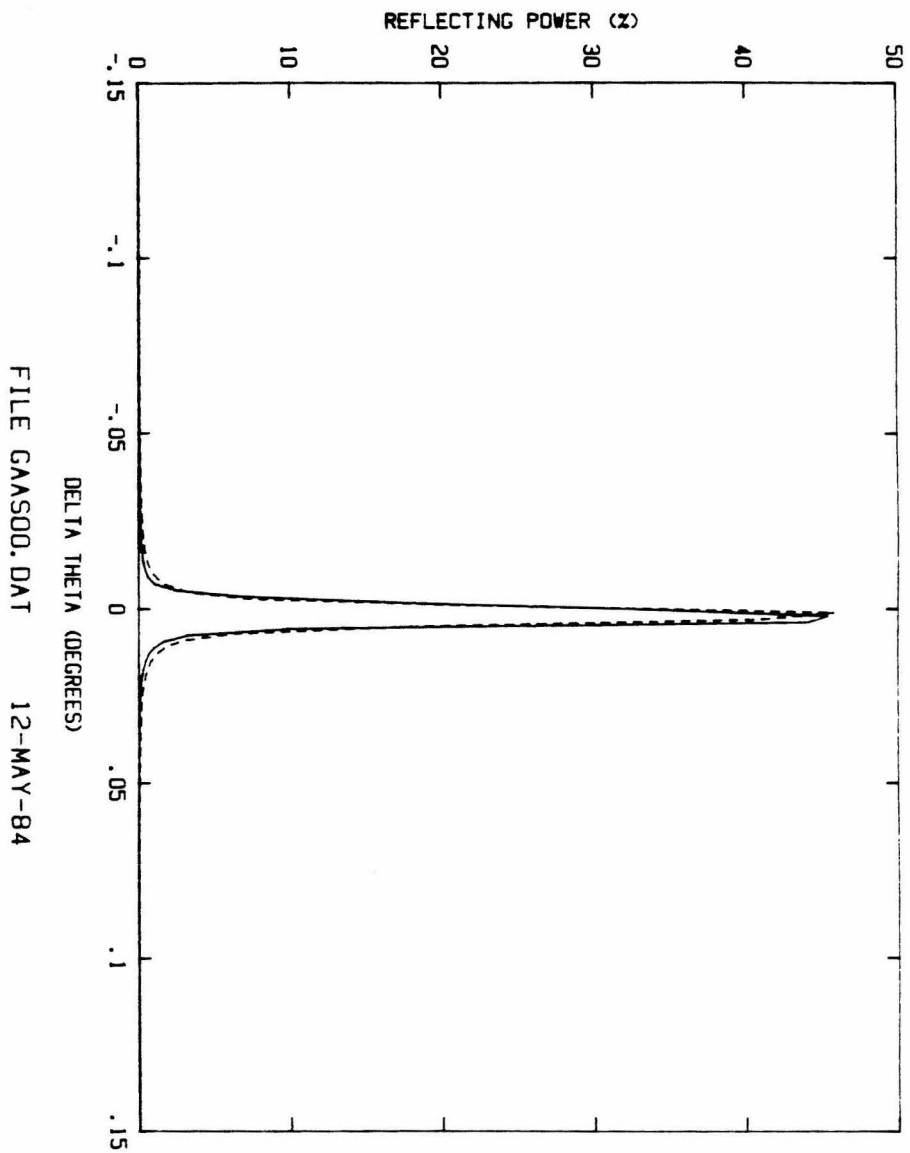


**Figure 16.** Dynamical diffraction theory calculation of rocking curve. Experimental (dashed) and calculated (solid) curves are shown for a FeK $\alpha$ 1 (400) reflection from a virgin GaAs(100) crystal. The formula (2.6b) was used for the calculation with 10 arcsec half-width gaussian convolution.

Equations (2.5) and (2.6b) are used for the rocking curve analysis with the dynamical x-ray diffraction theory. Since the correct evaluation of "s" (which is a square root of complex variables) is important for the rocking curve calculation, we give the formula in Appendix B.

As a final remark, we show a calculated rocking curve for a virgin crystal in Figure 16. The figure shows an experimental rocking curve (dashed) for a virgin GaAs(100) crystal with FeK $\alpha$ 1 (400) reflection, and the calculated rocking curve (solid) using the formula (2.6b) with a 10 arcsec half-width gaussian convolution.

### 3. Behavior of $\text{CaF}_2$ , $\text{LiNbO}_3$ , Si, and Cu Crystals

We studied the insulating materials,  $\text{CaF}_2$  and  $\text{LiNbO}_3$ , to find whether or not the ion damage track produced by the electronic process from the MeV ion bombardment controls the strain and damage production in the surface layers. The rocking curves taken from these materials are given in Figures 17 and 18. These materials had been bombarded with 15 MeV Cl ions to various beam doses. The strain and damage depth profile in the bombarded  $\text{CaF}_2$  crystals was obtained by analyzing the rocking curves of Figure 17. The depth profiles are given in figure 19 each with corresponding experimental and calculated rocking curve. The kinematical x-ray diffraction theory was used for the analysis because the maximum reflecting power from the strained layer was low (i.e., less than 6 %), and because a computer program based on this theory was available (the dynamical theory was subsequently programmed).

The correspondence between the rocking curve and the depth profile in Figure 19 is understood by the following way: (1) The peak at zero angle is from the undamaged substrate beyond the ion range (depth  $\geq 5 \mu\text{m}$ ). (2) The prominent peak at negative angle corresponds to the relatively thick layer of low strain, near the surface. (3) The peak at the lowest angle is from the layers of high strain at around  $4 \mu\text{m}$  depth.

According to the depth profile in the bombarded  $\text{CaF}_2$  crystal shown in Figure 19, the production of strain and damage in this insulating material seems to be controlled by the nuclear collision process of the ion (see Figure 13 for the stopping power depth profile). This indicates that even if electronic erosion occurs in this insulating material, point defects are produced mainly by the nuclear stopping.



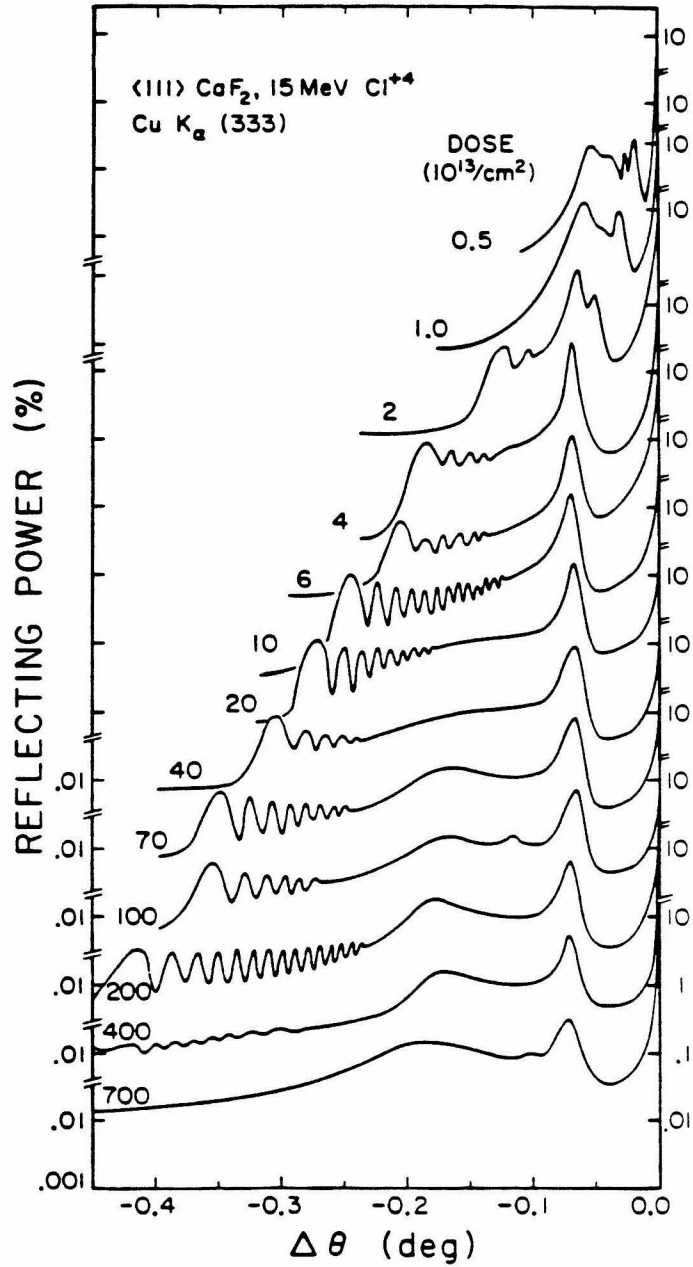


**Figure 17.**  $\text{CuK}\alpha_1$  (333) reflection from 15 MeV Cl ion-bombarded  $\text{CaF}_2(111)$  crystals. Only the negative angle side of the virgin crystal Bragg angle is shown.

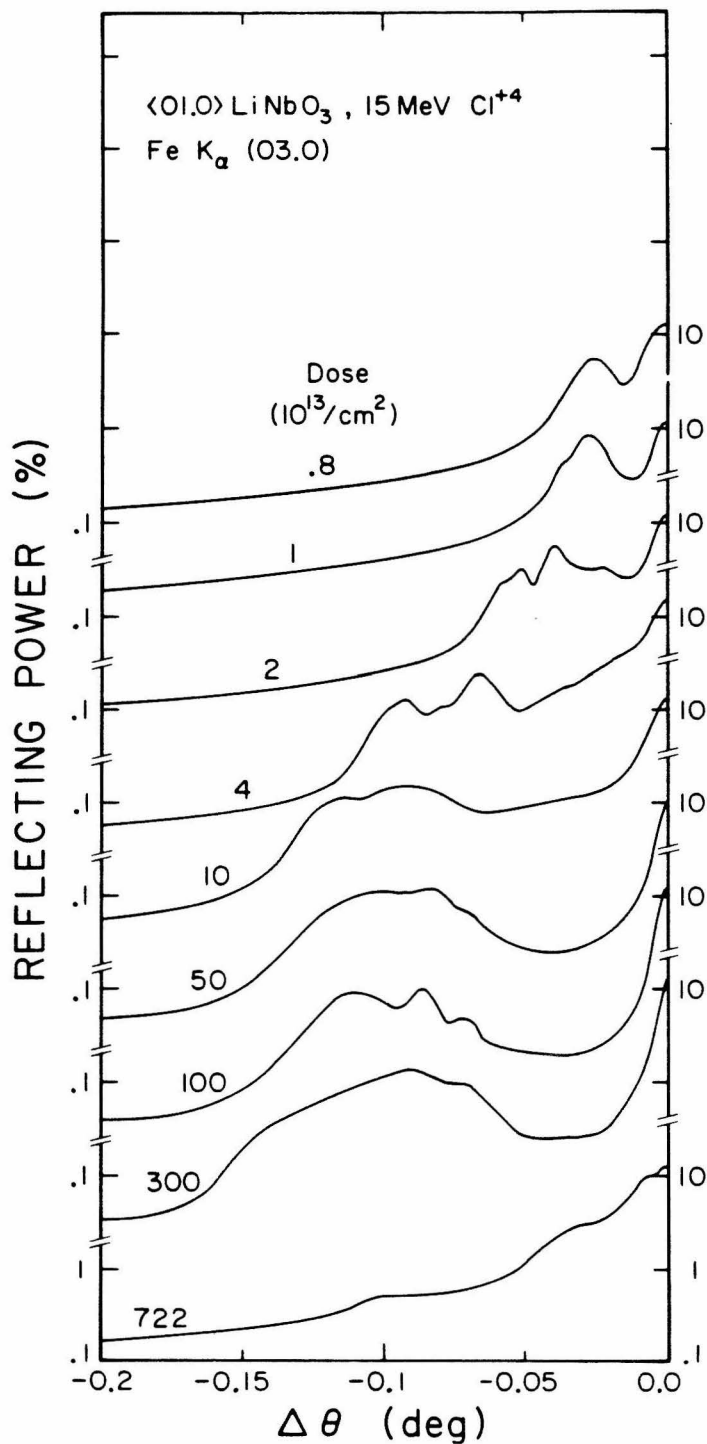


**Figure 18.** Experimental rocking curves for MeV ion-bombarded  $\text{LiNbO}_3(01.0)$  crystals.  $\text{FeK}\alpha 1$  radiation was reflected from (03.0) planes. The virgin crystal Bragg angle is at zero degree in the figure.

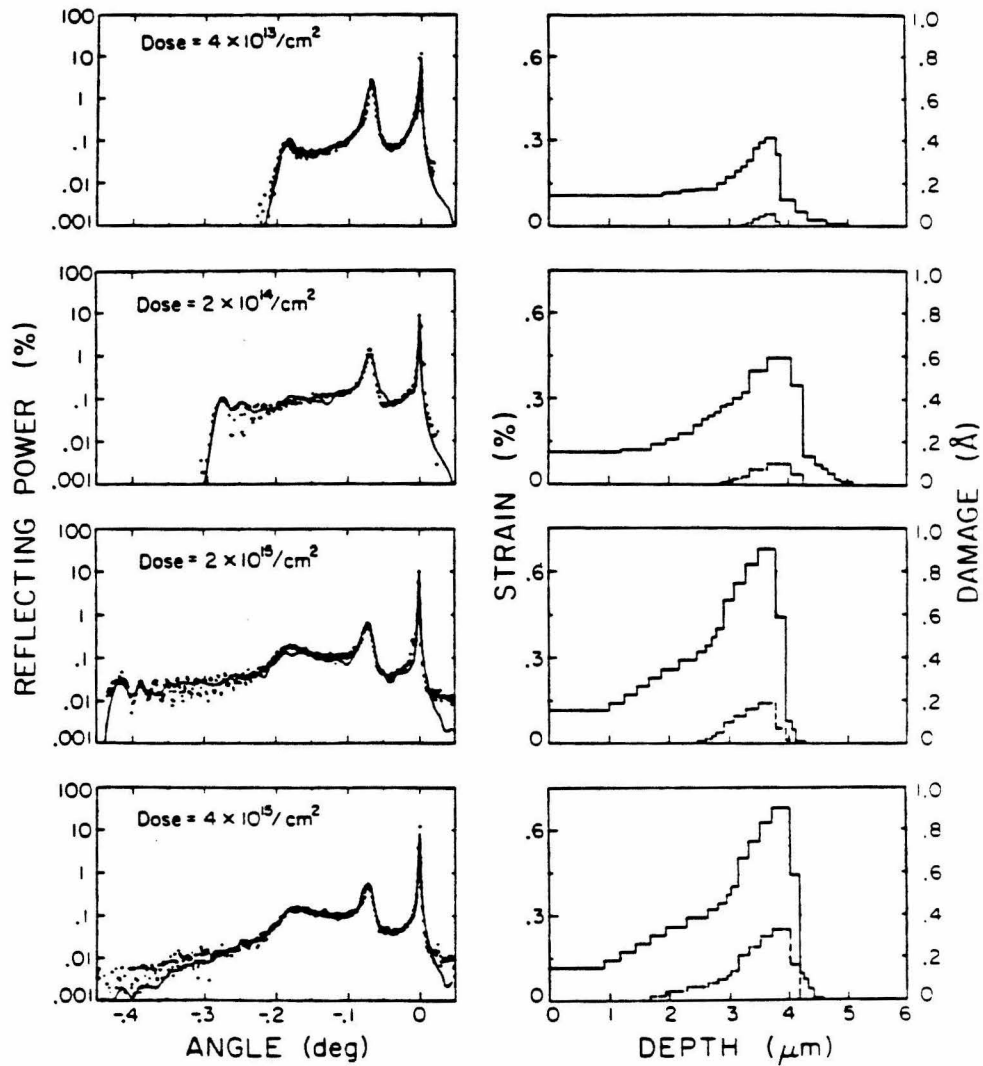


**Figure 19.** Kinematical diffraction theory analyses of  $\text{CaF}_2$  rocking curves shown in Figure 17. Left: calculated (solid) and experimental (dotted) rocking curves. Right: strain (solid) and lattice displacement (dashed) depth profile.

The rocking curves of the bombarded  $\text{LiNbO}_3$  crystal indicate that the surface layers of this material have become amorphous after an ion beam dose of  $7.22 \times 10^{15}$  ions/cm<sup>2</sup> (the diffraction from the strained layer is very weak for  $u \geq 0.2$  Angstrom). The  $\text{CaF}_2$  crystal did not completely become amorphous in the surface layer after  $4 \times 10^{15}$  ions/cm<sup>2</sup>. However, the rocking curves indicate that the region corresponding to the maximum nuclear stopping power has become amorphous at this dose, and this is responsible for the disappearance of the rapidly oscillating part in the rocking curve. The layer which has become amorphous in the  $\text{CaF}_2$  crystal corresponds to an average atomic displacement larger than .2 Angstrom in the strain/damage depth distribution (see the last profile of Figure 19).

Maximum strains reached at a given beam dose, corresponding to the maximum angular deviation in the rocking curves, and main surface strain, corresponding to the maximum intensity, are shown in Figure 20 for the  $\text{CaF}_2$  and  $\text{LiNbO}_3$  crystals. The slope change in the strain versus beam dose curve, at a beam dose of  $4 \times 10^{13}$  ions/cm<sup>2</sup>, and the observation that the increase in the reflecting power for the main strain peak with beam dose stopped at the same dose, made it possible to infer an approximate cylindrical damage track diameter for the Cl ion in  $\text{CaF}_2$ , which is about 18 Angstroms (Wi84b).

The behavior of a Si crystal under the MeV ion bombardment is shown in Figure 21. Data indicate that the region around the maximum nuclear stopping power becomes amorphous at a relatively low beam dose,  $1.25 \times 10^{14}$  ions/cm<sup>2</sup>, and the maximum strain reached before it becomes amorphous is very low (about .06 %) compared to the insulating crystals. The rocking curve at negative angles for doses higher than  $1.25 \times 10^{14}$

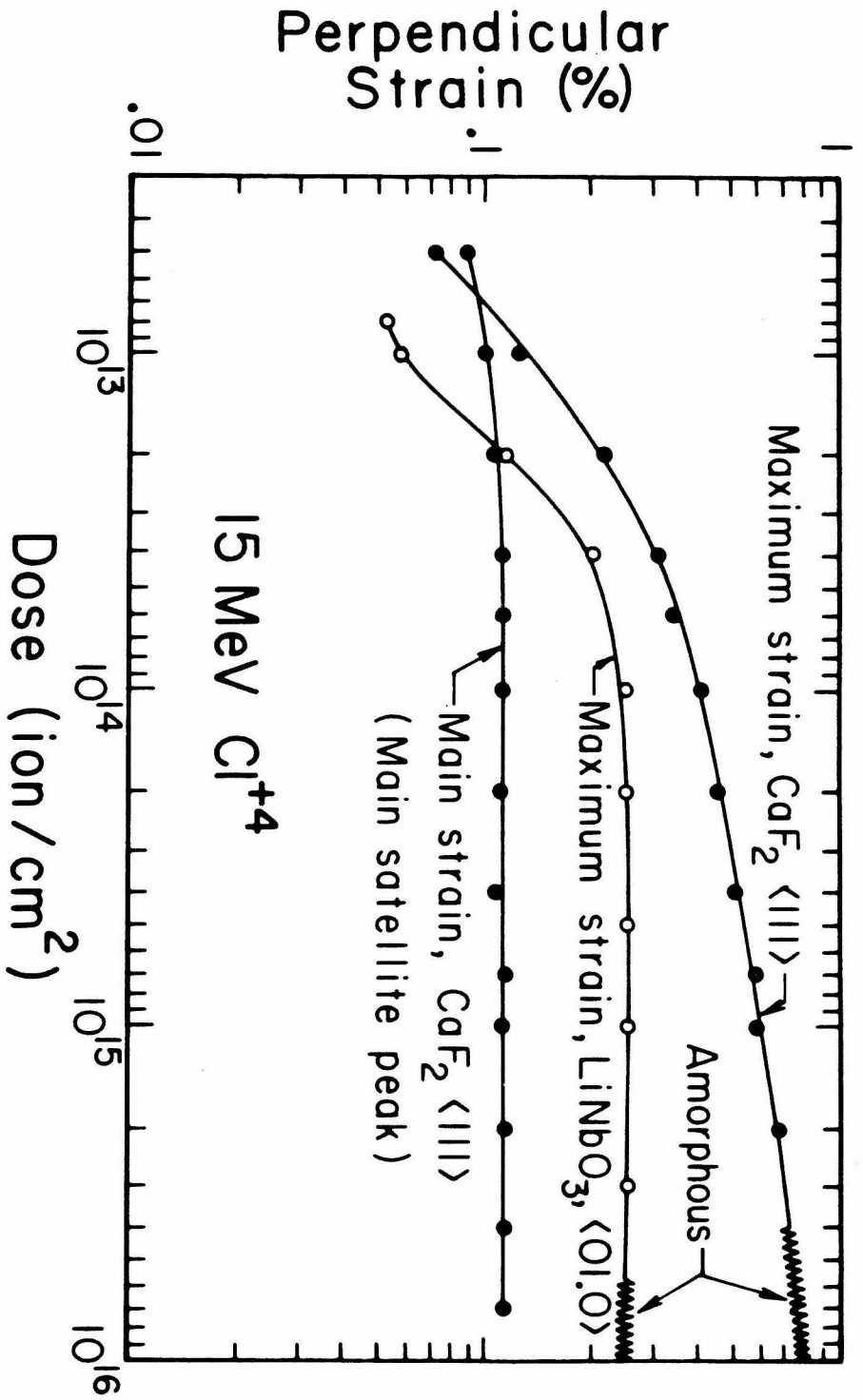


**Figure 20.** Maximum strain reached in the crystal is shown as a function of beam dose for CaF<sub>2</sub> and LiNbO<sub>3</sub> crystals. The main strain in the surface layer of CaF<sub>2</sub>, corresponding to the maximum satellite peak, is also shown.

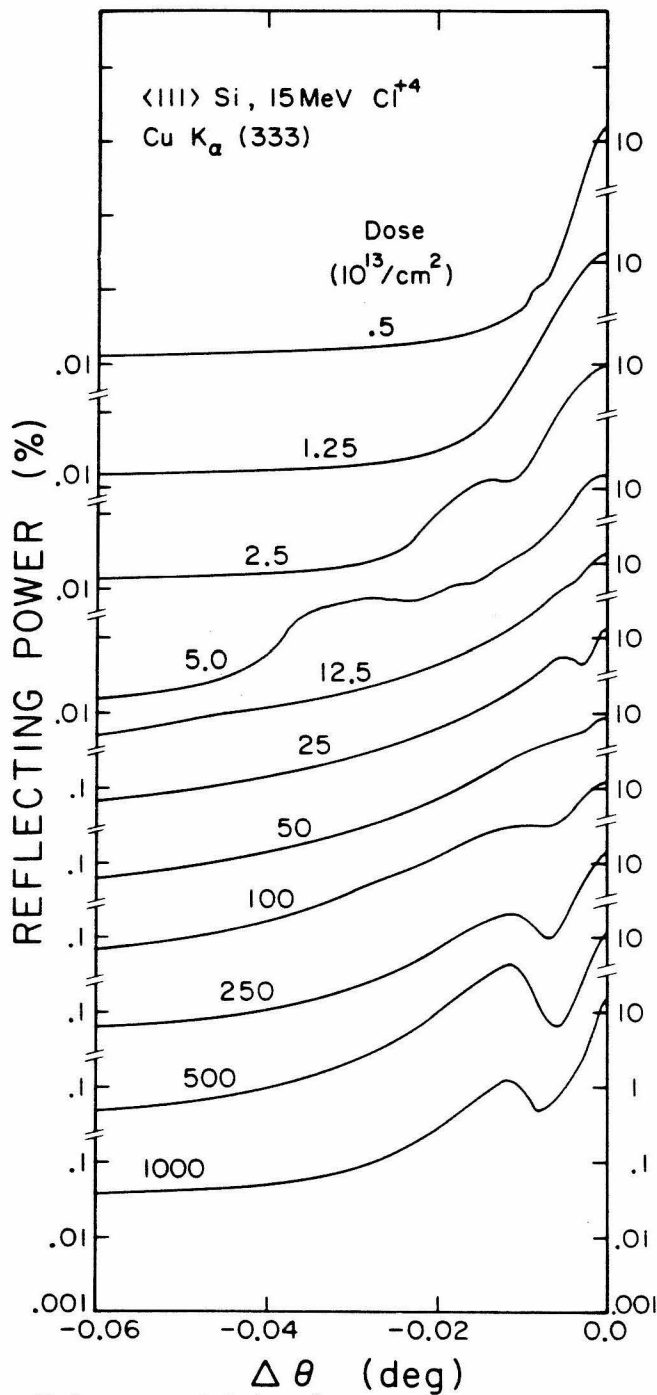


**Figure 21.** Behavior of Si(111) crystal under MeV ion irradiation at room temperature. Note that deviation of the strain peak from the original Bragg angle (at zero degree in the figure) is much smaller than in  $\text{CaF}_2$  or  $\text{LiNbO}_3$ .

ions/cm<sup>2</sup> may be attributed to defect complexes or to the strain fields around disordered regions, and the corresponding strain in the rocking curve is about 0.02 %.

Primary defects in Si or Ge crystals are all known to be mobile at room temperature. Thus, most of the defects produced in the surface layers by MeV ion bombardment at room temperature may have been annihilated. This may be responsible for the rocking curve pattern in the Si crystals which generally show very low strain, with most of the surface layer free of damage except the region around the end of the ion range.

The strain produced in the MeV ion bombarded Cu crystal was negative at a beam dose of  $2 \times 10^{13}$  ions/cm<sup>2</sup> (see Figure 22). No strain could be seen at a high dose ( $1.2 \times 10^{15}$  ions/cm<sup>2</sup>) as shown in Figure 22. Negative strain produced in an ion-implanted InP crystal was also observed (Vr85). The origin of negative strain in ion-irradiated crystals is not understood.

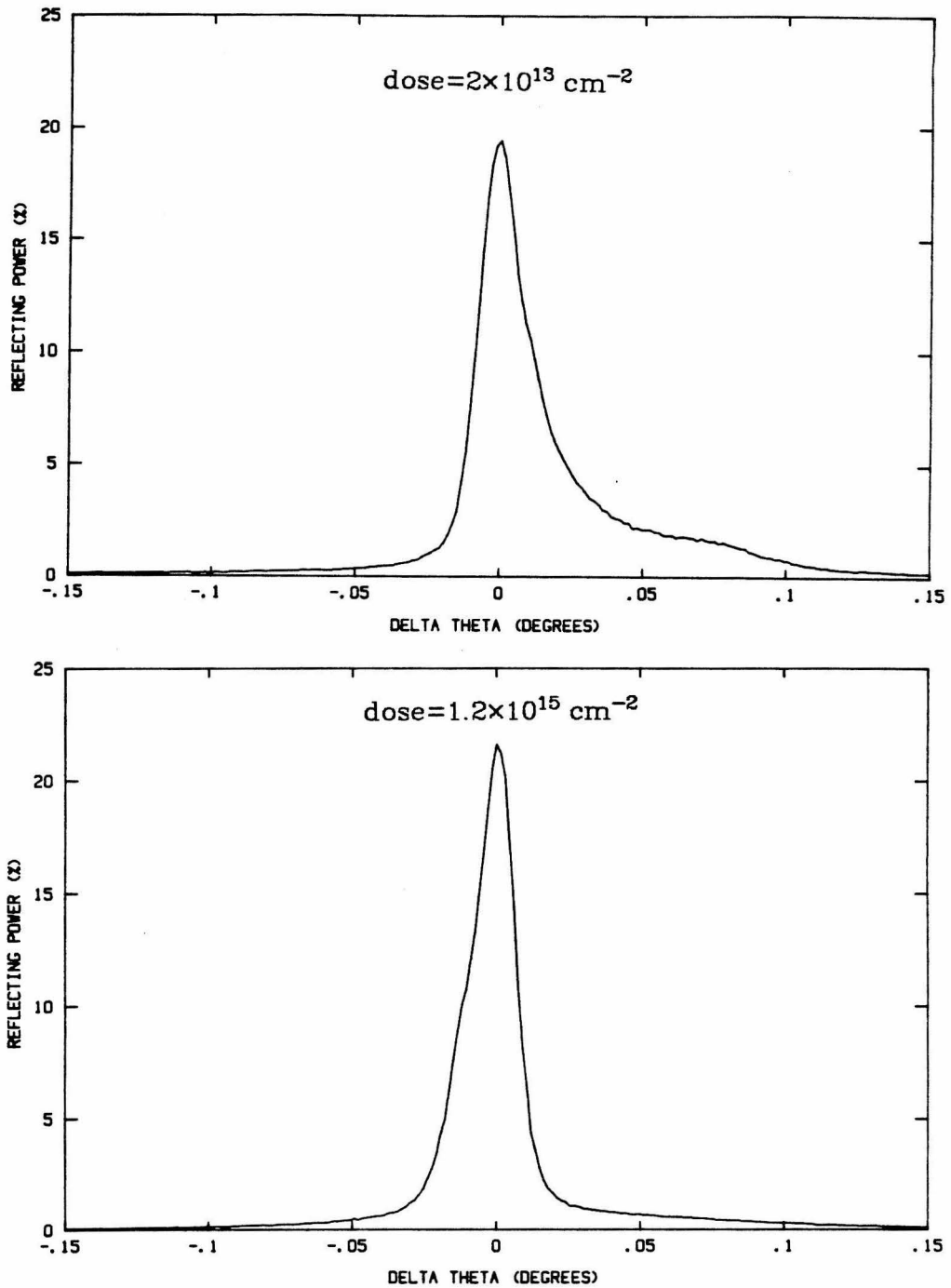


**Figure 22.** Cu(111) crystal bombarded to  $2 \times 10^{13}$  and  $1.2 \times 10^{15} \text{ cm}^{-2}$  with a 15 MeV Cl ion beam. The negative strain developed at  $2 \times 10^{13} \text{ cm}^{-2}$  disappears at  $1.2 \times 10^{15} \text{ cm}^{-2}$ , indicating that the corresponding region has become amorphous.  $\text{CuK}\alpha_1$  radiation was reflected from the (333) planes.



## 4. GaAs and III-V Semiconductors

### 4.1 Lattice Disorder and Recovery Stages in III-V's

III-V compounds have either the zinc-blende structure or the wurtzite structure (Ki76). We consider the variety of basic lattice defects in the zinc-blende structure. For example, in GaAs there can be both Ga-vacancies and As-vacancies. There can be Ga-interstitials surrounded by nearest neighbors which are all Ga- or all As-atoms, and similarly for As-interstitials. Thus in the zinc-blende lattice we may have two kinds of vacancies and four kinds of interstitials. There can also be clusters of interstitials and/or vacancies.

In addition, there can be two distinguishable sites for the two kinds of interstitial atoms. Both sites are equivalent as far as nearest neighbors are concerned (see Figure 23). The interstitial sites are at the center of a trigonal prism with six neighbors at the corners of the prism. The sites differ in that in one the prism is "capped" by the next nearest neighbors along the c-axis from the interstitial sites. The other site is in the center of an "uncapped" prism; i.e., the next nearest neighbors to this interstitial site are the atoms capping adjacent prisms (Co66).

Another type of lattice defects in the zinc-blende structure is the antisite defects where a Group III atom occupies a Group V site, or vice versa. It has been suggested that diffusion in III-V compounds proceeds through a specific sublattice (Ei57, Go61). That is, Ga atoms diffuse through the Ga sublattice of GaAs, etc.

Irradiation with heavy particles can result in high atomic recoil energies and spike damage such that a local region of the lattice undergoes a phase change. In the MeV ion irradiated materials, the spike damage can

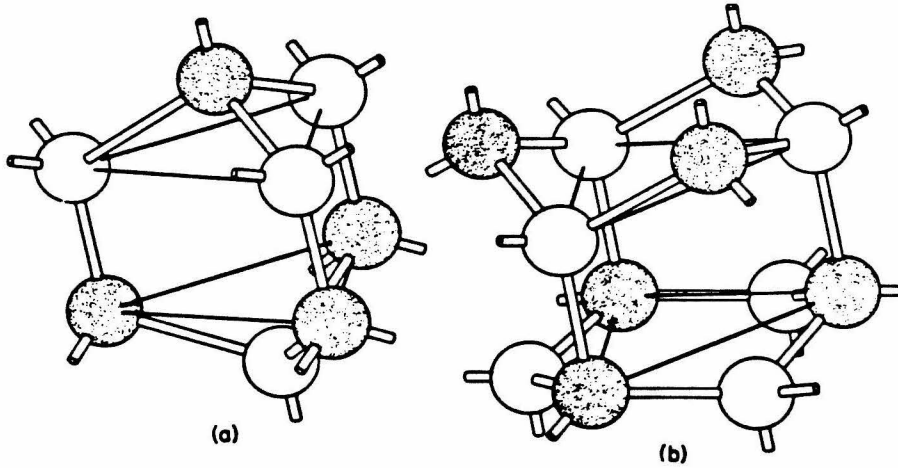


**Figure 23.** Interstitial environment in the zinc-blende lattice. (a) The "capped" prism. (b) The "uncapped" prism. This was taken from Corbett (Co 66).

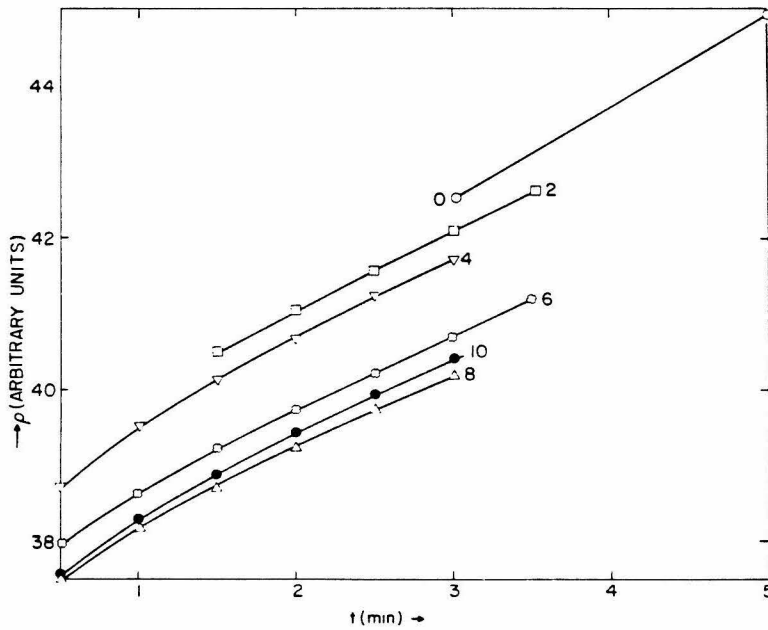


**Figure 24.** Resistivity at 4.2 K in n-type GaAs as a function of time after irradiation with 1.0 MeV electrons (dose  $8 \times 10^{14}$  electrons  $\text{cm}^{-2}$ ) and various doses of 0.46 MeV electrons. The low-energy electron doses are indicated at the curves in units of  $10^{13}$  electrons  $\text{cm}^{-2}$ . This was taken from Thommen (Th 70).

easily occur around the end of the ion range where the nuclear stopping power is high. Also, there is always the possibility that sparse spike damage regions occur in the near surface region even if the nuclear stopping power is on the order of the threshold displacement energy per atomic spacing. Experimental data for GaAs indicate that the lattice defects are produced by the nuclear stopping process and are partially recovered by the electronic process.

Available experimental data also indicate that ionizing radiation plays a role in the defect-related processes with different efficiencies for the III-V semiconductors and for the elemental semiconductors (Si and Ge). For example, Thommen measured the electrical resistivity in GaAs after 1 MeV electron irradiation followed by 0.46 MeV electron irradiation, both at 4.2 K (see Figure 24). Here, 1 MeV is above the threshold energy for the production of displacement damage by electrons in GaAs, while 0.46 MeV is below the threshold so that electrons of this energy produce only electronic excitation in the target. A significant reduction of resistivity was observed, after 0.46 MeV electron irradiation for the beam dose range  $10^{13}$ - $10^{14}$  electrons/cm<sup>2</sup>, from that taken before 0.46 MeV irradiation (Th70). However, a similar experiment performed on Ge (see Figure 25) shows that the lower energy electron beam dose required to bring the radiation annealing to completion is about 3 orders of magnitude higher than in GaAs (Mc59, Si69).

Different types of defects have different associated activation energies. If the experimental probe is sensitive to certain types of defects, then the measured physical quantity changes rather abruptly whenever the annealing temperature matches with the activation energies. For example, in electrical resistivity measurements or in optical

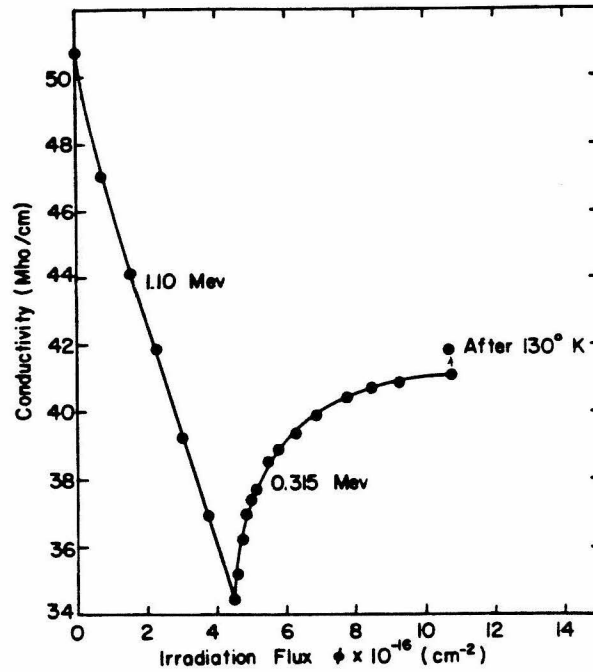


Figure 25. Conductivity changes in n-type Ge with 1.10 MeV electron followed by 0.315 MeV electron irradiation. This was taken from McKay et al. (Mc 59).

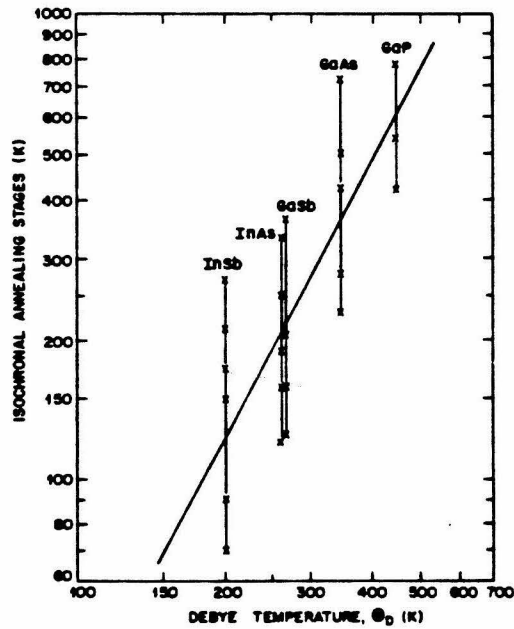


Figure 26. Isochronal recovery stages in InSb, InAs, GaSb, GaAs, and GaP as a function of Debye temperature  $\Theta_D$ . The line through the data shows a  $\Theta_D^2$  dependence. This was taken from Lang et al. (La 77).

measurements the annealing data usually show major recovery stages for each type of defects (see , for example, Ei71).

The isochronal recovery stages for some of the III-V semiconductors are shown in Figure 23. This was drawn based upon previously reported annealing data on the electrical or optical measurements of these materials (La77, Pi66). The line drawn through the data is proportional to  $\Theta_D^2$ , where  $\Theta_D$  is Debye temperature. Note that all the defects in GaP are all stable well above room temperature, while the annealing of lower stage defects in GaAs occur near or below room temperature.

It has been suggested that divacancies, interstitials, and close Frenkel pairs are possible candidates for defect annealing at lower temperatures (Pi73). It is also believed that the radiation-induced defects which are stable at room temperature in GaAs are most likely simple defects such as antisite defects, vacancies, or interstitials (La77).

Strain induced by radiation damage in crystalline materials, however, could be produced by all kinds of defects, so that the annealing data on the lattice dilatation may indicate a spectrum of activation energies (Pr55). The data obtained on the strain reduction in GaAs due to annealing indicate a spectrum of activation energies.

## 4.2 Experimental Results and Discussion<sup>3</sup>

### 4.2.1 GaAs

GaAs(100) single crystals with dopants Cr, Te, or Si, were bombarded with Cl, O, and C ions of various energies to beam doses ranging from  $1 \times 10^{13}$  to  $5 \times 10^{15}$  ions/cm<sup>2</sup>, and all the bombardments were made at room temperature. Rocking curves taken with FeK $\alpha$ 1 radiation are shown in Figure 27 for a symmetric reflection from (400) planes. The development of a single peak after an ion beam dose,  $1.2 \times 10^{15}$  cm<sup>-2</sup> for the 15 MeV Cl ions, indicates the saturation of perpendicular strain to about 0.4 %. Among the crystals with different dopants, the Cr-compensation-doped GaAs had the best crystal quality as demonstrated by the rocking curve before the ion bombardment. We think this is due to the doping concentration in the crystal, and the Cr-doped semi-insulating GaAs requires the lowest doping concentration to achieve the required electronic property. The strain development and saturation phenomenon was the same for other crystals with different dopants, and this is illustrated for the Te-doped GaAs crystal in the last diagram of Figure 27. Also, this phenomenon was observed for all the ions of different energies we tried.

Using asymmetric reflections we measured the parallel strain in the surface layers. If a crystal contains point defects which are uniformly distributed throughout the entire volume, then the crystal would expand isotropically. However, since the radiation-damaged region in our samples was constrained laterally by the ion beam spot size, and limited in depth by the ion range, we expected that the parallel strain would be

---

<sup>3</sup>Part of the work on GaAs has been published (Wi84).

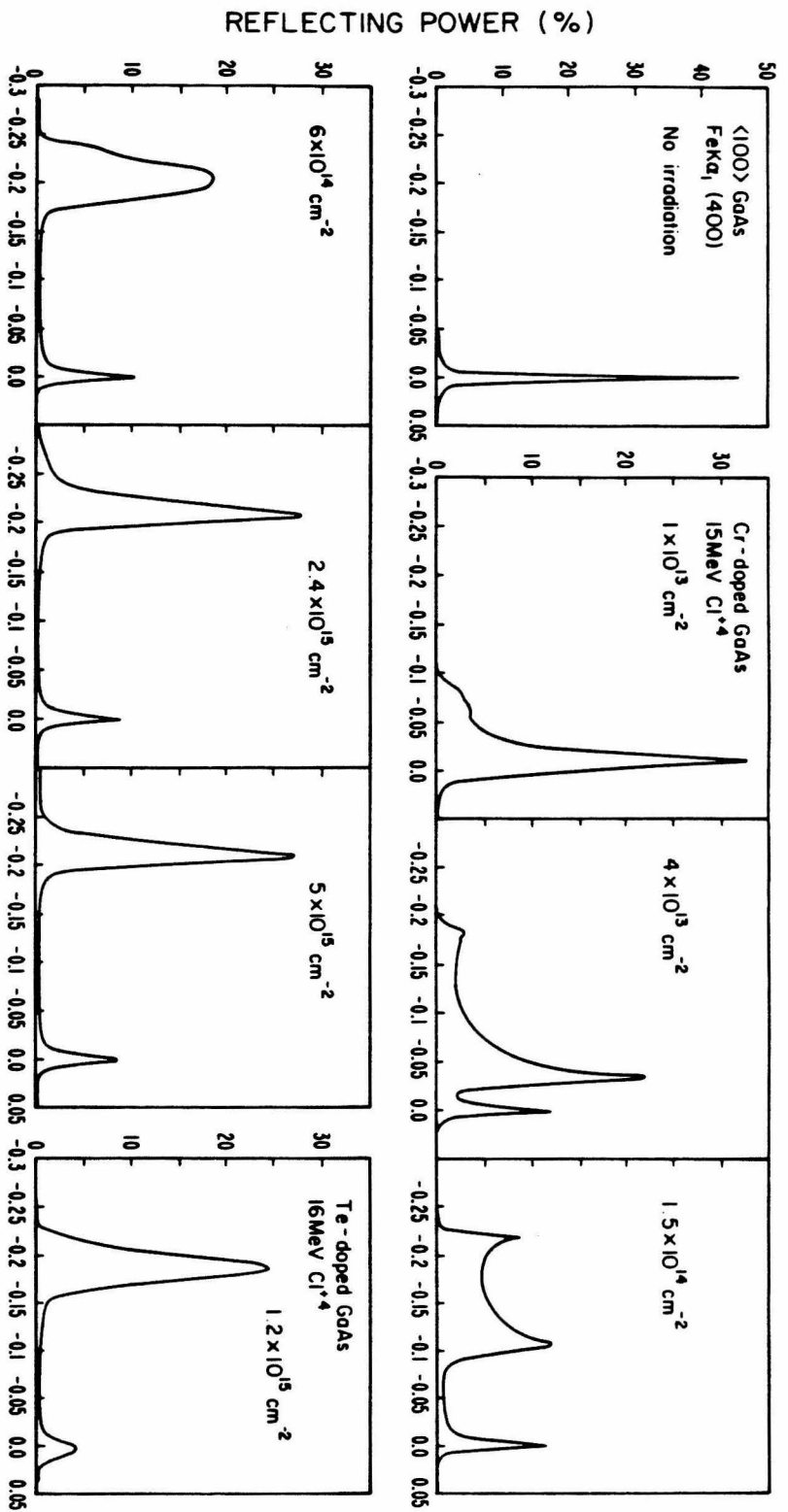


**Figure 27.** FeK $\alpha$ 1 (400) reflections from 15 MeV Cl ion bombarded GaAs(100) crystals. Ion doses are shown in the figure. Development of a single diffraction peak at negative angles indicates strain saturation. The small peak at zero angle is from the undamaged substrate crystal beyond the ion range.

different from the perpendicular strain (see Figure 28 for beam spot geometry). By the asymmetric reflections from (333), (511), and (422) planes we measured the rocking curves for the Cr-doped GaAs(100) bombarded with 15 MeV Cl and 8.3 MeV O ions to the beam doses of  $1.2 \times 10^{15}$  and  $2.4 \times 10^{15}$  ions/cm<sup>2</sup>, respectively. Both beam doses are such that the diffraction from the surface layers is of a single peak structure so that the strains can be obtained from the rocking curves directly.

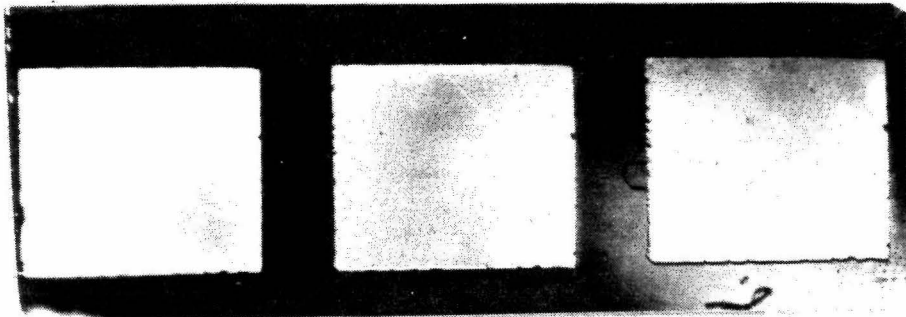
Table VI summarizes the asymmetric measurements. In Table VI(a), we give the appropriate parameters and the angular separation of the strain peak from the substrate peak for each reflection. Table VI(b) shows that the parallel strain in the surface layers is essentially zero within the experimental error. Since the bombarded region was constrained by two factors, i.e., by the beam spot size and by the coupling of the strained film to the undamaged substrate, we tried to remove the constraint from the beam spot size by covering the whole sample surface (only in the x-direction) with the ion beam. The data obtained for the 15 MeV Cl beam were from this geometry, as is indicated in the footnote of Table VI(a). Since there was no observable difference in the angular separation from that with a laterally constrained beam spot, we concluded that the lateral expansion of the strained film is forbidden by a strong coupling of the  $\sim 6$   $\mu\text{m}$  thick surface layer to the much thicker substrate.

Symmetric (400) reflections were taken for a series of bombardments made at room temperature with Cl, O, and C ions of various energies. The perpendicular strain at the sample surface was measured from the rocking curves. The perpendicular strain at the surface (defined as surface strain hereafter) is shown in Figure 29 as a function of an ion beam dose for all the bombardments made. At the same dose the surface



## ION BEAM SPOT GEOMETRY

### (1) TOP-VIEW (X-RAY REFLECTION TOPOGRAPH)



X-RAY BEAM IS AT THE BRAGG ANGLE  
OF NON-BOMBARDED CRYSTAL



X-RAY BEAM IS AT THE SURFACE  
STRAINED LAYER BRAGG ANGLE

### (2) SIDE-VIEW

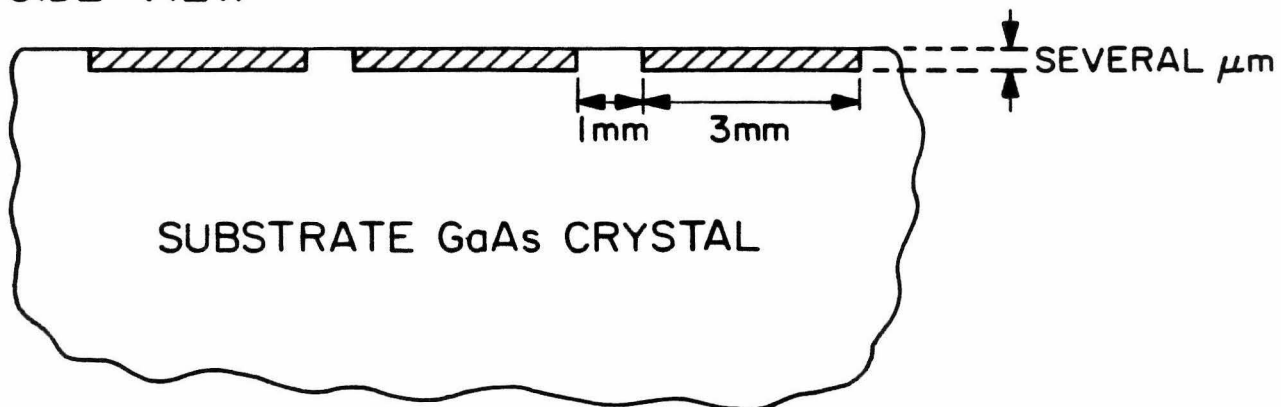


**Figure 28.** Ion beam spot geometry in samples. The spot size is around  $3 \times 3 \text{ mm}^2$  square.

**Table V.** Asymmetric reflection for the parallel strain measurements in GaAs(100) crystals.

**(a)** Angular separation of strain peak from substrate peak.


Reflection <i>FeK<math>\alpha</math>1</i>	(400)	(333)	(511)	(422)
$\theta_B$ (deg.)	43.27	63.16	63.16	57.27
$\varphi$ (deg.)	0	54.74	15.79	35.26
(1) $ \Delta\theta_B $ (deg.)	0.2001	0.2344	0.4469	0.3248
(2) $ \Delta\theta_B $ (deg.)	0.1888	0.2300	0.3746	0.2936


Incident angle =  $\theta_B - \varphi$  w.r.t. sample surface.

$|\Delta\theta_B| = k_1\varepsilon_1 + k_2\varepsilon_2$ , where  $\varepsilon_1$  = perpendicular strain,

$\varepsilon_2$  = parallel strain,  $k_1 = \cos^2\varphi \tan\theta_B + \sin\varphi \cos\varphi$ ,

$k_2 = \sin^2\varphi \tan\theta_B - \sin\varphi \cos\varphi$ .

(1). 15 MeV Cl<sup>+</sup>,  $1.2 \times 10^{15} \text{ cm}^{-2}$ , ion beam spot in sample = 

(2). 8.3 MeV O<sup>+</sup>,  $2.4 \times 10^{15} \text{ cm}^{-2}$ , ion beam spot in sample = 

**(b)** Comparison of angular separation and the perpendicular strain term.

	Reflection	(400)	(333)	(511)	(422)
15 MeV Cl $1.2 \times 10^{15} \text{ cm}^{-2}$	$ \Delta\theta_B $ (%)	0.349	0.409	0.780	0.567
	$k_1\varepsilon_1$ (%)	0.349	0.419	0.776	0.559
8.3 MeV O $2.4 \times 10^{15} \text{ cm}^{-2}$	$ \Delta\theta_B $ (%)	0.330	0.401	0.654	0.512
	$k_1\varepsilon_1$ (%)	0.330	0.396	0.732	0.528
(3)	$\frac{k_2}{k_1}$	0	0.75	0.055	0.032

(3).  $\frac{k_2}{k_1}$  is a measure of sensitivity of the angular separation to the parallel strain. When the incident angle is  $\theta_B + \varphi$ , it is more sensitive to the parallel strain.

strain is higher for the ions with higher nuclear stopping power (see the inset in Figure 29).

Since the defect density produced by the ion bombardment will be proportional to the nuclear stopping power, if the surface strain is plotted against the nuclear stopping power times beam dose, then the surface strain is higher for lower electronic stopping power (see Figure 30). Figure 30 indicates the role of the nuclear and electronic stopping powers in the strain/damage production. Now, we can make a model for the mechanism of strain/damage production by MeV ion bombardment.

The initial number of defects produced by the nuclear collision process must be proportional to the nuclear stopping power of the ion. Thus, we may write

$$N_0 = k_1 S_n, \quad (4.2.1)$$

where  $N_0$  is the initial number of defects per unit length,  $S_n$  the nuclear stopping power, and  $k_1$  is a constant.

These defects produced by the nuclear collision process are partially recovered by the electronic ionization process. The recovery rate is assumed to be proportional to the number of electron-hole pairs created by the ionization process. The initial number of electron-hole pairs per unit length,  $n_0$ , will be proportional to the electronic stopping power  $S_e$ ; i.e.,

$$n_0 = \frac{k_2 S_e}{E_g}, \quad (4.2.2)$$

where  $E_g$  is the bandgap, and  $k_2$  is a constant. The time variation due to electron-hole pair recombination is taken into account by writing

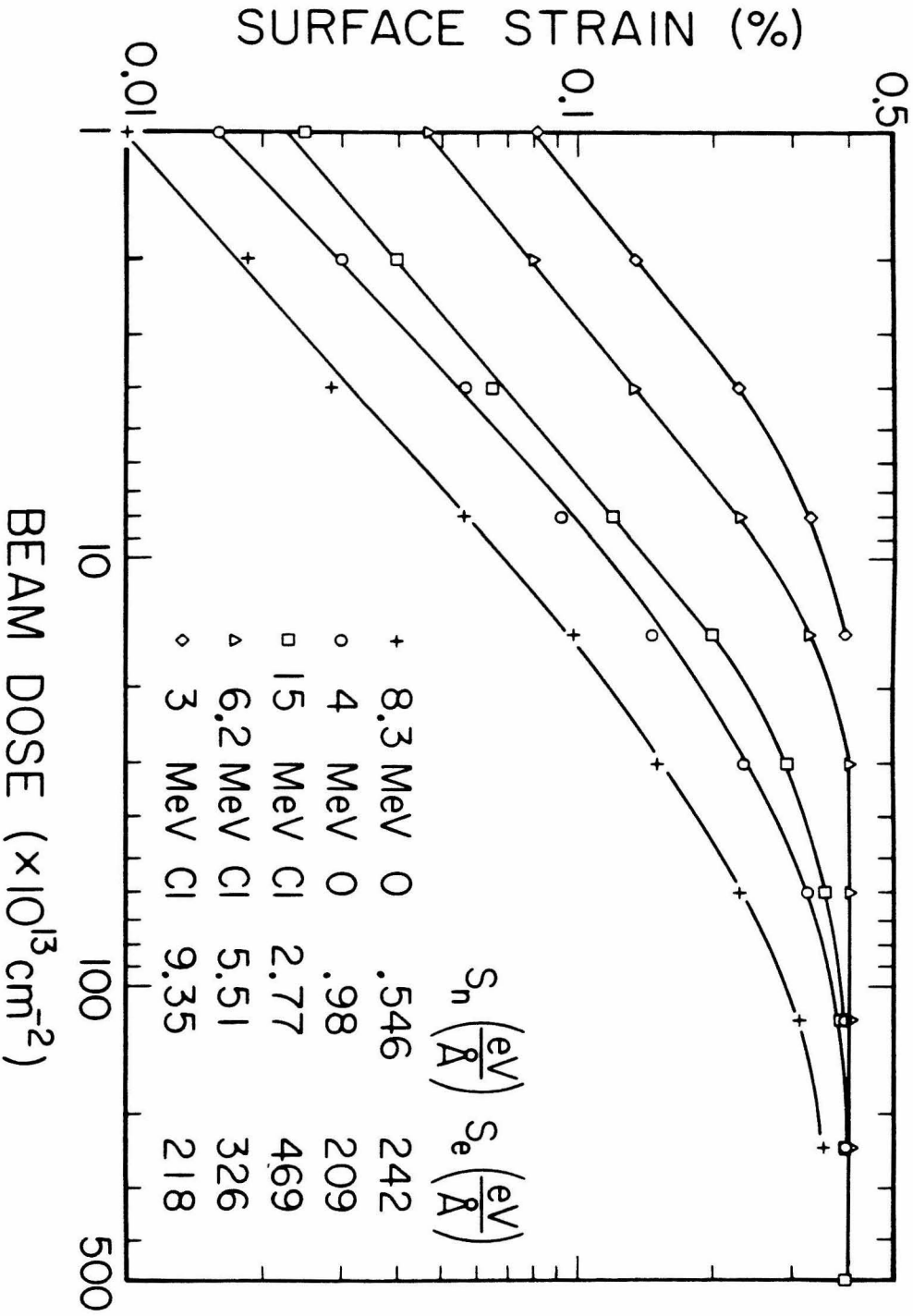


**Figure 29.** Perpendicular strain at GaAs(100) surface as a function of the bombarding beam dose. The higher the nuclear stopping power, the higher the strain.

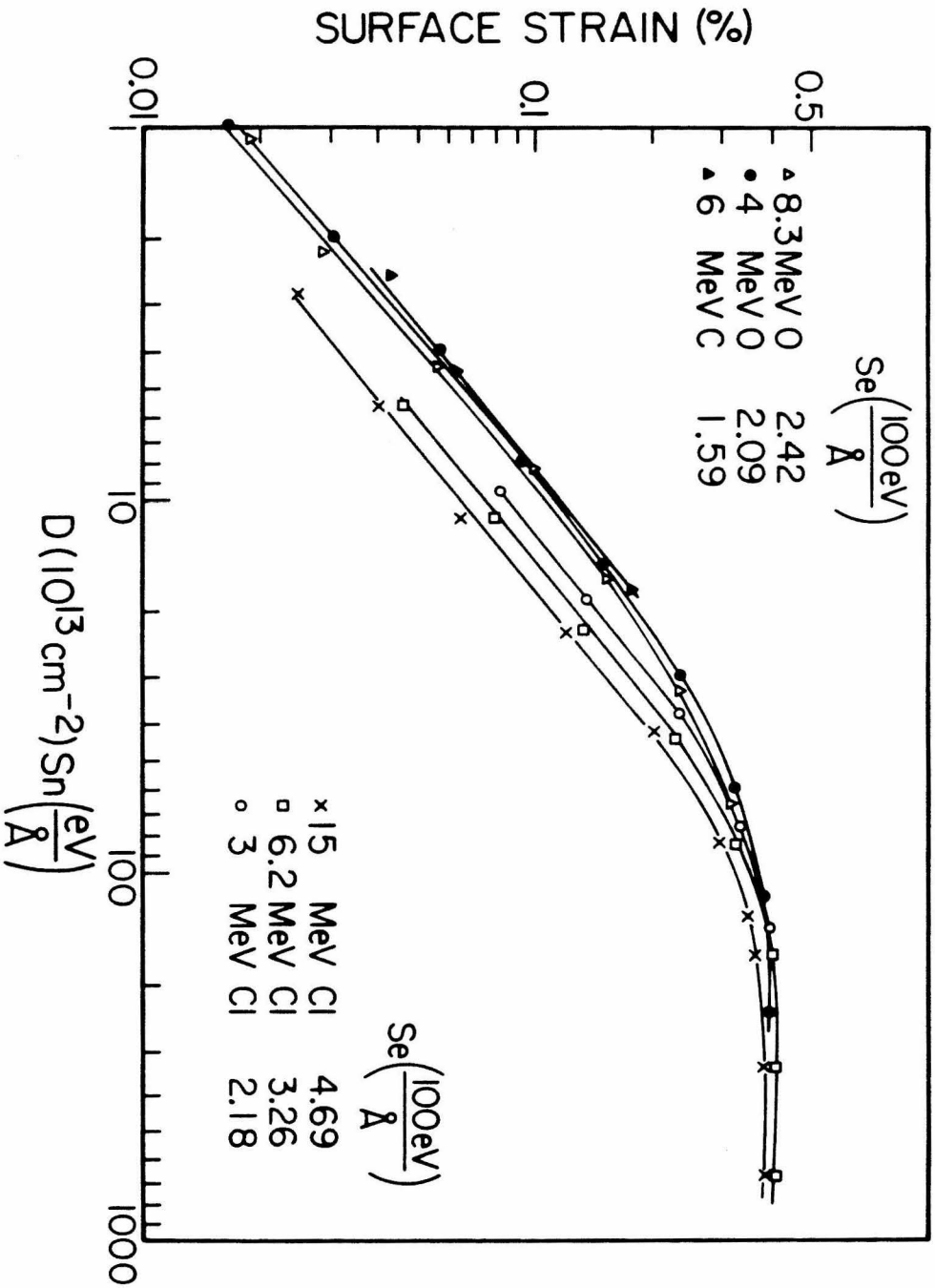


**Figure 30.** Surface strain of ion-bombarded GaAs(100) crystal. Abscissa is now beam dose times nuclear stopping power. The higher the electronic stopping power, the lower the strain is.

$$n(t) = n_0 e^{-\frac{t}{\tau}}, \quad (4.2.3)$$

where  $\tau$  is the electron-hole pair lifetime. Thus, the ionization-induced defect recovery rate can be written as

$$\frac{dN}{dt} = -k_3 N(t)n(t). \quad (4.2.4)$$

Thus, from the above equations the final number of defects per unit length,  $N_f$  created by one ion is

$$N_f = N_0 e^{-k_3 n_0 \tau}. \quad (4.2.5)$$

If  $k_3 n_0 \tau$  is smaller than unity, equation (4.2.3) becomes approximately

$$N_f \approx N_0 (1 - k_3 n_0 \tau). \quad (4.2.6)$$

At a dose range for which the cylindrical ion track regions do not overlap sufficiently, the defect concentration will be proportional to the beam dose  $D$ . Therefore, the final defect density after the ionization-induced recovery,  $n_d$ , is given by

$$n_d = DN_f \propto DS_n (1 - k S_e), \quad (4.2.7)$$

where  $k = k_2 k_3 \frac{\tau}{E_g}$ .

This model accounts for the defect recovery due to the ionization process at a given temperature. There will also be thermal recovery due to the ambient temperature during the bombardment. However, the thermal recovery does not affect the functional dependence of the final defect density on the stopping powers. In Figure 31, the surface strain is plotted against the expression in equation (4.2.7) with  $k = 0.09$ ,  $S_n$  in

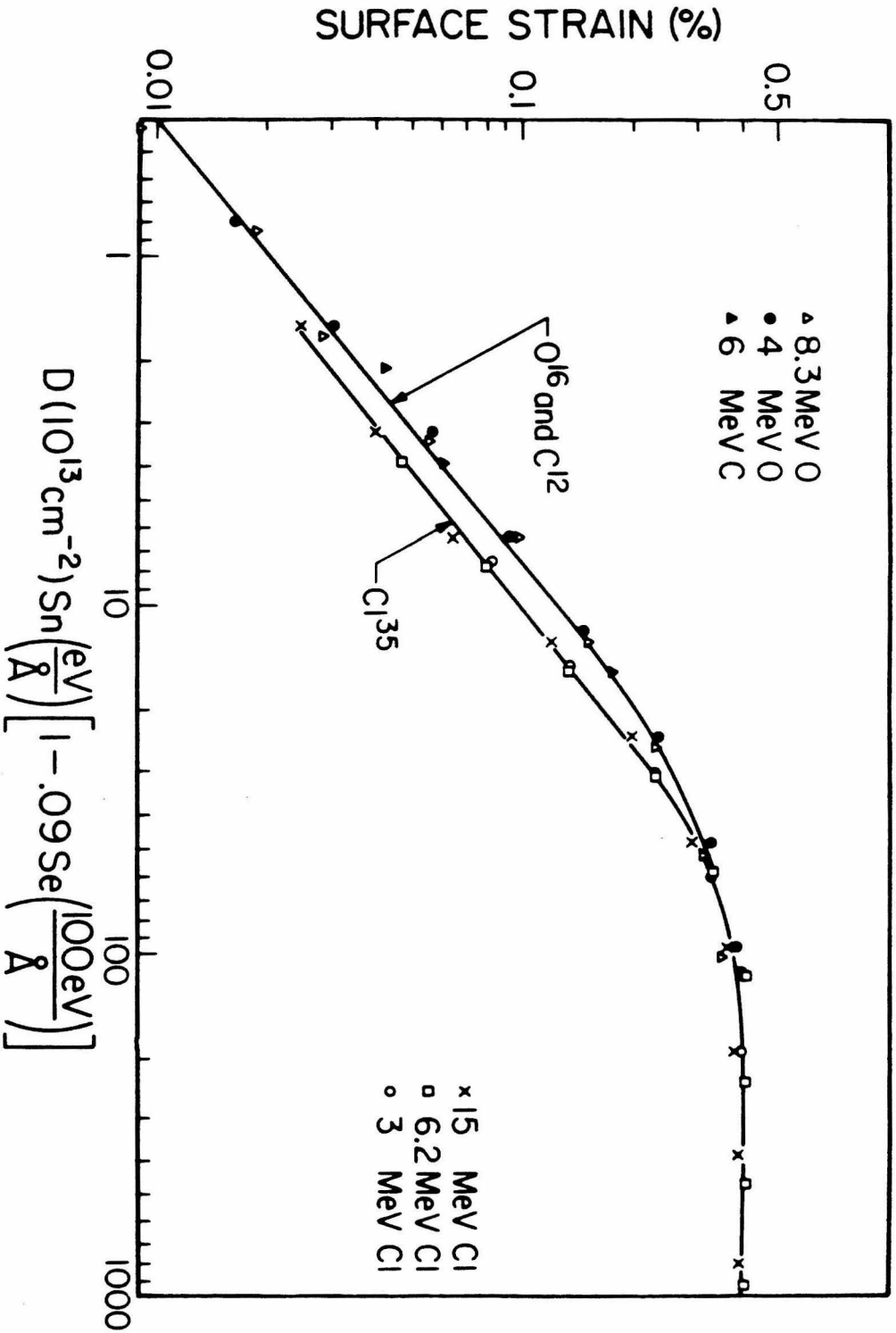


**Figure 31.** Surface strain of ion-bombarded GaAs(100) crystal. The expression on the abscissa is the relationship of final defect density with the stopping power.

eV/Angstrom, and Se in 100 eV/Angstrom. The data points show a universal curve for a given ion with a slight mismatch for different ions. The different efficiency of different ions in strain production is not well understood.

The dynamical x-ray diffraction theory presented in the previous section was used to analyze the rocking curves. Since the maximum reflecting power of the surface strained layer is much higher than 6 %, the kinematical theory analysis is not applicable. The strain and damage depth distribution for each beam dose is shown in Figure 32, with corresponding experimental and calculated rocking curves. The depth profiles illustrate very well the strain production and saturation phenomenon. The profiles also show that the region corresponding to maximum nuclear stopping power becomes amorphous at a high beam dose (see the last profile in Figure 32). The depth profile of the several micron thick layer is usually very hard to obtain with conventional experimental techniques such as Rutherford Backscattering or Auger Electron Spectroscopy. Cross-sectional TEM may provide a depth profile of comparable thickness. The strain/damage depth profile obtained from the rocking curve analysis has been shown to be consistent with that obtained from the RBS channeling technique for an ion-implanted crystal (Pa81).

A Cr-doped GaAs crystal bombarded with 15 MeV Cl ions to  $1.2 \times 10^{15} \text{ cm}^{-2}$  has been annealed at a successively higher temperature for 15 minutes. The annealing was performed in vacuum and the sample was capped with another GaAs wafer to suppress the arsenic out-diffusion. The strain corresponding to the single diffraction peak was obtained after each annealing step. The data are shown in Figures 33a and 33b. The



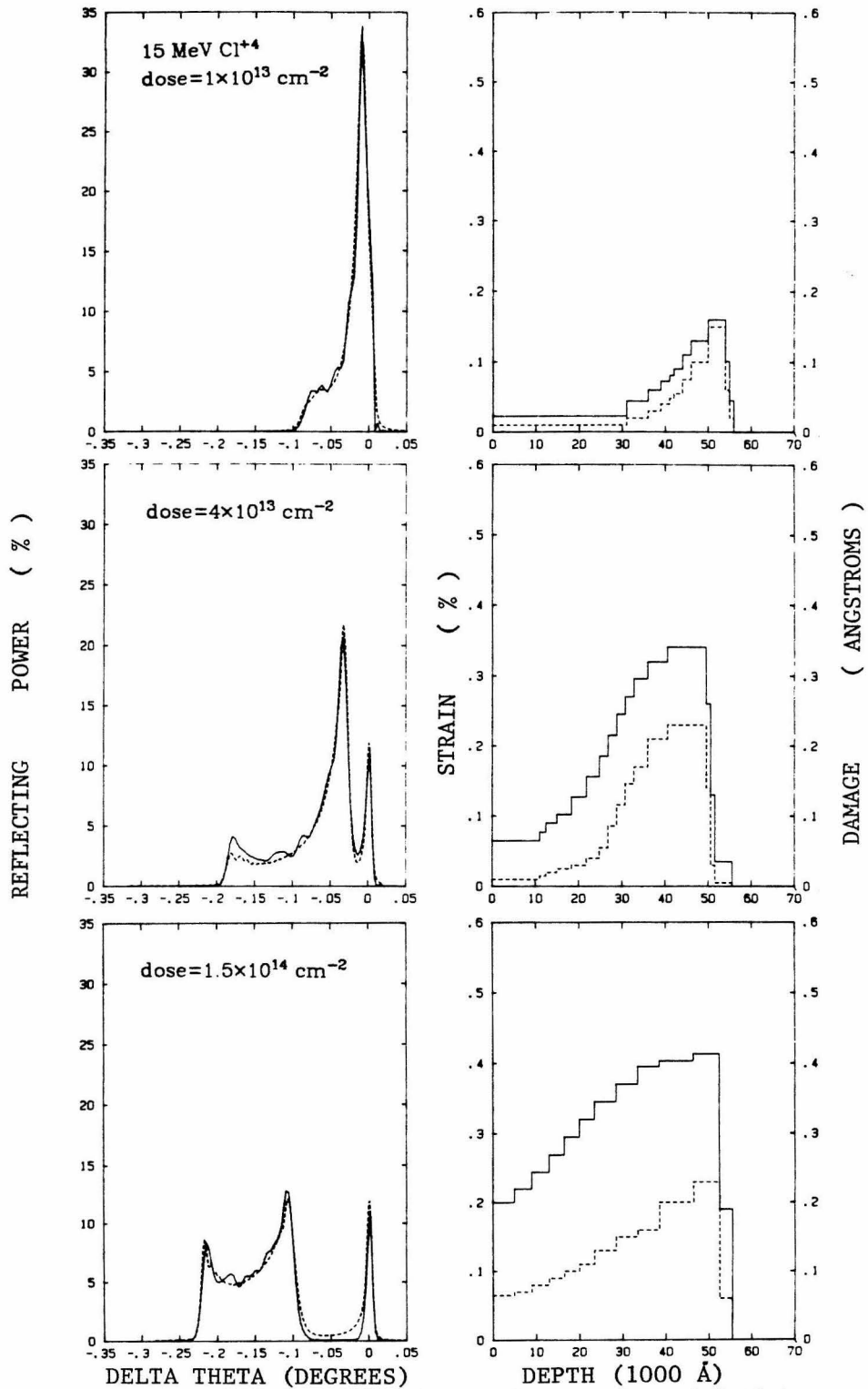


**Figure 32.** Dynamical x-ray diffraction theory analyses of the GaAs rocking curves shown in Figure 27. Left : experimental (dashed) and calculated (solid) rocking curves. Right : strain (solid) and damage (dashed) depth profile. Cont'd on next page.

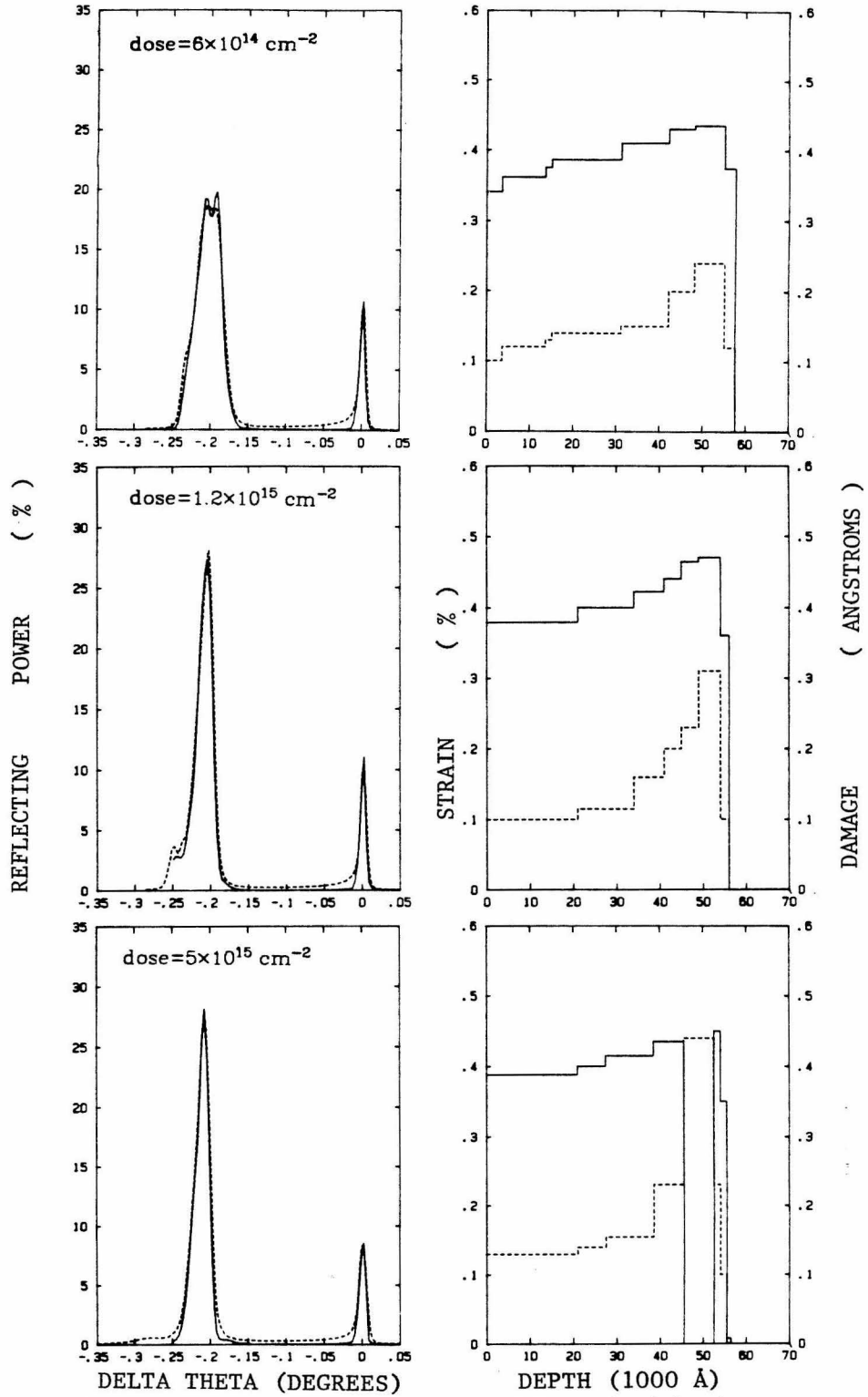
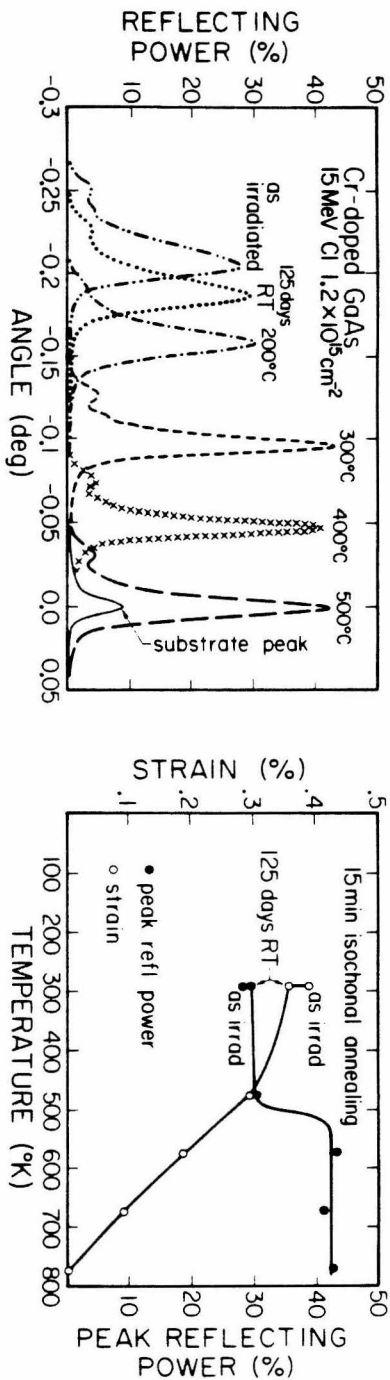


Figure 32, cont'd. Note that the layer at  $5 \mu\text{m}$  depth has become amorphous at  $5 \times 10^{15} \text{ cm}^{-2}$ .

peak reflecting power jumps at around 500 K, and appears to agree with the vacancy recovery stage in GaAs (La77, also see Figure 26). But we must be careful in associating the reflecting power jump with any physical process because, when the (100) plane of a GaAs crystal is at an angle of a few degrees from the sample surface (as is the case for most of our samples), the azimuthal orientation of the sample with respect to the incoming x-ray beam can alter the peak reflecting power significantly. The strain decreases with temperature rather smoothly, and goes to zero at around 770 K which occurs around the recovery stage of the antisite defects in GaAs (Wö82).

The strain and damage recovery behavior is shown in Figure 33c, which was obtained by the dynamical theory analyses of the rocking curves in Figure 33a. Relaxation of the overall strain/damage with annealing temperature is shown explicitly in the depth profiles. The heavily damaged layer at 5  $\mu\text{m}$  depth does not completely recover after the annealing at 500 C. We should remember that the damage in the near surface layer is mainly composed of point defects, while the damage at around 5  $\mu\text{m}$  depth is in a form of many disordered regions due to the high nuclear stopping power in this region. Strains produced by these two different forms of defects will be very much different. The thermal recovery behavior and the apparent decoupling of the strain relaxation from the damage relaxation suggests that it is a problem worth intensive future study.

Since this initial annealing experiment was performed at a large temperature step (about a 100 K interval), we tried a more careful annealing experiment to see if any distinct recovery stage was associated with it. Figure 34 shows the strain recovery data obtained from the second



**Figure 33. (a):** (400) Bragg reflection for 15 MeV Cl ion-bombarded GaAs(100) after a successive 15 min. isochronal annealing at the temperatures indicated. **(b):** Perpendicular strain and peak reflecting power versus annealing temperature. It was obtained from (a).

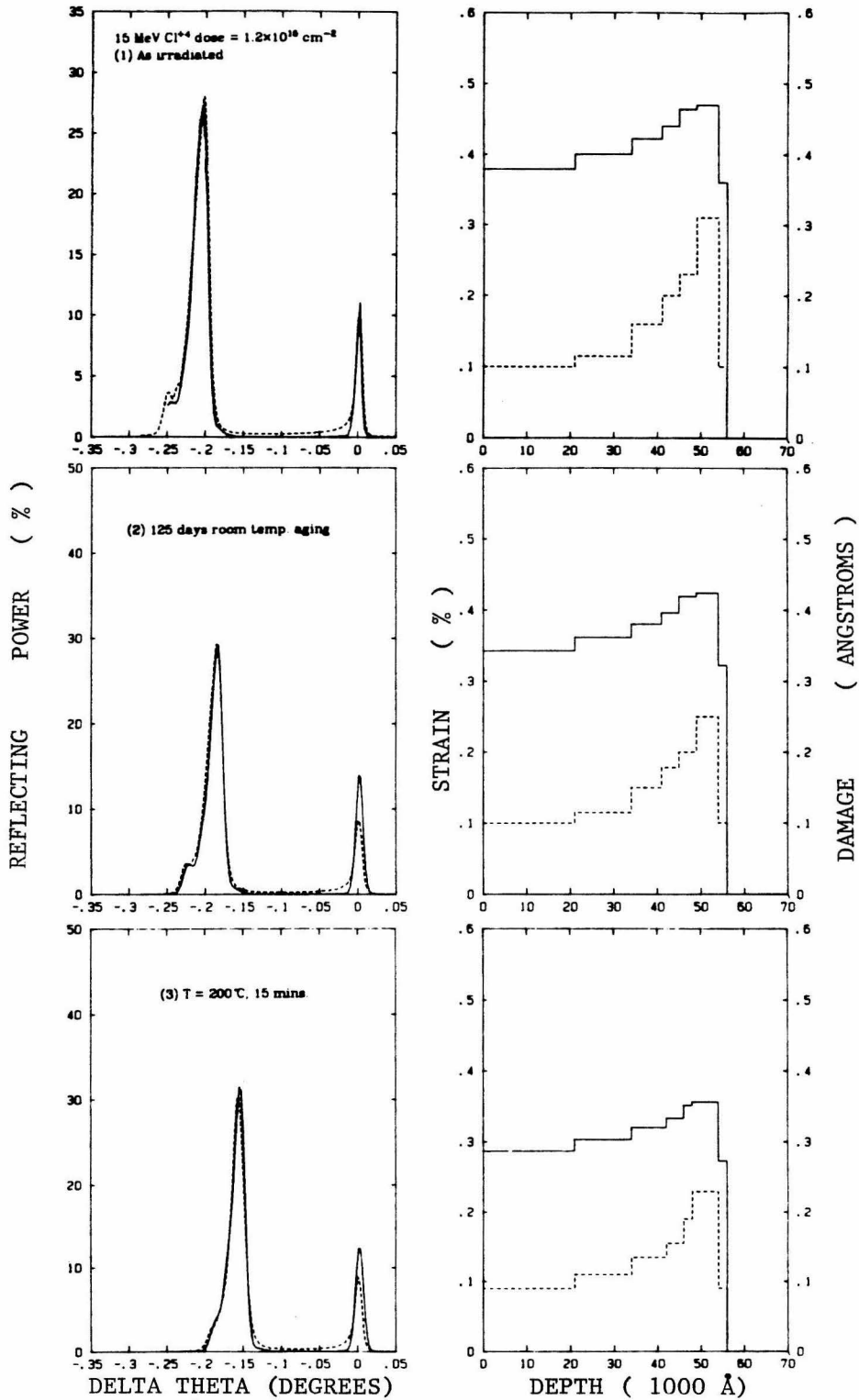


**Figure 33(c).** Thermal recovery of strain and lattice damage. The apparent decoupling of the strain relaxation from the damage relaxation implies many activation energies are involved in the strain recovery process. Cont'd on next page

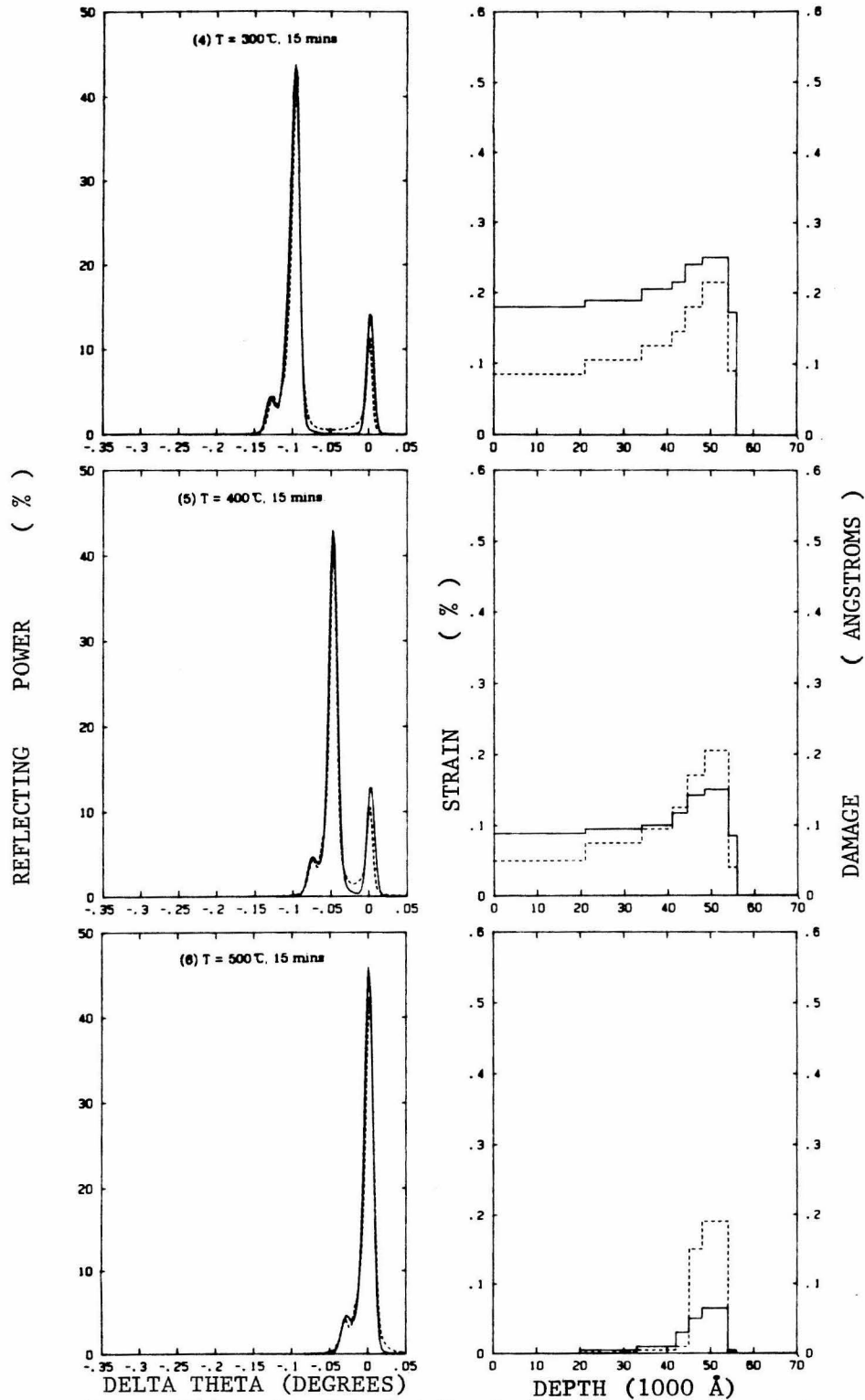


**Figure 33(c) cont'd.** Note that the strain in the heavily damaged layer at 5  $\mu m$  depth relaxes by about the same amount with the strain in the near surface layer even if total recovery of strain/damage in that layer requires much higher temperature than 500°C (actually, it recovers at 700°C).

isochronal (15 minutes) annealing experiment. The two recovery curves represent the data obtained from two samples bombarded to the same dose. Even though the two curves do not coincide exactly, both show the same trend of gradual recovery as the first isochronal anneal data.

In Figure 35, we give the isothermal anneal data obtained at several different temperatures for an 8 min. time step. The isothermal data suggest that annealing has occurred for all the strain associated with activation energies below that reached at the end of each step of annealing at a given temperature. The characteristic activation energy  $E_a$  at the end of each step annealing is defined by  $k_B T \ln(\nu t)$ , where  $\nu$  is the frequency factor approximately given by  $k_B T/h$ ,  $t$  the annealing time,  $k_B$  the Boltzmann constant,  $T$  the temperature, and  $h$  the Planck constant. The strain change which has occurred in each step of annealing,  $\Delta\epsilon$ , is approximately the integral of the activation energy spectrum from  $E_{a1}$ , the value of  $E_a$  at the end of previous step of annealing, to  $E_{a2}$ , the value of  $E_a$  at the end of present annealing. Then  $\frac{\Delta\epsilon}{(E_{a2} - E_{a1})}$  is the average value of the activation energy spectrum between  $E_{a1}$  and  $E_{a2}$ , and plotting it against  $E_a$  gives an approximate block graph of the activation energy spectrum. The isochronal anneal data in Figure 34 were analyzed in this way, and the result is given in Figure 36. The same approach has been used by Primak et al. to analyze the anneal data of radiation-induced lattice dilatation of diamond and silicon carbide (Pr56).

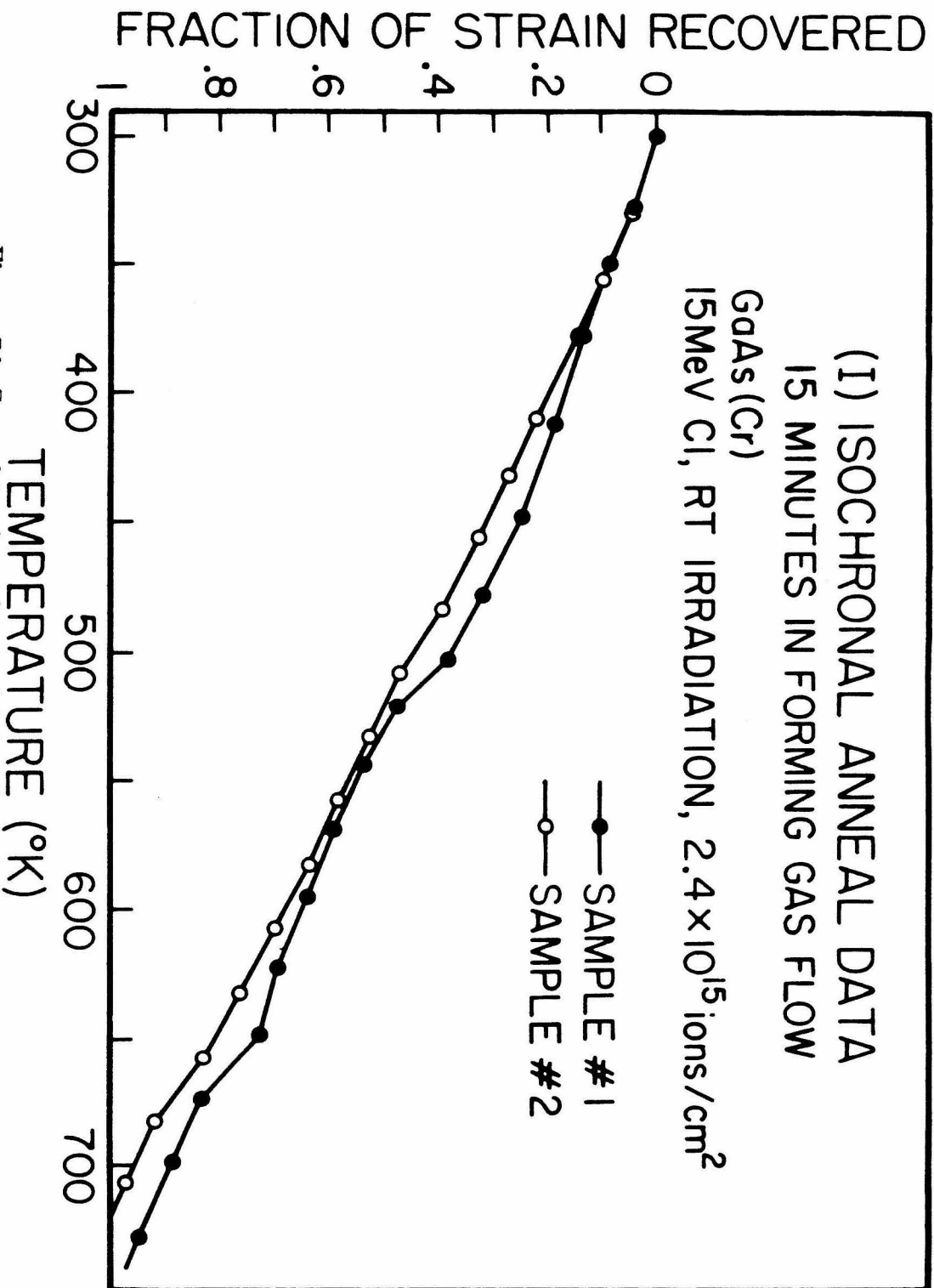


**Figure 34.** Second isochronal anneal data. The two data curves were obtained from two GaAs(100) crystals bombarded to the same dose with 15 MeV Cl ions.



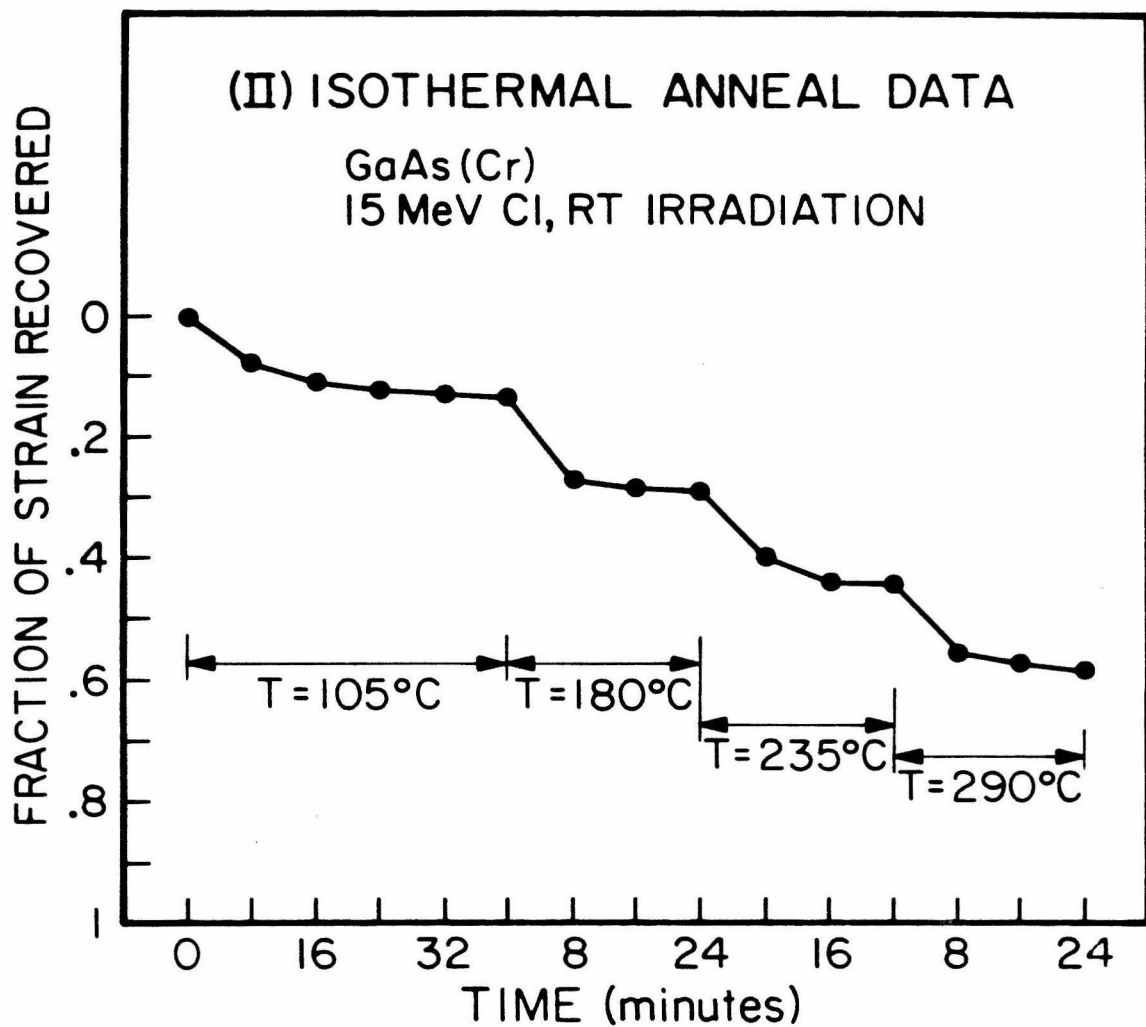


**Figure 35.** Isothermal anneal data obtained from GaAs(100) sample bombarded with the same ion to the same dose as the samples in Figure 34.

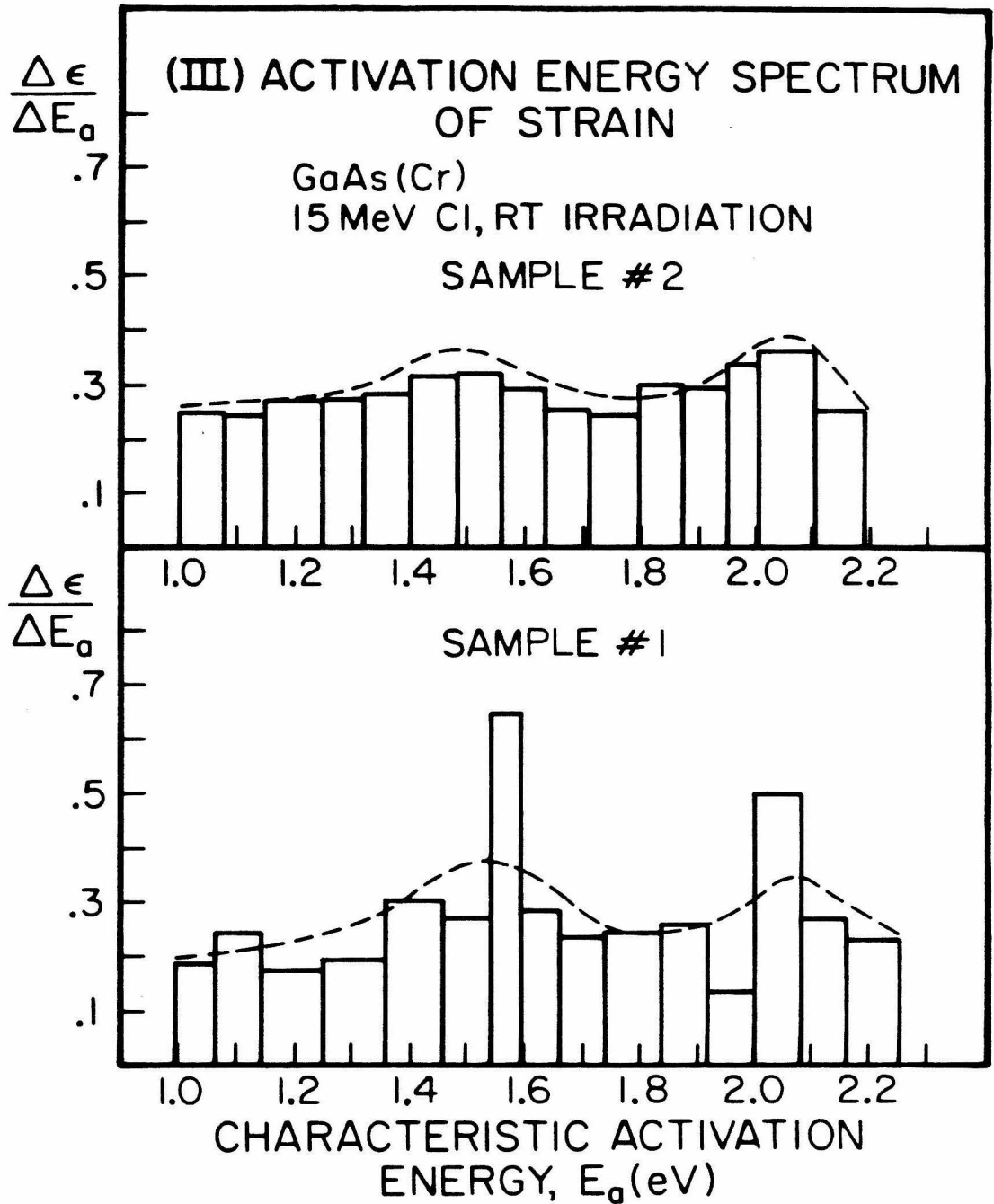


Figure 36. Activation energy spectrum obtained from the strain recovery data in Figure 34. The dashed curve is a common smooth curve for both data.

### 4.2.2 GaP

Primary defects in GaP are all stable well above room temperature according to the recovery stages shown in Figure 26. We bombarded Zn-doped GaP(100) crystals at room temperature, and measured the rocking curves for several bombardment doses to see if the strain saturation is a common phenomenon in III-V semiconductors. Figure 37 shows that the rocking curves of GaP at low beam dose follows a similar trend to GaAs, and that the strain peak at a high beam dose is symmetric but much broader than that of a corresponding GaAs crystal.

We postulate that low-temperature recovery stage defects such as close Frenkel pairs may give a much higher crystal distortion than simple defects. An interstitial defect is also a possible candidate for a higher crystal distortion than those substitutional defects such as vacancies and antisite defects. It is also believed that, among the simple defects, the interstitial defects anneal at lower temperature than the substitutional defects. To check this postulate we bombarded the Zn-doped GaP(100) crystal at an elevated temperature, i.e., at about 490 K to a high dose of  $\sim 1 \times 10^{15} \text{cm}^{-2}$ . The rocking curve taken from this sample is given in Figure 38, and shows a sharp strain peak with very narrow linewidth. This result demonstrates that strain or defects saturation is common for GaAs and GaP crystals, and that low-temperature recovery stage defects give rise to high distortion to the crystal field around each defect. This may indicate that the saturation phenomenon is general for all the III-V semiconductors.

The room-temperature bombarded GaP crystal was annealed isochronally. Figure 39 shows the strain recovery, the x-ray broadening, and the peak reflecting power of the strain peak as a function of annealing

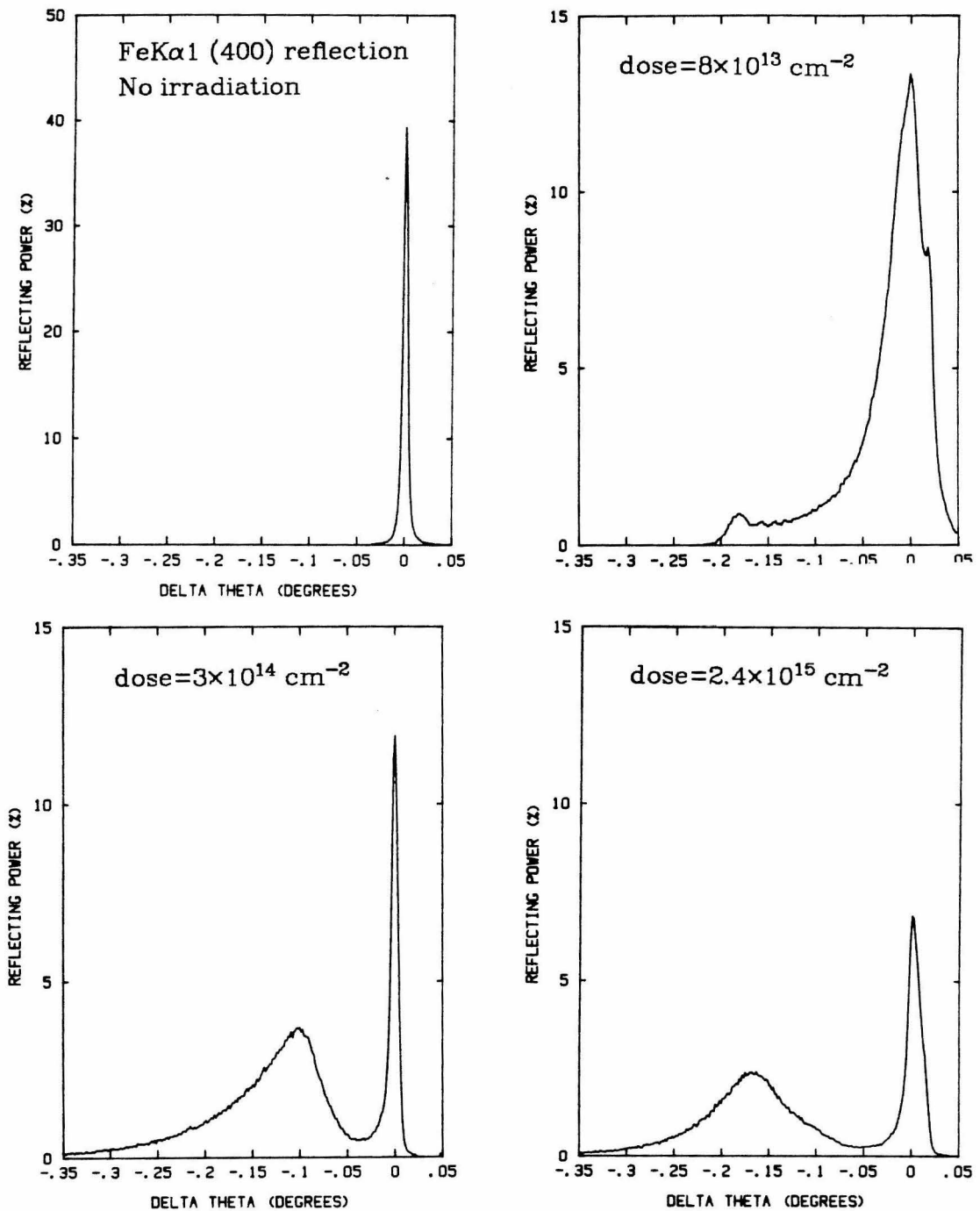


**Figure 37.** Rocking curves for Zn-doped GaP(100) crystals irradiated with with 15 MeV Cl ions at room temperature. The strain peak after a high-dose bombardment is much boader than for a corresponding GaAs crystal.

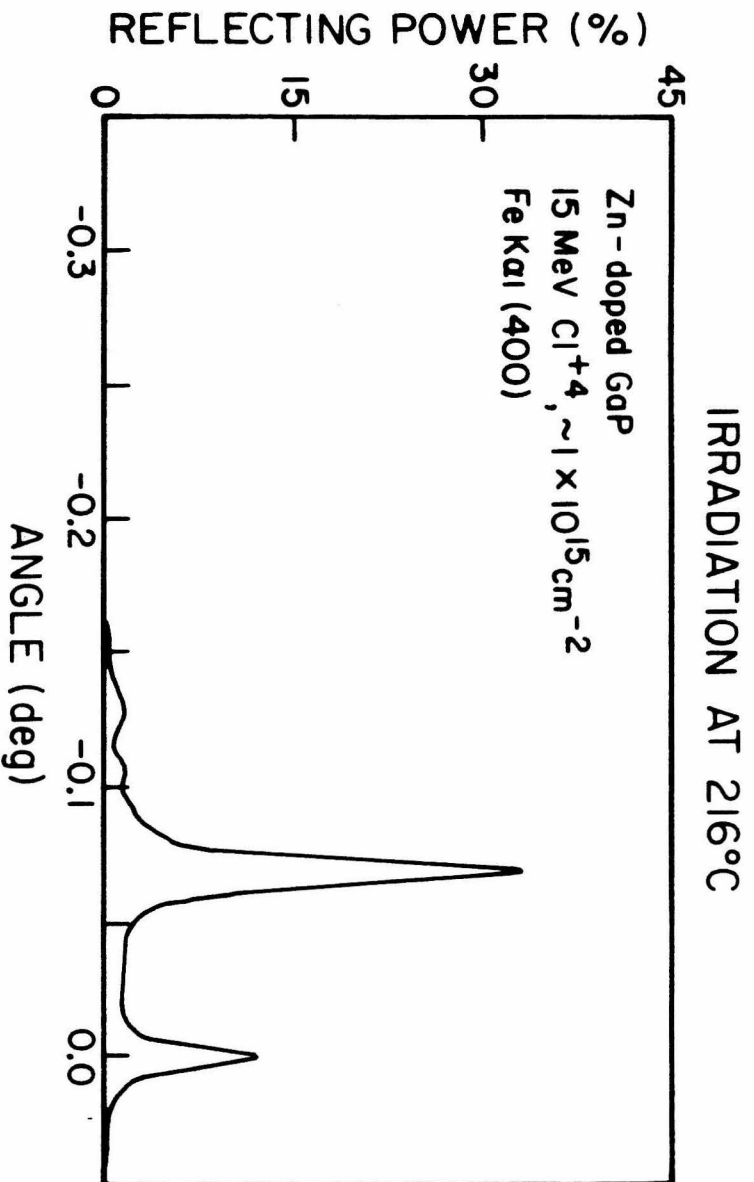


**Figure 38.** FeK $\alpha_1$  (400) reflection from GaP(100) crystal bombarded at 216°C. The 15 MeV Cl beam dose is roughly  $1 \times 10^{15}$  cm<sup>-2</sup>.

temperature. It also shows that there is a significant relaxation of strain in room temperature (i.e., after 73 days room-temperature aging). This room-temperature relaxation is probably due to the slow recovery of low-temperature recovery stage defects. Picraux has shown that the lattice disorder, in a GaP(111) crystal implanted at 120 K, recovers over a temperature range from 150 K to 400 K for a low-fluence implantation ( $1.5 \times 10^{13}$  Zn or Sb/cm<sup>2</sup>), and the disorder recovers over a range from 300 K to 620 K for a high fluence implantation ( $1.1 \times 10^{14}$  Zn or Sb/cm<sup>2</sup>) (Pi73). The recovery stages for III-V compounds shown in Figure 26 should be considered with care.

One should note that the strain and the x-ray linewidths are smaller for the GaP crystal irradiated at a high temperature than for the same crystal irradiated at room temperature and subsequently annealed to the same high temperature. The strain and the linewidths are .08 % and 40 arcseconds for the sample bombarded at 490 K, and .11 % and 82 arcseconds for the sample bombarded at room temperature and subsequently annealed up to 490 K.

We close this section by saying that the results on GaAs and GaP suggest a general trend in MeV ion-induced strain production and saturation, and crystal field distortion in the III-V semiconductors which is closely related to the defect recovery stages in each material.

### ANNEALING OF GaP(100) BOMBARDED BY 15 MeV Cl IONS TO $2.4 \times 10^{15}$ Cl/cm<sup>2</sup>

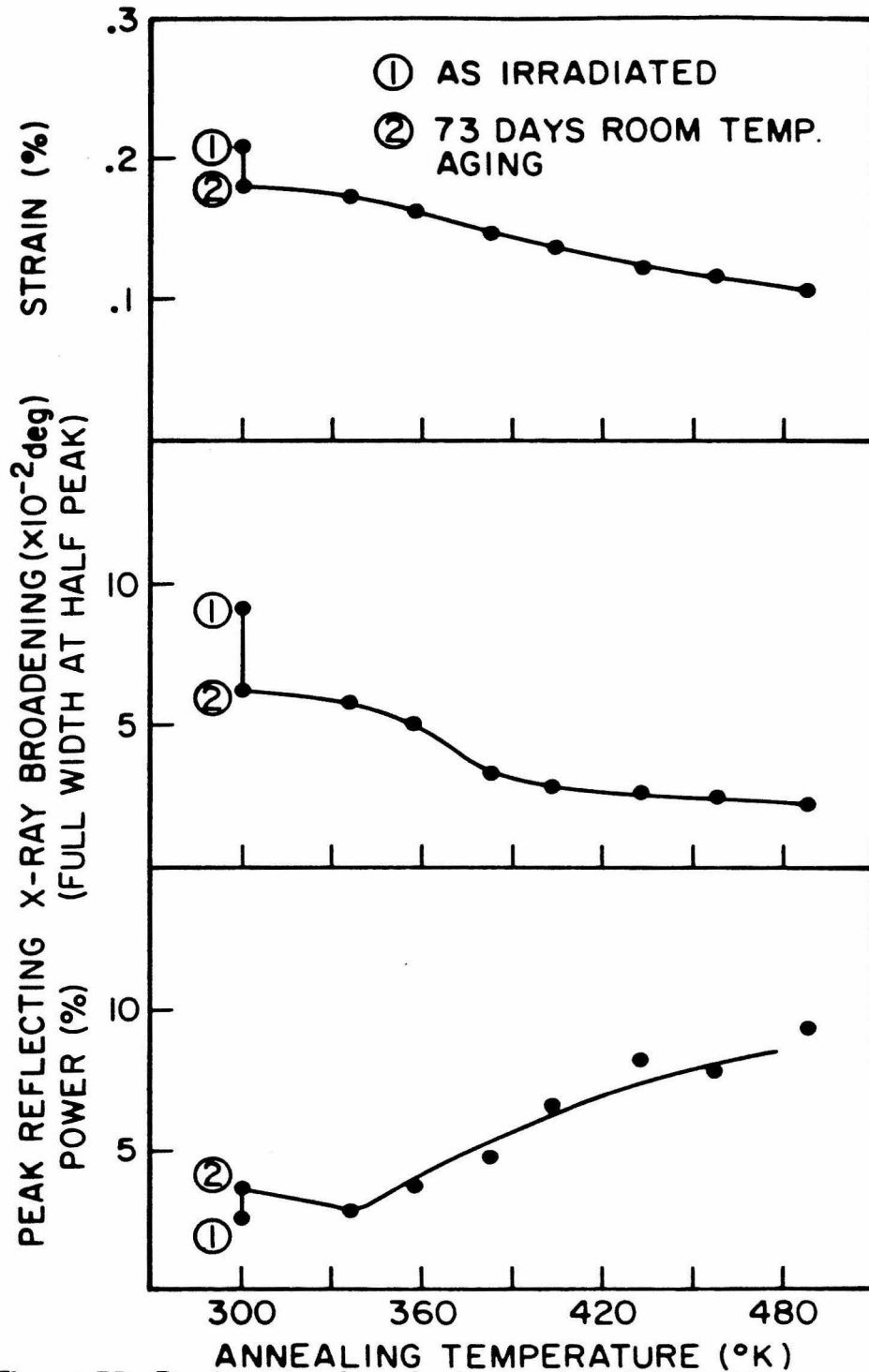


Figure 39. Strain, x-ray broadening, and peak reflecting power for a successive isochronal annealing of the ion bombarded GaP.

### 4.2.3 Summary

Bombardment of III-V semiconductors with MeV ions produces strains which corresponds to the lattice dilatation normal to the surface, with negligible parallel expansion. The strain in the surface layers is mainly due to point defects produced by the nuclear collision process. Partial relaxation of the strain is caused by the electronic process.

The strain saturation in GaAs bombarded at room temperature, and in GaP bombarded at an elevated temperature, suggests that there is a saturated defect density at a given bombardment temperature for the III-V semiconductor materials. It is not clear whether the balancing of production and recovery of defects at the saturate point is a dynamic process (i.e., radiation-induced dynamic recovery) or a thermal process (i.e., quasi thermal equilibrium).

The x-ray rocking curves from the GaP crystals bombarded at room temperature, and from the same crystal bombarded at an elevated temperature, indicate that low-temperature recovery stage defects generally cause major distortion to the crystal fields. This may explain the rather sharp strain peaks from the room-temperature irradiated GaAs crystals for a high-dose bombardment, because the recovery stages are generally at lower temperatures in GaAs than in GaP.

The x-ray rocking curve technique with the dynamical diffraction theory analysis was shown to provide the depth profiles of radiation damage for a relatively thick layer ( typically  $10 \mu m$ ). Also it illustrates very well the progression of strain and damage as the ion fluence increases. This non-destructive technique is advantageous because of rapid data acquisition and low equipment cost compared to RBS and AES spectroscopy.



The gradual recovery of the lattice strain with the annealing temperature was interpreted in terms of a spectrum of activation energies. The absence of major recovery stages in the strain anneal data is in contrast with those results obtained from using other probes of radiation damage such as electrical and/or optical measurements.

## Appendix A : Derivation of The Takagi-Taupin Equation

Let us consider the physical basis of the theory. Basic assumptions made in the theory will be discussed. Our aim is to derive a differential equation which will describe the spatial variation of the incident and diffracted waves due to absorption and diffraction by the medium.

The deformation is assumed to be small. The variation of the deformation over one x-ray wavelength is assumed to be smaller than the deformation itself. If  $w$  is the displacement of a lattice atom, then

$$\left| \frac{\partial w}{\partial x_j} \right| \ll 1 ,$$

$$\left| \frac{\partial^2 w}{\partial x_i \partial x_j} \lambda \right| \ll \left| \frac{\partial w}{\partial x_i} \right| ,$$

and these are the only assumptions on the deformation of the crystal medium, which makes the resulting theory quite general in describing diffraction from the deformed crystals. Also, the deformation can vary in any direction of the medium. In Section 4.2.2 we considered the case of longitudinal variation only, for the convenience of dealing with the x-ray rocking curve technique.

If the incident and diffracted waves can be approximated by plane waves, then the total wave field inside the medium is:

$$\vec{D}(\vec{r}) = \sum_H \vec{D}_H(\vec{r}) e^{i\omega_0 t - i2\pi \vec{\beta}_H \cdot \vec{r}} , \quad (\text{A.1})$$

where the capital subscript  $H$  refers to crystal planes with Miller indices  $(h,k,l)$ , and  $H = 0$  corresponds to the incident wave.

The variation of the amplitudes over one x-ray wavelength is assumed to be small; i.e.,

$$\left| \frac{\partial \vec{D}_{0,H}}{\partial x_i} \lambda \right| \ll \left| \vec{D}_{0,H} \right| ;$$

it is further assumed that

$$\left| \frac{\partial^2 \vec{D}_{0,H}}{\partial x_i \partial x_j} \lambda \right| \ll \left| \frac{\partial \vec{D}_{0,H}}{\partial x_i} \right| .$$

We shall assume the magnetic permeability to be unity and the current density to be zero. The dielectric constant for the x-ray frequency range is very close to unity. Thus,

$$\epsilon = 1 + \Psi , \quad (\text{A.2})$$

where  $\Psi \ll 1$ . Since the x-ray wavelengths are on the order of the crystal lattice spacing, x-ray photons will see the crystal structure. So we expand  $\Psi$  in a Fourier series in the reciprocal lattice space.

$$\Psi(\vec{r}) = \sum_H \Psi_H e^{-2\pi \vec{\beta}_H \cdot \vec{r}} , \quad (\text{A.3})$$

where  $\vec{\beta}_H$  is the reciprocal lattice vector, and  $\vec{\beta}_H = \vec{\beta}_0 + \vec{B}_H$  (Bragg's law).

From the Maxwell equations, the wave equation follows,

$$\vec{\nabla} \times \vec{\nabla} \times [\vec{D}(\vec{r}) (1 - \Psi(\vec{r}))] = -\frac{1}{c^2} \frac{\partial^2 \vec{D}}{\partial t^2} . \quad (\text{A.4})$$

Inserting equations (A.1) and (A.3) into (A.4) and comparing the coefficients of the exponential factor, we get

$$\vec{\nabla} \times \vec{\nabla} \times [(\vec{D}_L(\vec{r}) - \sum_K \vec{D}_K(\vec{r}) \Psi_{H-K}) e^{-i2\pi \vec{\beta}_L \cdot \vec{r}}] = 4\pi^2 k_0^2 \vec{D}_L(\vec{r}) e^{-i2\pi \vec{\beta}_L \cdot \vec{r}} , \quad (\text{A.5})$$

where  $k_0$  is the wave vector value in vacuum.

If there exist two internal waves in the medium, i.e., the incident wave and one diffracted wave, then we may set

$$\vec{D}_0 \neq 0, \vec{D}_H \neq 0, \text{ and } \vec{D}_L = 0 \text{ for } L \neq 0, H. \quad (\text{A.6})$$

Equations (A.5) and (A.6) yield

$$\vec{\nabla} \times \vec{\nabla} \times [(\vec{D}_0(\vec{r}) - \Psi_0(\vec{r})\vec{D}_0(\vec{r}) - \Psi_H(\vec{r})\vec{D}_H(\vec{r}))e^{-i2\pi\vec{\beta}_0 \cdot \vec{r}}] = 4\pi^2 k_0^2 \vec{D}_0(\vec{r})e^{-i2\pi\vec{\beta}_0 \cdot \vec{r}}, \quad (\text{A.7})$$

$$\vec{\nabla} \times \vec{\nabla} \times [(\vec{D}_H(\vec{r}) - \Psi_0(\vec{r})\vec{D}_H(\vec{r}) - \Psi_H(\vec{r})\vec{D}_0(\vec{r}))e^{-i2\pi\vec{\beta}_H \cdot \vec{r}}] = 4\pi^2 k_0^2 \vec{D}_H(\vec{r})e^{-i2\pi\vec{\beta}_H \cdot \vec{r}}.$$

A further reduction of equation (A.7) is made with the following considerations.

- i) Neglect  $\frac{\partial^2 \vec{D}_0}{\partial x_i \partial x_j}$ ,  $\frac{\partial^2 \vec{D}_H}{\partial x_i \partial x_j}$ , and  $\frac{\partial}{\partial x_i}(\Psi_L \vec{D}_K)$  : first-order approximation.
- ii)  $\vec{\beta}_0 \cdot \vec{D}_0 = 0$ ,  $\vec{\beta}_H \cdot \vec{D}_H = 0$  : transverse wave.
- iii)  $\vec{\nabla} \cdot \vec{D}_{0,H}(\vec{r}) = 0$  : variation only along the propagation direction.
- iv)  $\vec{\beta}_0 \cdot \vec{D}_H = 0$ ,  $\vec{\beta}_H \cdot \vec{D}_0 = 0$  : for the normal polarization.
- v) Corresponding results for the parallel polarization are obtained by replacing  $\Psi_H$  by  $\Psi_H \cos 2\theta_B$  everywhere.

With i) - v) taken into account, equation (A.7) results in the Takagi-Taupin equation:

$$i \frac{\lambda}{\pi} \vec{\beta}_0 \cdot \vec{\nabla} \vec{D}_0(\vec{r}) = \Psi_0 \vec{D}_0(\vec{r}) + \Psi_H \vec{D}_H(\vec{r}),$$

$$i \frac{\lambda}{\pi} \vec{\beta}_H \cdot \vec{\nabla} \vec{D}_H(\vec{r}) = \Psi_0 \vec{D}_H(\vec{r}) + \Psi_H \vec{D}_0(\vec{r}) - \alpha_H \vec{D}_H(\vec{r}) ,$$

where  $\alpha_H = \frac{1}{k_0^2} (B_H^2 + 2\vec{k}_0 \cdot \vec{B}_H)$ , which is approximately  $2(\Theta_B - \Theta) \sin 2\Theta_B$  for the Bragg case.

**Appendix B : Formula for Evaluating  $s = \sqrt{C^2 - B^2}$**

$$s = s_1 + is_2 \text{ for } y \leq -q_1,$$

$$s = s_2 + is_1 \text{ for } -q_1 < y \leq q_2,$$

$$s = -s_2 + is_1 \text{ for } q_2 < y \leq q_1,$$

$$s = -s_1 + is_2 \text{ for } y > q_1,$$

where

$$s_1 = \sqrt{\frac{r+r_1}{2}},$$

$$s_2 = \sqrt{\frac{r-r_1}{2}},$$

$$q_1 = \sqrt{1-k^2+g^2},$$

$$q_2 = \frac{k}{g},$$

and

$$r_1 = \left| y^2 - g^2 + k^2 - 1 \right|,$$

$$r_2 = 2(yg - k),$$

$$r = \sqrt{r_1^2 + r_2^2}.$$

## References

- Al84 M. Alonso, J. L. Sacedo'n, and F. Soria, *Appl. Phys. Lett.*, **45**, 154 (1984).
- As84 C. I. H. Ashby, *Appl. Phys. Lett.*, **45**, 892 (1984).
- Ba84 J. E. E. Baglin, G. J. Clark, and J. Bottiger, in *Thin Films and Interfaces*, edited by J. E. E. Baglin et al. (Elsevier, North Holland, 1984) p.179.
- Br84 P. Brewer, H. Scott, and R. M. Osgood, Jr., *Appl. Phys. Lett.*, **45**, 475 (1984).
- Co66 J. W. Corbett, in *Solid State Physics*, edited by F. Seitz and D. Turnbull, Suppl. 7 (Academic Press Inc., New York and London 1966), p.39.
- Da81 E. Dartyge, T. P. Duraud, Y. Langevin, and M. Maurette, *Phys. Rev.*, **234**, 5231 (1981).
- Ei57 F. H. Eisen and C. E. Birchenall, *Acta Met.*, **5**, 265 (1957).
- Ei71 F. H. Eisen, in *Radiation Effects in Semiconductors*, edited by J. W. Corbett and G. D. Watkins (Gordon and Breach, New York 1971), p.273.
- Es56 J. D. Eshelby, in *Solid State Physics*, edited by F. Seitz and D. Turnbull (Academic Press Inc., New York 1956), vol.3, p.79.
- Fl75 R. L. Fleischer, P. B. Price, and R. M. Walker, **Nuclear Tracks in Solids** (University of California Press, Berkeley 1975).
- Go61 B. Goldstein, *Phys. Rev.*, **121**, 1305 (1961).

- Gr79a R. W. Grant and R. M. Housley, in *Electron and Positron Spectroscopies in Materials Science and Engineering*, edited by O. Buck et al. (Academic Press, 1979), p.219.
- Gr79b J. E. Griffith, Ph. D. Thesis, California Institute of Technology, (1979).
- Gr82 J. E. Griffith, Y. Qui, and T. A. Tombrello, Nucl. Instr. Meth. **198**, 607 (1982).
- Ha84 M. A. G. Halliwell, M. H. Lyons, and M. J. Hill, Journal of Crystal Growth, **68**, 523 (1984).
- Ja83 S. Jacobson, B. Jönssen, and B. Sundqvist, University of Uppsala Preprint (1983).
- Ki76 C. Kittel, **Introduction to Solid State Physics**, Fifth ed. (Wiley, New York 1976).
- Kl73 B. Klar, and F. Rustichelli, Nuovo Cimento, **13B**, 249 (1973).
- La77 D. V. Lang, R. A. Logan, and L. C. Kimmerling, Phys. Rev. B, **15**, 4874 (1977).
- La80a B. C. Larson, and J. F. Barhorst, J. Appl. Phys. **51**, 3181 (1980).
- Li61 J. Lindhard, and M. Scharff, Phys. Rev. **124**, 128 (1961).
- Li80b U. Littmark, and J. F. Ziegler, **Handbook of Range Distributions for Energetic Ions in All Elements, Vol.6** (Pergamon Press, New York 1980).
- Li84 R. P. Livi, S. Paine, C. R. Wie, M. H. Mendenhall, J. Y. Tang, T. Vree-land, Jr., and T. A. Tombrello, Proc. Matr. Res. Soc. of 1984 (1985), in press.



- Mc59 J. W. McKay, E. E. Klontz, and G. W. Gobeli, *Phys. Rev. Lett.*, **2**, 146 (1959).
- Me83 M. H. Mendenhall, Ph. D. Thesis, California Institute of Technology (1983).
- Mi84a I. V. Mitchell, J. S. Williams, P. Smith, and R. G. Elliman, *Appl. Phys. Lett.*, **44**, 193 (1984).
- Mi84b I. V. Mitchell, G. Nyberg, and R. G. Elliman, *Appl. Phys. Lett.*, **45**, 137 (1984).
- Mo68 D. V. Morgan, and L. T. Chadderton, *Phil. Mag.*, **17**, 1135 (1968).
- No70 L. C. Northcliffe, and R. F. Schilling, **Range and Stopping Power Table for Heavy Ions**, Nuclear Data Tables 7, NO. 3-4 (Academic Press, New York 1970).
- Pa81 B. M. Paine, V. S. Speriosu, L. S. Wielunski, H. L. Glass, and M. A. Nicolet, *Nucl. Instr. Meth.*, **191**, 80 (1981).
- Pi73 S. T. Picraux, *Rad. Eff.*, **17**, 261 (1973).
- Pi66 V. Piesbergen, in *Semiconductors and Semimetals*, edited by R. K. Willandson and A. C. Beer, Vol.2, (Academic Press, New York 1966) p.49.
- Po84 D. V. Podlesnik, H. H. Gilgen, and R. M. Osgood, Jr., *Appl. Phys. Lett.*, **45**, 563 (1984).
- Pr55 W. Primak, *Phys. Rev.*, **100**, 1677 (1955).
- Pr56 W. Primak, L. H. Fuches, and P. P. Day, *Phys. Rev.*, **103**, 1184 (1956).

- Pr75 W. Primak, **The Compacted States of Vitreous Silica** (Gordon and Breach, New York 1975).
- Qi83 Y. Qiu, J. E. Griffith, W. J. Meng, and T. A. Tombrello, *Rad. Eff.*, **70**, 231 (1983).
- Sa84 G. A. Sai-Halasz, and G. Gazecki, *Appl. Phys. Lett.*, **45**, 1067 (1984).
- Si59 R. O. Simmons, and R. W. Balluffi, *J. Appl. Phys.*, **30**, 1249 (1959).
- Si69 L. L. Sivo, and E. E. Klontz, *Phys. Rev.*, **178**, 1264 (1969).
- Si77 P. Sigmund, in *Inelastic Ion-Surface Collisions*, edited by N. H. Tolk and J. C. Tully (Academic Press, New York 1977), p.121.
- So84 D. K. Sood, W. M. Skinner, and J. S. Williams, Royal Melbourne Institute of Technology Preprint, Australia.
- Sp81 V. S. Sperosu, *J. Appl. Phys.*, **52**, 6094 (1981).
- Sp84 V. S. Speriosu, and T. Vreeland, Jr., *J. Appl. Phys.*, **56**, 1591 (1984).
- Sz81 S. M. Sze, **Physics of Semiconductor Devices**, Second ed. (John Wiley & Sons Inc., New York 1981), p.74.
- Ta62 S. Takagi, *Acta Cryst.*, **15**, 1311 (1962).
- Ta64 D. Taupin, *Bull. Soc. Franc. Mine'r. Cryst.*, **87**, 469 (1964).
- Th70 K. Thommen, *Rad. Eff.*, **2**, 201 (1970).
- To83 T. A. Tombrello, *Int. J. Mass Spectrom. Ion Phys.*, **53**, 307 (1983).
- To84a T. A. Tombrello, C. R. Wie, N. Itoh, and T. Nakayama, *Phys. Lett.*, **100A**, 42 (1984).
- To84b T. A. Tombrello, *Nucl. Instr. Meth.*, **B2**, 555 (1984).

- Va43 V. Vand, Proc. Phys. Soc., (London), **55**, 222 (1943).
- Vr85 T. Vreeland, Jr., Private Communication (1985).
- We83 B. T. Werner, T. Vreeland, Jr., M. H. Mendenhall, Y. Qiu, and T. A. Tombrello, Thin Solid Films, **104**, 163 (1983).
- Wi77 W. D. Wilson, L. G. Haggmark, and J. P. Biersack, Phys. Rev. B, **15**, 2458 (1977).
- Wi84 C. R. Wie, T. Vreeland, Jr., and T. A. Tombrello, Proc. Matr. Res. Soc. of 1984 (1985), in press.
- Wi85a C. R. Wie, C. R. Shi, M. H. Mendenhall, R. P. Livi, T. Vreeland, Jr., and T. A. Tombrello, Nucl. Instr. Meth. (1985), in press.
- Wi85b C. R. Wie, T. Vreeland, Jr., and T. A. Tombrello, Nucl. Instr. Meth. (1985), in press.
- Za45 W. H. Zachariasen, **Theory of X-Ray Diffraction in Crystals** (Wiley, New York 1945).